KNOCK DAMAGE
IN SPARK-IGNITION ENGINES

R.J.NATES PrEng, MSc(Eng), BSc(Mech Eng) Cape Town

Thesis presented for the Degree of
DOCTOR OF PHILOSOPHY
in the Department of Mechanical Engineering
UNIVERSITY OF CAPE TOWN
June 1995

ABSTRACT

The objectives of this thesis were to identify, explain and quantify the damage caused by knocking combustion in spark-ignition engines.

A literature review indicated that, in general, research into knock has focused on the causes and avoidance of knock, rather than on the damage resulting from knock. The few published works concerning the effects of knock were mainly interested in the prevention of one specific form of damage, namely piston erosion. The review highlighted the need to investigate the relationship between knock and the various forms of damage.

Using the evidence from knock-damaged engines, the sequence of events leading to failure were reconstructed. The manner in which knock damage manifests itself as surface erosion, piston-ring failure, piston-land cracking, piston blow-by and seizure were examined. From these observations it was deduced that two independent damage paths result from knock. Consequently, the research diverged into two studies, namely:

- Local pressure-temperature transients in the end-gas zone which cause localised erosion damage.
- Excessive heat flux associated with knocking combustion which results in global piston and ring problems.

The investigation into localised pressure-temperature transients included theoretical analysis, detonation chamber tests, together with experiments performed on a modified research engine. A model describing detonation waves was used to gain an understanding of the parameters controlling the intensity of these waves. A detonation chamber was used to validate the accuracy of the model, and to investigate the effect of operating conditions on erosion damage. An analysis of the thermal stresses was undertaken to determine their contribution towards erosion damage. Engine tests were used to measure the erosion damage under various operating conditions, and to test the validity of the predictions made by the theoretical analysis. A knock parameter was identified and correlated to erosion damage. This was used to develop a criterion for the assessment of the safety margin for operating under knocking conditions without causing erosion damage.

Knock damage due to excessive heat flux was investigated by means of engine and other tests. A theoretical and experimental study determined the relationship between knock and ring gap. The extent of plastic yield of piston rings under simulated conditions was investigated. The manner in which knock causes rings to jam in their ring grooves was established experimentally. The results of these studies enabled the identification of a knock intensity parameter related to the heat flux modes of failure. This parameter was used to quantify the safety margin for operating under knocking conditions without piston or ring damage.

The interrelationships between these various modes of engine failure were identified, resulting in an explanation of the pathways leading from knock to damage. Ultimately, the independent studies were used to establish methods for the determination of damage-free, knocking operation.

DECLARATION

I declare that this thesis is essentially my own work and that it has not been submitted for a degree at any other university.

.....

R.J.Nates

June 1995

ACKNOWLEDGEMENTS

I greatly appreciate the guidance and support given by my supervisor Dr Andrew Yates. I was extremely privileged to have worked with a person of such harmony and balance.

I thank my wife, Sharon and children, Gary and Theo for their support and encouragement, and express my gratitude for their gift of time for this task. This work is dedicated to them.

I would like to thank SASOL (Ltd) and in particular Dr Johan Botha for initiating and financing this work.

I acknowledge the assistance given by John Fitton towards the some of the experimental and photographic work.

Nulla est homini causa philosophandi,
nisi ut beatus sit
(St Augustine)

Man has no reason to philosophise,
except with a view to happiness

CONTENTS Page

SUMMARY i
ACKNOWLEDGEMENTS iii
DECLARATION iv
LIST OF FIGURES viii

1. INTRODUCTION AND RATIONALE 1

2. LITERATURE REVIEW 4
2.1 THE KNOCK PHENOMENON 4
2.2 THE CAUSES OF KNOCK 10
2.2.1 Cyclic variation of knock 10
2.3 THE EFFECTS OF KNOCK 13
2.3.1 Erosion damage 14
2.3.2 Heat flux 23
2.3.3 Other forms of knock damage 27
2.3.4 Pre-ignition and knock 27
2.4 KNOCK INTENSITY MEASUREMENT 29
2.4.1 Knock detection techniques 29
2.4.2 Knock intensity parameters 31
2.4.3 Discussion 36

3. DAMAGE INVESTIGATION 38
3.1 OBSERVATIONS 39
3.1.1 Erosion damage evidence 39
3.1.2 Piston seizure evidence 43
3.1.3 Piston ring and land failures 43
3.2 DISCUSSION OF DAMAGE SURVEY 45
3.2.1 Erosion damage mechanism 46
3.2.2 Piston seizure mechanism 48
3.2.3 Piston ring and land failure mechanisms 49

4. EROSION INVESTIGATION 50
4.1 DETONATION MODEL 51
4.1.1 Ethylene-oxygen detonation simulations 52
4.1.2 Effect of fuel type and mixture strength on detonation . . 54
4.1.3 Effect of initial pressure and temperature on detonation 55
4.1.4 Sensitivity analysis of initial conditions 56
4.1.5 Effect of engine operating conditions on detonation 57
4.1.6 Proposed knock intensity-erosion criteria 59
4.2 THERMAL STRESS ANALYSIS 61
4.3 DETONATION CHAMBER EXPERIMENTS 64
4.3.1 Apparatus 65
4.3.2 Experimental method 66
4.3.3 Results and discussion 66
4.4 ENGINE TESTS 70
4.4.1 Development of experimental method 70
4.4.2 Experimental method 72
4.4.2 Results and discussion 73
4.5 QUANTIFICATION OF EROSION DAMAGE 79
5. HEAT FLUX INVESTIGATION 80
5.1 RING GAP INVESTIGATION 83
5.1.1 Theoretical development 83
5.1.2 Experimental study of ring gap 87
5.2 RING SEIZURE AND YIELD STUDY 90
5.2.1 Analysis of strain in a seizing ring 90
5.2.2 Experimental study of ring yield 91
5.2.3 Results and discussion 92
5.3 RING GROWTH STUDY 94
5.3.1 Experimental study of ring growth 95
5.3.2 Results and discussion 95
5.4 RING DAMAGE MECHANISMS 97
5.5 PISTON SEIZURE MECHANISMS 98
5.6 QUANTIFICATION OF HEAT FLUX DAMAGE 99

6. PATHWAYS TO KNOCK DAMAGE 103
6.1 EROSION PATHWAY 104
6.2 HEAT FLUX PATHWAY 105

7. CONCLUSIONS AND RECOMMENDATIONS 107

8. REFERENCES 110

APPENDIX A: Piston specimen data sheets A1
APPENDIX B: Detonation model B1
APPENDIX C: Thermal stresses C1
APPENDIX D: Detonation chamber tests D1
APPENDIX E: Engine erosion study E1
APPENDIX F: Ring gap investigation F1
APPENDIX G: Ring seizure and yield G1
APPENDIX H: Ring growth H1
APPENDIX I: Detonation model - BASIC computer code I1

LIST OF FIGURES

		Page
1.	Effect of geometry on position of end-gas vortices [46]	17
2.	Damage values from endurance tests [47]	19
3.	Spark timing versus surface temperature [48]	24
4.	Cylinder-head temperature versus spark timing [50]	25
5.	Heat flux into wall opposite to auto-ignition zone [51]	25
6.	Knocking pressure trace [41]	32
7.	Filtered pressure trace [41]	32
8.	Specimen #1	39
9.	Specimen #2	40
10.	Specimen #3	40
11.	Specimen #4	41
12.	Specimen #5	42
13.	Eroded cylinder-head	42
14.	Specimen #6	44
15.	Top ring inside bore (from specimen #6)	44
16.	Progressive erosion damage	47
17.	Initial blow-by damage	48
18.	Progressive blow-by damage	48
19.	Theoretical and experimental velocities (ethylene detonation)	52
20.	Theoretical and experimental pressures (ethylene detonation)	53
21.	Detonation pressure vs equivalence ratio	54
22.	Detonation pressure vs initial pressure	55
23.	Detonation pressure vs initial temperature	55
24.	Sensitivity analysis	56
25.	Detonation pressure vs compression ratio	57
26.	Comparative thermal stresses in a 10 mm wall	62
27.	Plan view of detonation chamber	64
28.	Section through specimen-end of detonation chamber	65
29.	Regions evaluated for damage	66
30.	Effects of mixture strength on damage intensity	67

31. Detonation pressure and temperature vs mixture strength 67
32. Effect of specimen temperature on damage intensity 68
33. Spacer plate showing position of specimen 71
34. Specimen geometry 71
35. Engine specimen showing erosion damage 72
36. Micrograph from piston #2 73
37. Micrograph from engine erosion test 73
38. Micrograph from detonation chamber specimen 74
39. Pressure differential necessary to cause bending of specimen 74
40. Erosion damage intensity as a function of knock intensity factor 75
41. Erosion damage intensity as a function of cylinder pressure at knock 77
42. Modelled detonation pressure for engine operating conditions 77
43. Ring gap closure and damage 81
44. Experimental and theoretical results based on mean pressure amplitude of all cycles 88
45. Experimental and theoretical results based on mean pressure amplitude of knocking cycles alone 89
46. Plastic strain vs test temperature 92
47. Lateral ring growth as a function of temperature 96
48. Safety margin as a function of knock intensity 101
49. Knock damage pathways 103

CHAPTER 1

INTRODUCTION AND RATIONALE

Knocking combustion in spark-ignition engines is a well known phenomenon that has been studied for many years [1,2]. It has long been known that knock is able to damage and in many cases destroy engines, and is thus one of the major factors limiting engine performance and efficiency.

Much research has been performed to understand and quantify the processes causing knock [3,4]. The development of more knock resistant fuels and anti-knock additives to replace lead-based compounds has been the focus of more recent investigations [2,5]. Detailed chemical-kinetic models of auto-ignition have been used to gain insight into the causes of knock [6,7], but rarely the effects. Other work has seen engines optimised for knock-free performance [8,9].

The conventional philosophy in engine and fuel development is to avoid knock by invoking generous safety margins in terms of fuel and operating conditions. In terms of fuel-derived anti-knock properties, these amount to additional refining and production expenses, while for engine optimization there is fuel wastage associated with knock-free safety margins [10].

Knock research has focused primarily on factors causing or preventing knock, the assumption being that any knock whatsoever is detrimental to engine durability. Hence, the CRC Octane rating procedure uses an arbitrarily chosen knock intensity and standard reference fuels as the basis for comparing the knock resistance of fuels [11]. This rating gives no indication of the damage potential of fuels and engines under knocking conditions.

However, it has been found, that knock under certain conditions or below a certain intensity is not damaging, and in some cases is beneficial to higher power output [12,13,14]. Also, knocking combustion has been shown to significantly reduce unburned hydrocarbon emissions [15]. In this regard the measurement of knock is somewhat contentious with various researchers using different means of detection and definitions of knock intensity. This leads

The investigation into local pressure-temperature transients included a theoretical analysis, detonation chamber tests and experiments performed on a modified Ricardo E6 research engine. A model describing detonation waves was developed to gain an understanding of the parameters controlling the intensity of these waves. The effects of fuel composition, air-fuel ratio, initial temperatures and pressures were simulated. The detonation chamber tests were used to validate the accuracy of the model, as well as test the effect of operating conditions on erosion damage. An analysis of the thermal stresses in the walls was undertaken to determine the magnitude of their contribution towards erosion damage. The engine tests were used to measure the magnitude of erosion damage under various conditions, and to test the validity of the predictions made by the theoretical analysis.

The mechanisms of knock damage due to heat flux were investigated by means of engine and bench tests. These experiments were aimed at gaining an understanding of the influence of knock on thermal expansion, leading to ring and/or piston seizure. Tests were performed on an instrumented CFR engine to determine the direct effect of knock on ring gap closure. Further experiments were performed on a specially designed high temperature rigs to investigate the permanent strains occurring in compression rings subjected to an equivalent knocking environment.

From this research, the relationship between these various modes of failure were deduced, resulting in an understanding of the pathways leading from knock to damage.

Ultimately these studies were used to gain a broad understanding of the mechanisms of damage under knocking combustion, and to identify knock intensity parameters that describe the potential to cause damage.

CHAPTER 2

LITERATURE REVIEW

Before addressing the subject of knock damage, some relevant aspects of the knock phenomenon are first considered.

2.1 THE KNOCK PHENOMENON

Knock is characterised by a non-uniform pressure distribution in the combustion chamber which is manifested as pressure oscillations in the cylinder [16]. This means that within the combustion chamber, there exists a shock wave (or series of waves) moving at sonic or greater velocities. These waves resonate within the chamber, usually at frequencies above 6.5 kHz (dependent on chamber shape, gas temperature and composition) and die out during the expansion stroke. The term "knock" describes the audible resonance of the engine structure in sympathy with the gas vibrations.

Historically, two main theories have been proposed as possible explanations for these observations:

(1) **Knock is a detonation process** whereby a shock front is thought to develop from the acceleration of the regular, spark initiated flame which changes into a detonation wave consuming the unburned end-gas at supersonic velocities. The energy released by the chemical reaction serves to maintain the shock front immediately ahead of the reaction site. Detonation waves of this description are typically observed when studying the combustion of flammable gases in long tubes. Under this theory, the shock wave must initially travel into the end-gas. For many years, the term "detonation" was used synonymously with "knock". In the context of this thesis, the phase "detonation theory of knock" is taken to mean the acceleration of the regular flame.

(2) **Knock is an auto-ignition phenomenon**, where a body of the end-gas is brought to a near homogeneous reaction under the influence of the high temperatures and pressures established under the combined action of the piston movement and combustion compression of the end-gas. The shock wave should be seen to originate in the end-gas region (ahead of the normal flame front) and travel into the burnt-gas region.

The phenomenon of knock taxed the ingenuity of the early researchers because the speed with which the events occurred made it an extremely difficult subject to study. It was initially suspected that knocking might be a detonation phenomenon and, in 1947, Miller reported that he had obtained conclusive photographic evidence of a detonation wave originating in the end-gas region [17]. However, the evidence reduced to an interpretation of a single frame, which provoked a lively discussion at the time. Miller's attempts to obtain higher frame speeds were confounded by equipment problems and questionable results were produced.

Despite the ascendance of the auto-ignition theory in the intervening years, there still exist adherents to the detonation theory of knock as illustrated by a 1993 publication [18]. This popular automotive handbook describes knock as occurring "when the flame propagates near the speed of sound".

Over the last 40 years, the evidence supporting the auto-ignition theory of knock has accumulated convincingly and somewhat over-shadowed the historical detonation theory [19,20,21].

As early as 1923, Ricardo had adopted the auto-ignition theory of knock [22]. At that time it was assumed that the auto-ignition phenomenon was a near instantaneous, homogeneous reaction of the end-gas. In 1949 Male demonstrated that the auto-ignition process was neither homogeneous nor instantaneous, by means of ultra-high speed photographs [23]. The results showed that auto-ignition was initiated at many discrete nuclei from which combustion proceeded as a host of radially propagating fronts. The radially expanding combustion zones were observed to be associated with shock waves. The conclusion that could be drawn from this work (although not by Male) is that auto-ignition is the cause of the shock waves and hence the cause of knock. Another process was responsible for the transition from auto-

ignition to shock waves.

The auto-ignition theory was further corroborated by Franklin and Murphy, who attempted to reduce knock intensity by milling a groove on the piston crown near the end-gas region [24]. Their piston modification was intended to demonstrate the detonation theory of knock. The experimental results showed an increase in knock intensity with the groove. If the detonation theory was correct, then a sudden increase in the flame front area would break down the detonation wave. This was clearly disproved by their findings, much to their consternation. They concluded that the shock waves originated within the end-gas zone (and not from outside as they had originally surmised).

In a review article, Litzinger followed the development of knocking combustion chemistry from 1928 to the present [25]. The objective of most of the reviewed research was to analyse the causes of knock and in order to avoid its occurrence. As a result, much of the detailed chemistry leading to auto-ignition is now understood, but little of this work encompasses the effects of the auto-ignition process. With the assumption of a homogenous end-gas, this work could not be used to explain the formation of shock waves inside the end-gas region.

The distinction between the auto-ignition theory and detonation theory of knock has become somewhat blurred by recent developments. In 1984, Oppenheim persuasively argued that the mixture in engines is heterogeneous and that a rapid reaction is initiated at exothermic centres with strong interaction thereafter between pressure pulses and reaction chemistry [26]. More recently, Goyal, Maas and Warnatz have combined detailed models of the chemistry with the generation of a pressure wave in a one dimensional system [27]. An exothermic centre may arise from both local temperature or compositional heterogeneity. Appreciable temperature gradients may remain in the end-gas region as a result of turbulence [28], and compositional heterogeneity may arise from imperfect mixing of the residual gas from the previous cycle. The model derived by Goyal et al illustrated two distinctly different consequences of auto-ignition derived from hot-spots. Ignition results in a pressure wave propagating away from the hot-spot and heating the reactive mixture. In certain instances (where the temperature gradient around the hot-spot is low), this heating is sufficient to spontaneously ignite the sensitised mixture, causing a large temperature increase. The reaction wave which is

formed, moves with a higher velocity than the pressure wave (due to its higher temperature) and would finally merge with the latter forming a detonation front. Under other conditions (where there is a very high temperature gradient around the hot-spot), the compression heating is not sufficient to ignite the mixture spontaneously. Instead, ignition occurs only after an induction time and a deflagration flame ensues, consuming the end-gas without producing any pressure discontinuity. Goyal's work thus shows that auto-ignition is a precursor to knock, but that auto-ignition will not always result in knock.

These works show that detonation is a process occurring after auto-ignition, and not the acceleration of the regular flame as originally surmised.

In a recent study by Pan and Sheppard the effect of multiple exothermic centres was investigated using a 2-dimensional fluid dynamic and chemical interaction simulation [29]. A most significant finding concerned the case of sequential auto-ignition of multiple centres. For two exothermic centres characterised by large temperature gradients (which would normally yield benign deflagration waves), it was found that the pressure waves produced by the first ignition could modify the temperature gradient of the second centre, resulting in a violent "developing detonation" of the second centre. This work thus places a higher probability of the detonation form of ignition occurring, as optical data from engines indicates the presence of multiple ignition centres within the end-gas.

König and Sheppard [30] and König et al [31] used high speed photography and laser schlieren filming on a modified 2-stroke engine with optical access to investigate the knock phenomenon. They reported that all knocking cycles were preceded by visible auto-ignition of the end-gas, which was generally at multiple-centres in that region. Shock waves were observed to radiate from these centres and the authors characterised these as "developing detonation". It was also observed, that occasionally some cycles exhibited auto-ignition without knock. In these cases the end-gas auto-ignition developed into deflagrations (with observable flame fronts) and behaved like extensions of the main flame front, thus confirming the analysis forwarded by Goyal et al [27]. This process was considered benign and possibly beneficial in accelerating combustion of the unburned mixture. The authors found no sign of homogeneous auto-ignition of the end-gas (the original assumption of most chemical models).

Under knocking conditions, the combustion behaviour in the crevice regions is of particular relevance, since this is where erosion damage is known to occur. Klein [32,33] developed a two-dimensional reactive-gasdynamic model to examine conditions in the crevice region between the piston and cylinder, above the first compression ring (henceforth referred to as "top-land region"). A similar model was used by Maly et al [34] to explain some of their experimental work. The aim of this work was to determine why piston erosion occurs at the top-land, a region which under normal operating conditions, is not exposed to combustion conditions (due to flame quenching). By assuming an in-coming shock wave established by the auto-ignition process, the models predicted the various types of interaction of the diffracted and reflected waves that could occur in a simulated 2-dimensional top-land. Their simulations showed that:

- The pattern of density and velocity contours inside the crevice is dependent on the temperature sensitivity of the ignition process.
- The flow pattern at the simulated piston top-land surface is especially influenced by the initial conditions (of the incoming shock as well as the thermo-chemical properties of the mixture in the crevice).
- Very strong chemico-hydrodynamic coupling occurs near the walls due to the reflected shock waves causing localised compression heating. This strong coupling means that the resulting energy release rate (from the compression zone) is high enough to precipitate detonation close to the walls.
- The modelled data indicates severe wall loading in the vicinity of the simulated piston top-land region.

The main source of the auto-ignition sites (or exothermic centres) have been traced to turbulent eddies which have the effect of thermally insulating a small volume of the gas from the cooling end-gas region. Thus, the core of turbulent eddies are heated to near adiabatic temperatures. Some researchers [35,36] have proposed that the main source of this heterogeneity is the roll-up vortex at the edge of the piston crown, while others [37] contend that the general combustion turbulence is sufficient to produce these effects.

To summarise, it is currently understood that knock is the result of the auto-ignition of preferential sites within the end-gas under conditions which favour the subsequent

development of a detonation wave. This wave is able to penetrate into the top-land crevice, where it is refracted and reflected according to the geometry of the region and causes the energy release of the remaining unburnt gas in the crevice. The shock wave is also responsible for exciting the combustion chamber into resonance. Thus the progression of this phenomenon follows a specific path: auto-ignition to detonation to knock. Each of these terms indicates a specific process. However ***knock*** *has been accepted as the term describing the whole process.*

2.2 THE CAUSES OF KNOCK

Although it has been found that auto-ignition does not always result in knock and it has been argued that there may be a means of preventing auto-ignition from forming shock waves, this has not been accomplished in conventional spark-ignition engines. Thus, the current understanding of the causes of knock lies in the wealth of knowledge concerning the causes of auto-ignition.

It has been established that the propensity of the end-gas to auto-ignite is determined by the chemical composition and the temperature-pressure-time history of the mixture. Exhaustive testing has been performed on all forms of compounds to determine their ability to resist knocking and it is now understood how engine parameters and operating conditions influence auto-ignition. Much of these details are now standard textbook material [3,4,16].

However, it must be noted that although these parameters (temperature, pressure, time and composition) have been well researched in terms of their effect on the occurrence of knock, little work has been done to determine their effect on post-knock conditions, and hence their damage potential. Furthermore, results of research using a "knock intensity" parameter are dependent on the particular definition used. This is a contentious issue and will be discussed in section 2.4.

Another complication in quantifying and studying knock is the cyclic fluctuation of the parameters causing auto-ignition, and hence the cyclic variability of the knock itself.

2.2.1 CYCLIC VARIATION OF KNOCK

The fluctuating nature of the knocking process is due partially to the random nature of the early combustion development (shortly after the firing of the spark). Much work has been performed in this area [38,39] as the cyclic variation of the combustion process is a serious restriction to engine and fuel optimization in its own right. Typical results of this work [40] have shown that under steady-state conditions, the time from spark to 50% mass fraction burned may vary by as much as $\pm 60\%$ of the mean time. These variations are thought to

be caused by cyclic fluctuations of the local thermal and compositional conditions at the spark-plug at the time of ignition. The corresponding effect on auto-ignition can be viewed simplistically as a virtual cyclic variation in the ignition-timing.

Cyclic variation is further exacerbated by the local (thermal and compositional) fluctuations occurring in the end-gas region. Chun and Heywood [41] investigated the variability of the knock process, in an attempt to correlate end-gas conditions to knock intensity. The work utilised a large amount of captured data from which it was shown that knock should be viewed as a stochastic event, with no periodicity and possessing a normal distribution in terms of data correlated. In order to increase the confidence of these correlations the authors performed similar tests using an ignition system which was able to spark once every two cycles, thereby minimizing the residual mass fraction and attempted to create consistent conditions at the spark event and in the end-gas. This produced a much closer correlation, but still with appreciable cyclic variation.

Leppard [42] performed statistical analyses on knock data from a multicylinder engine in order to study the cycle-to-cycle variation of knock occurrence. Of particular interest was a scatter plot of knock intensity as a function of TDC-pressure. The use of the TDC-pressure as the independent variable removed the stochastic aspects of early flame development. Having eliminated this effect, it was still found that the knock intensity varied considerably, yielding a correlation coefficient of only 0.55. It was concluded that knock occurrence and intensity are random and depend solely on the conditions of each individual cycle.

This stochastic aspect of auto-ignition has a further impact on knock research. Due to the effects discussed above, there is a gradual transition from normal to knocking combustion [43]. For instance, as the spark timing is advanced, at first only a few cycles begin to knock, with the "intensity" of the individual knocking cycles being a separate variable. Further timing advance increases the percentage of knocking cycles until all cycles are knocking. This creates difficulties in establishing a threshold for the occurrence of knock. It also poses the critical question of whether to include the non-knocking cycles in the definition of knock intensity.

In summary, knock is caused by auto-ignition, which is dependent on the thermodynamic and compositional history of each cycle. There is significant cyclic variation in these histories, resulting in a random cyclic fluctuation in both the measured knock intensity and the frequency of occurrence of knock.

2.3 THE EFFECTS OF KNOCK

The damaging effects of knock were recognised at the turn of the century, resulting in the search and discovery of organo-lead compounds as the most effective knock inhibitors [5]. In pioneering work, Harry Ricardo reported the various types of damage encountered [22]. The following were presented in the form of a warning against operating an engine under knocking conditions:

(1) Primary knock damage in the form of pitting or erosion was found on the piston at regions furthest away from the spark plug. Erosion of other surfaces in the combustion chamber was also noted.

(2) Piston-rings were found to stick in their grooves which was thought to be due to the presence of free carbon particles.

(3) General overheating of internal surfaces was observed and attributed to the scouring of the protective quench zone by the pressure pulses.

(4) As a consequence of (3), continuous knock would eventually result in pre-ignition and a run-away condition causing seizure.

The last two damage mechanisms (3 and 4) result from additional heat flux into the chamber and piston surfaces. Aspects of knock-induced heat flux have been systematically researched and will be discussed in a following section. In general, other types of damage (erosion, jammed rings, etc) have not been well investigated and that which is available will be discussed in a separate section dealing with specific reports of knock related damage.

taken to imply that damage was caused mechanically by the high-pressure shock waves and that this may be aggravated by extremely high-temperature gradients at the piston surface. The authors concluded that such extremely thin, high-temperature layers were disintegrated mechanically without leaving residues.

An experiment was also performed where a piston crown was subjected to 22 kHz excitation in an ultrasonic tank. Comparing this specimen to that from knock damage by means of scanning electron microscopy showed very similar damage surfaces, further reinforcing the authors' conclusion regarding purely mechanical damage.

Renault [44] performed steady speed endurance tests on a 4-cylinder engine from which it was shown that the exhaust gas temperature is dramatically reduced at the onset of knock-pre-ignition runaway. By using three primary reference fuels, the engine could be operated at various knock intensities bordering on the runaway exhaust gas temperature for long periods. From these tests the author produced a graph (with only 3 data points) illustrating piston erosion rate as a function of exhaust gas temperature. The erosion rate was shown to be inversely proportional to exhaust gas temperature, though, unfortunately the method of measuring this erosion rate was not described nor the units defined.

2.3.1.2 EFFECT OF OPERATING CONDITIONS

Essig [14] performed tests on a production engine instrumented with thermistors embedded in the pistons and pressure transducers. Endurance tests were performed under steady-state knocking conditions and the piston was periodically removed and inspected microscopically.

Under mild knock, primary damage in the form of erosion was found to begin on the top-land at about 1.5mm below the crown in the region furthest from the spark plug. Erosion spread around the perimeter in both directions, eventually spreading over the top to the squish zone. It also spread downwards to the edge of the ring groove as knock continued. Microscopic examination revealed that the erosion surface was covered with small fused beads and deep cavities. Metallographic section revealed crack networks of up to 40μm below the surface. The difference between the alloy melting point (on surface) and mean piston temperature indicated to the author that extremely high local temperature had

occurred. A thin-film thermocouple on the head side of the squish gap showed that the magnitude of the cyclic temperature change during heavy knock was 3 times that of normal combustion. Little discussion and no conclusions were presented in this paper. The fact that molten structures were observed, whilst only sub-molten temperatures were recorded could be explained by considering the profile of an eroded surface compared to a thin-film thermocouple surface. The rough, eroded surface comprises protuberances and valleys, which present a greater surface area for convective heat transfer, together with a reduced conductive path to the deep wall material. This would result in high local temperatures at the extremities of the surface. Conversely, the fact that the thermocouple was operating implied that it had not yet been eroded, and therefore possessed a smooth surface. In comparison to the erosion zone, the smooth surface would imply worse convective heat transfer with better conductive heat transfer and hence the surface temperatures would be relatively lower. It is therefore quite possible for extreme temperatures to occur at the upper surface of the eroded zone whilst much lower values are recorded by a surface thermocouple.

Lee and Schaefer [45] attempted to correlate known damage areas with local temperatures and pressures. Knock intensity was defined as the maximum pressure amplitude. The authors investigated whether the local pressures in the end-gas region were higher than in other areas. The engine was instrumented with two pairs of pressure transducers, one pair in the liner and cylinder head on the spark side and the other pair on the opposite side to the spark plug. A frequency distribution of peak pressures from 100 consecutive cycles was developed for different knock intensities. Under heavy knock the transducer pair furthest from the spark showed that 39% and 27% of the cycles exceeded 180 bar. Transducers closer to the spark registered only 17% and 9%. The highest value of 39% was recorded from the transducer positioned on the cylinder liner opposite the piston top land. The authors admitted that the problem of detailed statistical comparisons was confounded by the measurable limit of these transducers being in the region of 180 bar. However, they felt that these trends were sufficiently convincing to state that the pressure amplitudes were highest in the end-gas region.

The film thermocouple results revealed maximum temperatures of up to 250°C, much less than the melting point of the piston alloy (450°C). It was stated that these temperatures would cause a 50% reduction in the fatigue strength of the material. It was concluded that

occurred. A thin-film thermocouple on the head side of the squish gap showed that the magnitude of the cyclic temperature change during heavy knock was 3 times that of normal combustion. Little discussion and no conclusions were presented in this paper. The fact that molten structures were observed, whilst only sub-molten temperatures were recorded could be explained by considering the profile of an eroded surface compared to a thin-film thermocouple surface. The rough, eroded surface comprises protuberances and valleys, which present a greater surface area for convective heat transfer, together with a reduced conductive path to the deep wall material. This would result in high local temperatures at the extremities of the surface. Conversely, the fact that the thermocouple was operating implied that it had not yet been eroded, and therefore possessed a smooth surface. In comparison to the erosion zone, the smooth surface would imply worse convective heat transfer with better conductive heat transfer and hence the surface temperatures would be relatively lower. It is therefore quite possible for extreme temperatures to occur at the upper surface of the eroded zone whilst much lower values are recorded by a surface thermocouple.

Lee and Schaefer [45] attempted to correlate known damage areas with local temperatures and pressures. Knock intensity was defined as the maximum pressure amplitude. The authors investigated whether the local pressures in the end-gas region were higher than in other areas. The engine was instrumented with two pairs of pressure transducers, one pair in the liner and cylinder head on the spark side and the other pair on the opposite side to the spark plug. A frequency distribution of peak pressures from 100 consecutive cycles was developed for different knock intensities. Under heavy knock the transducer pair furthest from the spark showed that 39% and 27% of the cycles exceeded 180 bar. Transducers closer to the spark registered only 17% and 9%. The highest value of 39% was recorded from the transducer positioned on the cylinder liner opposite the piston top land. The authors admitted that the problem of detailed statistical comparisons was confounded by the measurable limit of these transducers being in the region of 180 bar. However, they felt that these trends were sufficiently convincing to state that the pressure amplitudes were highest in the end-gas region.

The film thermocouple results revealed maximum temperatures of up to 250°C, much less than the melting point of the piston alloy (450°C). It was stated that these temperatures would cause a 50% reduction in the fatigue strength of the material. It was concluded that

although melting point temperatures were not encountered, thermal loading could nevertheless contribute to erosion damage by means of reducing the fatigue resistance of the material. As argued previously, the relatively low thermocouple readings do not preclude melting of the upper erosion surfaces, after erosion has occurred.

2.3.1.3 EFFECT OF GEOMETRY AND MATERIAL

Maly and Zeigler [46] discussed the effect of end-gas geometry with respect to the location of knock-induced erosion. They argued that around TDC, the piston generates a squish flow in the form of small vortices. They proposed that the position of these vortices correlated with known damage sites for various chamber geometries. Figure 1 shows these ideas:

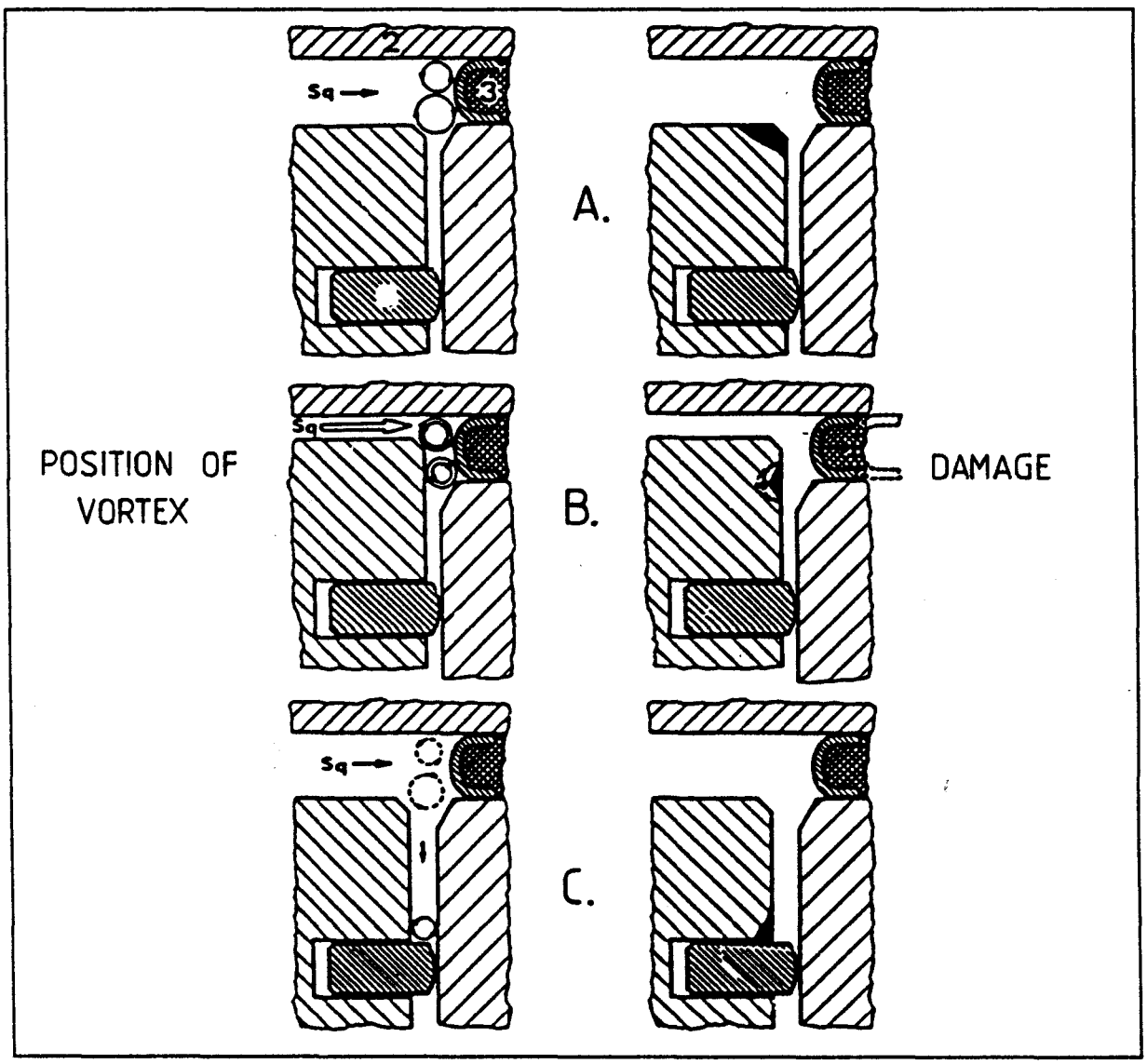

Figure 1: Effect of Geometry on Position of End-Gas Vortex [46]

Piston #1: Large piston-bore clearance and chamfer at edge of first ring groove (standard piston configuration).

Piston #2: Small piston-bore clearance (reduced by 0.2 mm relative to standard) and chamfer at edge of first ring groove.

Piston #3: Small piston-bore clearance, no chamfer at edge of first ring groove.

Piston #4: Large piston-bore clearance, no chamfer at edge of first ring groove..

Piston #5: Large piston-bore clearance, chamfer at edge of first ring groove and groove machined in the middle of top-land.

Piston #6: Large piston-bore clearance, chamfer at edge of first ring groove and oil spray piston cooling.

Piston #7: Large piston-bore clearance, chamfer at edge of first ring groove and nickel coating.

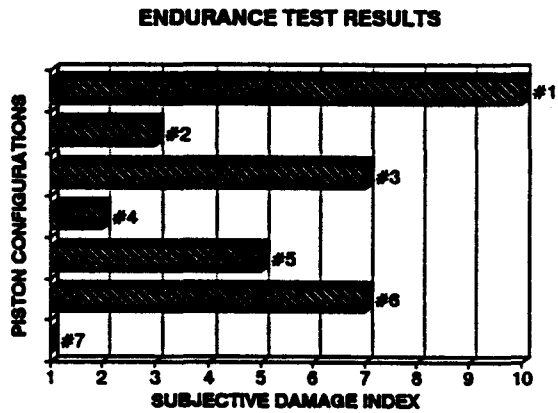

Figure 2: Damage values from endurance tests [47]

Using a 20 hour test, they ran the engine at steady-state knocking conditions. They used an accelerometer to determine the "knock intensity" and reported that "conditions were controlled to maintain an average of 2° to 3° ignition timing into knocking combustion". However, they did not explain how this was maintained over the 20 hour test. They found that the standard piston for this engine (#1) showed significant top-land erosion which they arbitrarily assigned a subjective damage index of 10 on a scale where 1 denotes no damage. The remaining configurations (#2 to #7) were subjected to a similar procedure and a corresponding damage value assigned by comparison to piston #1 These results of these tests are shown in figure 2.

Prior to discussing these results, it should be noted that the authors were mainly interested in proving the virtues of the nickel coating, and made no attempt to explain any of the other results. This is unfortunate, as these seem to be unique data in the field of study.

The results concerning the effects of ring-groove chamfer and piston-bore clearance are

summarised in the table below:

GROOVE CHAMFER	PISTON CLEARANCE	DAMAGE LEVEL
Yes	Large	10
No	Large	2
Yes	Small	3
No	Small	7

Clearly, there can be no conclusion concerning the effect of clearance or chamfer from these conflicting data. However, the oil cooling tests did show marginal benefits of reduced material temperature on erosion damage (at least under the operating conditions tested). Although the milled recess showed some improvement, it cannot be deduced from this single configuration exactly which aspect of the groove was responsible for the improvement. For both the chamfer and the recess, the parameters affecting the damage intensity could be any combination of the following: position, shape, width, depth or volume.

Numerous tests on the nickel coated piston (#7) confirmed it's complete resistance to erosion damage under the conditions tested. The authors attributed this to the "hot tensile strength and ductility of the nickel layer which protected the aluminium from the high gas pressure damage".

Lee and Schaeffer [45] also describe heavy knock endurance tests performed on a 4-cylinder engine fitted with aluminium pistons, two of which were surface coated with 20 μm of iron. The magnitude of the knock intensity was not reported. After 2.5 hours of operation the uncoated pistons showed signs of erosion knock damage, but not the coated ones. The authors concluded that the "tougher" materials are able to withstand the mechanical and thermal stresses of knock. The protection mechanism was described as a thin, tough diaphragm with high elasticity protecting the weaker base material.

2.3.1.4 SIMULATED EROSION DAMAGE

A recent paper by Maly et al [34] has reported the first direct observations of surface erosion caused by controlled detonation (within the context of knock). Furthermore, this is the first and only attempt to theoretically and experimentally analyse the knock process in terms of the effects on surface erosion of boundary and initial conditions.

One of the aims of this work was to validate a numerical simulation of the end-gas crevice region (discussed in section 2.1). Another goal was to develop an understanding of the magnitude of wall loading as a result of a detonation wave.

The experimental method adopted by these researchers was to use a detonation chamber in which near-plane detonation waves were allowed to impinge on aluminium specimens. The detonation waves were produced regularly (about 1 Hz) by spark-ignition of a steady flow oxygen-ethylene mixture at atmospheric pressure. This mixture was chosen on the basis that it would detonate at atmospheric pressures and would yield similar (specific) energy content to air-gasoline mixtures in the end-gas of a typical engine (just prior to auto-ignition). The damage produced after 10 000 to 200 000 shots (depending on operating conditions) was reported to be microscopically similar to knock-induced piston erosion.

The shapes of the specimens were chosen to simulate a two-dimensional piston top-land geometry, although the authors admit that complete similitude could not be established. The authors tested three top-land geometries, whose shapes concerned the effect of radii at either the inner or outer edge of a squish lip on a piston crown. High speed Schlieren diagnostics via an optical access, allowed the authors to record the temporal positions of density gradients in the specimen region.

The optical results from the detonation chamber showed close similarity to conditions predicted by the numerical simulation. Tests performed on aluminium probes showed similar erosion surfaces to that encountered with knock-induced erosion. The different shaped probes indicated that chamber geometry had a strong influence on the position and magnitude of the erosion damage. Having validated the numerical model using the detonation chamber, the authors simulated typical end-gas conditions for a knocking engine. The results of these

simulations were used to estimate the piston wall loading by using gas pressures as a measure of the direct wall stresses. A thermal contact model was used to estimate the wall thermal stresses. It was found that the pressure stresses could be in the vicinity of 35 MPa to 45 MPa, depending on the assumed initial conditions. In general, the thermal stresses were found to be less than half the values of the direct pressure stresses. The authors concluded that, from this data, both the direct and thermal stresses were responsible for erosion damage.

It should be noted that the thermal stress analysis in this work was based on the product of the coefficient of expansion and the change in the wall surface temperature. This simplistic stress analysis can be regarded as yielding an order-of-magnitude estimate. The result of this calculation is a single compressive stress level which is presumed to occur in the surface of the wall.

2.3.2 HEAT FLUX

The evidence of piston seizure as a consequence of knock, indicates that heat flux is another form of knock damage.

Betz and Ellerman performed tests on an instrumented engine [13]. NTC Temperature probes were mounted on the piston crown edge (1mm below the surface), near the expected end-gas region. The increase in crown edge temperature as a function of ignition advance was found to be linear in the no-knock and trace knock regions. Under medium and heavy knock, there was a significant increase in the piston temperature (of up to 100°C). Knock intensity was defined as a cumulative pressure amplitude, to be discussed in section 2.4. The measured knock intensities were then compared to the piston temperature increases. No correlation was undertaken, but it was stated that the change in knock intensity was a good indicator for the associated piston temperature increase.

French and Atkins [48] placed a number of thermocouples in various positions on the surface of the head and outer edges of the piston. With the engine running at steady-state conditions, the spark timing was advanced, and the mean surface temperatures measured. Two reference fuels were used, one resulting in knock and the other knock-free over the whole spark timing range. In the case of the knocking fuel, the spark advance acted as a means for increasing the knock intensity.

Typical curves showing the marked increase in piston temperature under knocking conditions are shown in figure 3. It was noted that the temperature rise was 10°C higher on the thrust side (opposite side to spark plug) where the eroded piston surface was observed by the authors. In general, the temperature rise of the cylinder head and liner was small representing only 25% of the maximum piston temperature rise.

The authors also used these temperatures to calculate the mean heat flow into the piston, liner and head. It was estimated that under heavy knock a mean increase in heat flux of about 20% occurred at the outer edge of the piston compared with increases of 10% and 30% into the head and liner respectively. The authors stated that these increases were due to the

disturbance of the gas-wall boundary layer by the resonating pressure waves and therefore found it puzzling that the heat flux changes to the various zones were not equal. However they referenced other work [49] which had reported similar results to theirs.

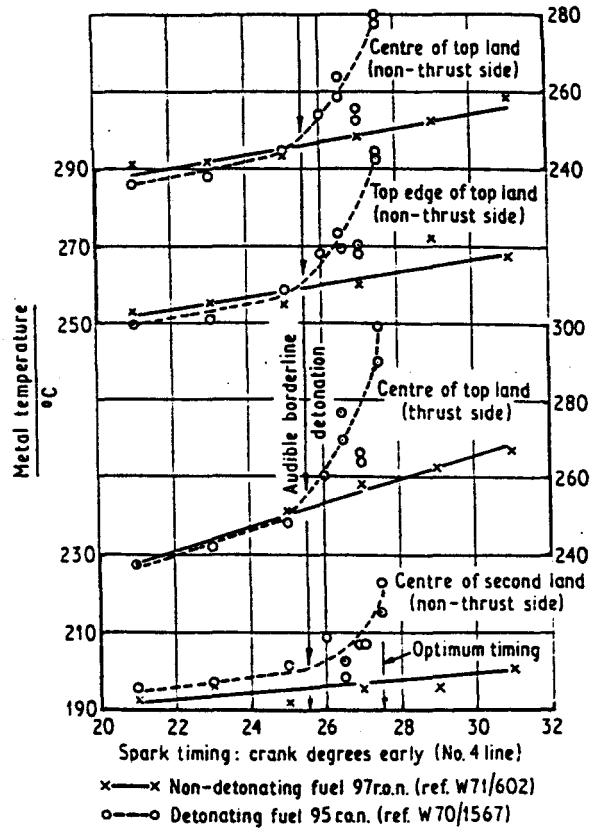

Figure 3: Spark Timing versus Surface Temperature [48]

An explanation for these data may be proposed with a closer look at figure 3. The highest temperature rise occurs around the sides of the piston on the opposite side to the spark plug (centre of top land - thrust side). This indicates that detonation may be occurring around the edge of the piston. Although the global effect is the production of resonating pressure waves (knock), these data are a suggestion that there is a more severe and localised effect causing this increased temperature (and the erosion observed by others). If auto-ignition was occurring in this region (between piston and liner) it would be expected that the head would be partially shielded from the localised occurrence and would only be exposed to the global effect (resonating waves), and would therefore show significantly lower heat flux (10% for the head and 30% for the liner).

Data reported recently by Zhao, Collings and Ma [50] confirmed the localised effect of auto-ignition on surface temperatures, although this was not noticed by the authors (who were interested in other aspects of these data). In this work thermal imaging was applied to the combustion chamber surfaces of an engine run under both knocking and normal conditions. Included in the results was a plot of head temperature (at two different positions on the cylinder head) as a function of spark timing for high and low octane fuel respectively, shown in figure 4. The onset of knock was recorded as 16° and 20° CA BTDC for the low and high octane fuel respectively. As seen in figure 4, position 1, which is near the end-gas zone, is

more sensitive to knock than position 2 which is on the opposite side of the chamber (close to the spark-plug). Although there is clearly a global effect, these data indicate that there is also a localised effect in the end-gas region.

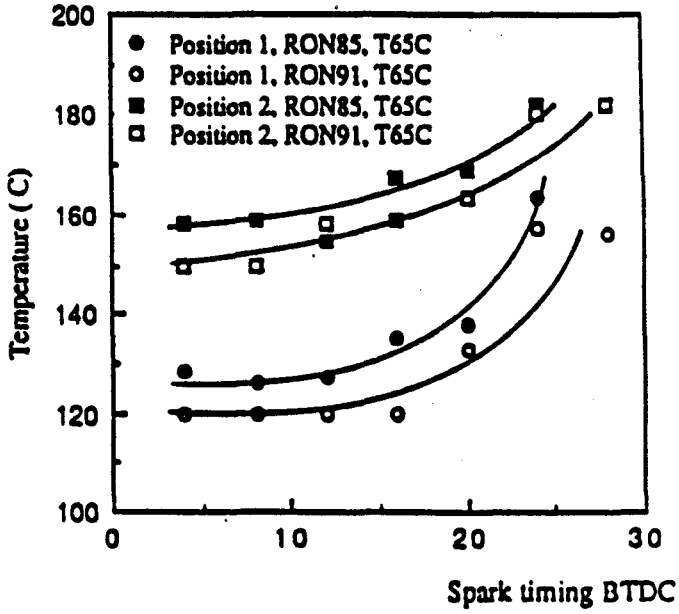

Figure 4: Cylinder Head Temperature versus Spark Timing [50]

Lee and Schaefer [45] tested a single-cylinder engine fitted with 9 film thermocouples arranged around the combustion chamber. The engine was operated under steady-state conditions and knock-induced by either advancing the spark timing or reducing the fuel octane number. It was found that all the thermocouples showed increased surface temperatures with increased knock intensity (measured as maximum pressure amplitude). A correlation of the thermocouple data showed that there was no significant local differences in the wall temperatures in the investigated area due to knock. In other words, the effect of knock intensity on surface temperature was similar for all nine locations tested.

Lu et al [51] used thin film platinum resistance thermometers to measure the instantaneous heat flux at two positions in a combustion chamber under knocking conditions. The fast response of these transducers allowed the heat flux to be plotted as a function of crank angle degrees. Figure 5 shows an example of an instantaneous heat flux trace in the region away from the auto-ignition zone (ie: adjacent to the spark-plug). Flame arrival was reported as 329°CA and the maximum heat flux due to knock occurred at 339°CA, clearly

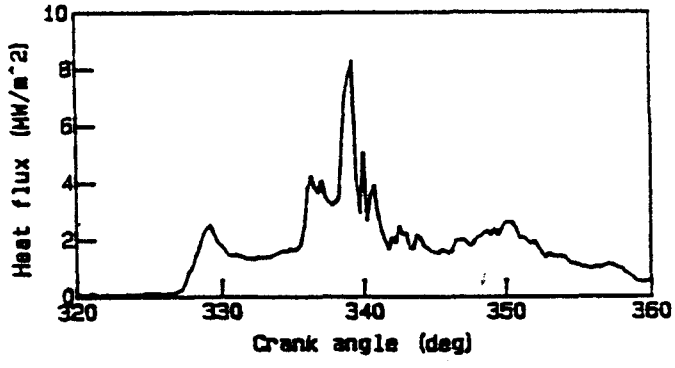

Figure 5: Heat Flux into wall opposite to auto-ignition zone [51]

confirming the global effect of knock on heat flux.

In general, most of the literature cited in this section mentions that the elevated heat flux (under knocking conditions) is caused by the disturbance of the thermal boundary layer at the walls. Effectively, the resonating pressure pulses induce transient gas velocities close to the walls, thus increasing the local heat flux. When looking at the data reported, it is apparent that in some cases, disproportionate increases in heat flux were found in localised regions, while in other cases, only a global effect was measured. No comment was found in the literature concerning these apparent contradictions, however an explanation may be formulated by considering the nature of the resonating pressure waves.

The manner in which the gas in a combustion chamber oscillates (as a consequence of knock) is related to the chamber geometry and gas conditions. The resonance has been explained [52] by the superposition of different modes of vibration (sets of standing waves), the most dominant being the radial and circumferential modes. The circumferential modes exhibit nodes which can be close to the walls (depending on chamber geometry). The position of these nodes may vary for circumferential modes of vibration. However, in the vicinity of these nodes, it is expected that less boundary disturbance will occur compared to other locations. This would explain the apparent contradictions in reported data, in that the position of the thermocouple relative to the resonant gas vibration nodes would effect the results.

In summary, knock results in an additional heat load on the surfaces of the piston and combustion chamber. The magnitude of this elevated heat flux varies with spatial position, but is nevertheless measurable all around the chamber.

2.3.3 OTHER FORMS OF KNOCK DAMAGE

Besides surface erosion, there are other forms of engine damage that have been attributed to knock. Betts [12] reported that breakage of piston lands had been observed in many instances. Examination of the fracture surfaces suggested that this damage occurred through a fatigue mechanism. It was proposed that the piston-lands failed as a result of crack growth initiated in the highly stressed corners in the base of the ring grooves, although the source of these stresses was not discussed.

Betz and Ellerman [13], and Maly and Ziegler [46] also reported cases of cracked and broken piston-lands. They independently theorised that the initiation of crack growth in the root of the ring-groove would be caused by the steep pressure rise of the knock event.

Additionally, it has also been reported [4,20,22] that knock results in rings jamming in their ring-grooves, broken rings and piston seizure. Heywood attributes all these observations (including broken piston-lands) to the elevated heat load, without further comment. It is easily understood that thermal expansion as a result of additional heat load could cause piston seizure. However, the mechanisms by which rings are permanently jammed in their grooves or rings are broken are not easily discernable.

The lack of complete explanation and analysis into these failure modes was recognised as a gap in the literature and was therefore included as an area for study in this thesis.

2.3.4 PRE-IGNITION AND KNOCK

Another related effect of knock concerns the phenomenon of pre-ignition (surface-ignition) which is caused by the elevated heat flux [4,16,53]. This phenomenon effectively replaces the spark with a surface-ignition source with an increasingly advanced ignition timing. This is a positive-feedback process causing heavier knock which reinforces the surface ignition. In this condition, an engine will run very rapidly to destruction unless it is stalled by load or choked by throttle. Knock is not the only cause of pre-ignition and the effects of pre-ignition

ignition (in terms of engine damage) are not always the same as those of knock (eg: melted surfaces). Although pre-ignition may be caused by knock, the phenomenon itself will not be considered in any more detail in this work, as it is a well documented. However, it must be noted that knock may be both the cause or the consequence of pre-ignition.

To summarise, the effects of knock that have been reported in the literature include:

- *Surface erosion of the piston-crown and cylinder-head*
- *Head-gasket failure*
- *Piston-land fracture*
- *Piston-rings jammed in their ring grooves*
- *Broken piston-rings*
- *Piston seizure*
- *Pre-ignition*

2.4 KNOCK INTENSITY MEASUREMENT

In order to test the knock resistance or damage potential of a fuel component or engine parameter, it is necessary to establish a datum for reference. This section is divided into two sections, the first dealing with knock detection techniques and the second with the analysis of data so as to produce a knock intensity parameter.

2.4.1 COMMONLY USED KNOCK DETECTION TECHNIQUES

Many alternative systems have been used to detect and measure knock. The difference between these methods lies in the objectives and resources of the particular research being performed.

The earliest gauge of knock intensity was performed audially and knock intensity evaluated subjectively as trace, medium or heavy knock [22]. The human ear is in fact a very sensitive instrument for detecting the onset of trace knock and is still used today for this purpose.

The ASTM method of rating fuels (RON and MON) tests gave rise to the internationally accepted ASTM Knock Meter [11]. The Octane Rating System (and its test procedure) is an arbitrary scale, historically accepted, and convenient to use.

2.4.1.1 PRESSURE TRANSDUCERS

The pressure transducer in various forms has been the basic instrument used for the study of knock. This instrument is inserted against the wall of the combustion chamber and produces a response to the pressure of the gas. The earliest instruments [22,54] had a very low natural frequency, in the region of 10 kHz, resulting in a very inaccurate representation of the pressure oscillations encountered during knock. More recently pressure transducers for engine testing have resonance frequencies of up to 160 kHz [45], which is much higher than the measured signal (in the region of 6 to 15 kHz). Thus, these transducers respond fast enough to capture the resonating pressure pulses.

The results from work [41,55] using two transducers for each test has shown that, the position of the pressure transducer around the combustion chamber has no effect on the pressure trace, other than a phase difference in the knock oscillations (due to the distance the pressure wave must travel to reach the transducer). Others [29,45] using four transducers each have found that there are peak pressure differences around the chamber, but these peak pressures were at the extreme range of the available transducers. This is a significant observation, if the object of the test is to analyse the nature of the peak pressure in the end-gas zone. It is improbable that the peak pressure in the end-gas zone (at auto-ignition) is the same as that in the rest of the chamber, as erosion damage is usually found in the end-gas region. The conclusion that can be drawn from this work is that modern pressure transducers are capable of monitoring the resonating pulses, but do not respond fast enough to capture the first pulse. Furthermore the positioning of the transducer is critical. The pressure history in the end-gas zone is likely to be much more severe than that of the burnt-gas region even though transducers are incapable of fully measuring the true peaks. It is likely that those researchers using only two transducers had not positioned one of them in the end-gas region, while those using four transducers managed to capture traces very close to the auto-ignition sites. It should also be considered that transducers positioned close to a node (of vibration) would register considerably lower pressure amplitudes of vibration.

2.4.1.2 TEMPERATURE MEASUREMENT

The occurrence of knock increases the heat flux from the gas to the chamber walls and piston. From the early days [54], aircraft engines were instrumented with temperature probes embedded in the cooling fins, which were used as an indication of engine overheating as a result of knock or lean-out. The original ASTM Aviation Octane Number Test used a thermal plug in the cylinder as a means of establishing a reference knock intensity [56].

More recently [19,51,57], fast response surface thermocouples have been developed which, when applied to the surface of the combustion chamber, are able to yield a clearer picture of the cyclic temperatures at the walls. Other than the early ASTM procedure, no attempt has been made to used temperature measurements as a direct means of evaluating knock intensity.

2.4.1.3 ACOUSTIC AND ACCELEROMETER TECHNIQUES

Instrumentation has been developed to characterise knock by means of accelerometers mounted on the engine structure [54,58] and by microphones recording engine noise [55].

Both these techniques are recording the engines structural response to the knock-induced pressure oscillations. By comparing data from normal combustion to those under knocking conditions it is possible to determine whether or not knock is occurring. Furthermore, the intensity of the signal is used as a guide to the intensity of the knock.

Knock intensity instruments operating on these principles were evaluated by Williams and Dale [58]. The evaluation concluded that the accelerometer instrument is better suited to knock-damage tests, while the microphone system is preferred for octane number assessment or fuel comparisons within a given engine, although no reasons were given for this judgement.

Instruments based on acoustic and accelerometer transducers have to be tuned for each separate engine type tested and give only an indirect indication of what is occurring inside the combustion chamber. It was stated by Klimstra [59], that the amplitude and frequency content of the vibration depends to a large extent on the stiffness of the engine block and on the point of excitation.

These systems can however be an accurate means of determining the onset of knock. In fact, the accelerometer system forms the basis for closed-loop knock control in current engine management systems [60], which are used to avoid knocking conditions.

2.4.2 KNOCK INTENSITY PARAMETERS

This section reviews knock intensity parameters as used by various researchers. Bearing in mind the general approach of avoiding knock completely, many authors chose a parameter to characterise the knock in terms of fuel and engine operating conditions. However, those that have defined knock intensity in some way are reviewed.

2.4.2.1 MAXIMUM PRESSURE AMPLITUDE

A typical engine pressure trace under knocking conditions [41] is shown in figure 6. The curve shows the characteristic pressure oscillation superimposed on the normal cycle. Feeding the signal through a high pass filter (5 kHz) produced the resulting signal shown in figure 7, which represents the pressure oscillations due to knock alone.

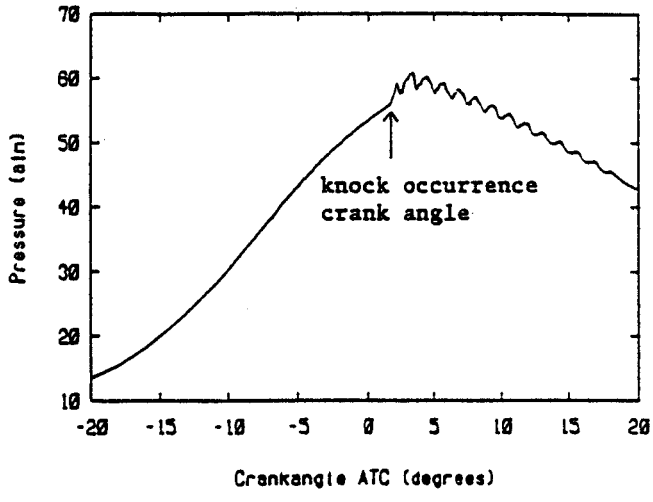

Figure 6: Knocking Pressure Trace [41]

The knock intensity may be defined as either the maximum pressure amplitude or the maximum peak-to-peak values. These intensities will be referred to as the **maximum pressure amplitude.** Many researchers [24,45,61] have expressed the opinion that this signal is directly related to damage, without validating this assumption.

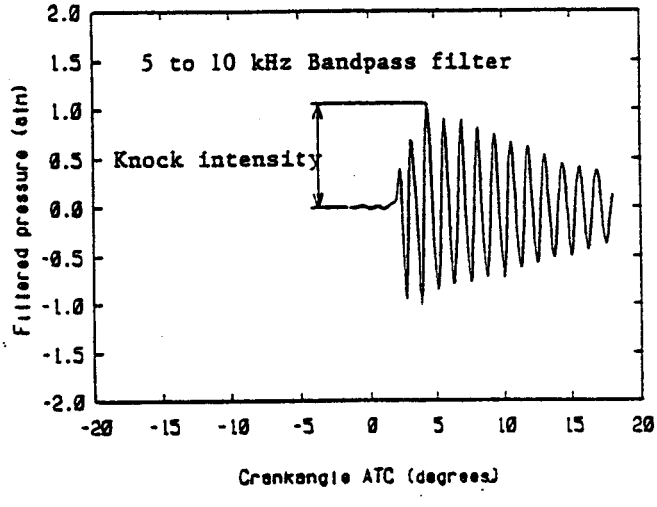

Figure 7: Filtered Pressure Trace [41]

Over the years, other parameters using the mean pressure amplitude have been defined and used. However, Leppard [42] has shown that the mean pressure amplitude, the integral of the pressure oscillations and the integral of the square of the pressure oscillations all cross correlated with statistical significance at the 99.9% level, indicating that these are all similar parameters.

An important point concerning the filtered signals seems to have been overlooked by some

researchers. The high-pass or band-pass filter takes a finite time to open its gate to a high frequency signal [62]. Furthermore, the response of the pressure transducer itself is too slow to track the initial pressure rise, which has been commented on by some authors [29]. In terms of a pressure-history, the auto-ignition is a step-function which causes the subsequent chamber resonance. In this sense, the chamber is a filter with its own time lag. The pressure-history measured is therefore a transmutation of actual events, resulting from the lag of the chamber, transducer and filter. The timescale of the end-gas energy release is of the same order as that of the resonating pressure waves [29], and therefore the pressure attained by the initial impulse should be much greater than that of the resonance. The filtered trace in figure 7 shows that the third oscillation produces the greatest pressure amplitude. This reveals the problems associated with this technique if it is used to describe the initiating impulse within the end-gas zone and as an indicator of the localised erosion damage.

However, the pressure signal does yield a good indication of the global conditions within the combustion chamber, if localised effects are ignored. As discussed previously [13], a knock intensity based on a filtered pressure trace was shown to be a good indicator of global heat flux.

2.4.2.2 AVERAGE MAXIMUM PRESSURE AMPLITUDE

The use of the maximum pressure amplitude as an indication of knock intensity does not account for the cyclic variations in the auto-ignition phenomenon.

Najt [63] showed an improvement in the repeatability of the data when correlating knock intensity against spark advance for a range of reference fuels. In this case his choice of intensity measurement was the maximum pressure amplitude averaged over 4000 consecutive engine cycles. Thus the parameter has the advantage of averaging the cycle-to-cycle variation. It was noted that the mean pressure amplitude included the zero amplitude of the non-knocking cycles.

2.4.2.3 CUMULATIVE PRESSURE AMPLITUDE DISTRIBUTION

Essig [14] used the high pass filtered pressure signal to determine the cumulative pressure amplitude distribution. This method involved the data capture of the digitised signal from a number of cycles. The maximum pressure amplitude was determined for each cycle. A frequency distribution was produced from these data in terms of the percentage exceeding of 5, 10, 15, 20 bar, etc., producing a frequency density of the maximum pressure amplitude.

Essig showed that 10% of the data exceeding 5 bar was equivalent to trace knock as detected by a trained observer. Further spark advance resulted in sustained knock with 100% exceeding 5 bar and over 20% in the region of 10 to 25 bar. This condition could be maintained for short periods, but longer runs under this level of knock resulted in piston crown erosion. Further spark advance resulted in heavy knock characterised by pressure amplitudes of over 50 bar. This condition was found to be unstable resulting in pre-ignition runaway. This is one of the few recorded attempts to relate a knock intensity directly to knock damage.

Betz and Ellerman [13] used a similar method to characterise knock. They combined all the data by defining a knock intensity (*Ki*) as follows:

$$Ki = \sum_{level\,0}^{level\,X} \frac{(p_{max} . n)}{10}$$

where:	values 0 to X	are discrete pressure intervals (eg: 5, 10, 15 bar, etc.),
	p_{max}	is the maximum pressure amplitude per cycle,
	n	is the fraction of occurrences at that pressure.

The absolute value of this knock intensity parameter is dependent on the choice of pressure intervals, although the authors did not comment on this. The authors also claim that this *Ki* is non-dimensional, which is not the case, as it has the units of pressure.

Tests performed on a multi-cylinder engine under heavy knock resulted in one piston being

2.4.2.4 ENGINE OPERATING PARAMETERS

Engine operating parameters have been used as the basis for defining a scale of knock intensity. Parameters such as knock-limited compression ratio (or spark advance, mean effective pressure, etc.) have commonly been used to characterise the onset of knock in terms of operating conditions [3]. When testing under knocking conditions, the operating conditions may still be used as an indication of knock severity in the form of additional increase beyond the point of trace knock. Spark advance is typically used in this manner, with the knock severity being described by the "ignition advance beyond that of trace knock" [47]. This method serves as a simple means of quantifying knock without the use of additional equipment (if trace knock is detected audially).

Exhaust temperature has also been used as indication of knock severity. Exhaust temperatures [45] have been shown to be reduced by as much as 100°C when moving from trace to heavy knocking conditions (by means of reducing fuel octane quality) [44,45,58].

2.4.3 DISCUSSION

In general many researchers seem to have arbitrarily defined a particular knock intensity. With a few exceptions, there was no validation of this choice, although some have inferred an assumption that erosion damage is caused by some form of mechanical impulse.

Most of these criteria are based on the pressure signal. As discussed previously, pressure transducers are able to monitor the oscillating aftermath of auto-ignition, but are not able to register the initial, localised pressure rise of the auto-ignition process itself. This means that any pressure-based criterion will only yield information concerning intensity of chamber resonance and not the intensity of the initial pulse.

It has been implied that the magnitude of the oscillation is directly related to the magnitude of the initial pulse. However, it is both the magnitude and the duration of this pulse that determines the resonating pressure amplitude. The duration is a function of the amount of end-gas involved in the energy release. Whilst, the magnitude of the pressure pulse is something of an unknown quantity and appears to be dependent on several factors, including

the geometry of the end-gas region. It follows that it is not possible to separate both the initial pressure rise and quantity of the end-gas from the magnitude of the resulting pressure oscillation. Until the development of transducers and filters with quicker response times, the initial pressure rise will remain an unknown quantity.

The localised erosion damage is expected to be more sensitive to the magnitude of the initial pressure pulse, than to the duration. Therefore, it is deduced that knock intensities based on the amplitude of the global pressure resonance will not correlate with the extent of erosion damage.

In summary, since erosion damage is a localised effect in the end-gas region, it follows that the damage will not correlate with a global, pressure-based knock intensity criterion. Alternately, increased heat flux, which results from chamber resonance, does correlate with well with pressure-based knock criteria. Damage arising from increased heat flux is expected to correlate in a similar manner. This provided a useful test for the damage investigation on which this thesis is based.

3.1 OBSERVATIONS

Although the engine types and operating conditions were quite varied, inspection of the specimens showed that 3 principal categories of damage prevailed. The specimens discussed below are typical of the 22 useful samples collected and in some cases are similar to those photographs presented by other authors. The information sheets for each of the samples discussed are contained in Appendix A.

3.1.1 EROSION DAMAGE EVIDENCE

All the specimens exhibited some evidence of erosion damage on the piston top-land and on the edge of the land and crown. In the cases where erosion was observed on the crown, it was only found where the clearance between head and piston was small (at the edge of the piston). Except in cases where the spark-plug was exactly centrally located (some 2-stroke engines), the erosion was found to be concentrated in one area of the specimen. The extent of the erosion varied from a cleaning of deposits and surface "polishing" to progressive amounts of erosion of piston material. The eroded surface always showed the typical "cavitation-type" pitting.

Specimen #1 (figure 8) shows an example of deposit cleaning. The operator reported that the engine had been knocking for some time prior to the failure. This piston was removed due to oil ring failure which had caused a carbon deposit of over 1.5 mm thick on the crown. As seen on this specimen, a crescent shaped area had been completely cleaned. Since this cleaned surface was the area furthest from the spark plug and was situated beneath the inlet valve, which is typically a very cool region in the combustion chamber [19], it was unlikely that this deposit removal could have been

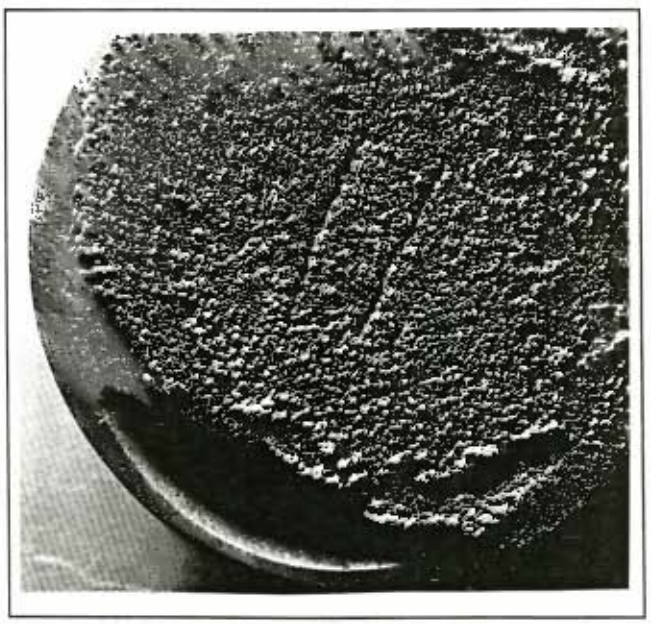

Figure 8: Specimen #1

caused by local overheating or surface-ignition. The top-land region within this crescent showed a polished surface while the rest of the top-land had a dark deposit. The crescent shape of the cleaned zone corresponded to the likely site of the end-gas at the point of auto-ignition. Although this piston had not been damaged by knock, the localised effect of incipient erosion was clearly evident.

Figure 9 (specimen #2) shows a 2-stroke piston which was removed after knocking combustion had been noticed. Significant knock erosion was seen on the top-land, with lesser damage at the outer edge of the crown. The spark-plug is centrally located in this engine which would result in a near annular end-gas region adjacent to the cylinder (at the onset of knock). Erosion damage could be seen all around the edge of the piston, but was particularly severe around the exhaust port (local hot zone).

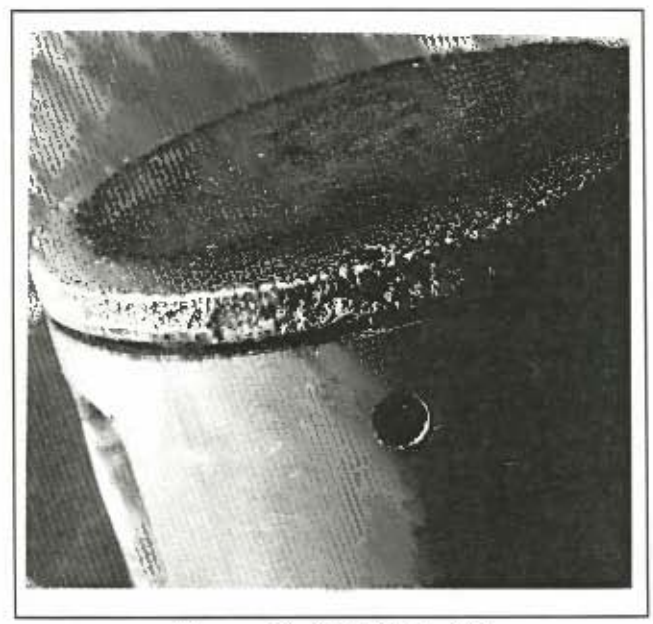

Figure 9: Specimen #2

The piston shown in figure 10 (specimen #3), had been inadvertently used with low octane fuel over a long distance, resulting in a partial seizure, as seen by the scuffing on the skirt. A large amount of material had been eroded along the top-land in the end-gas region. There were no other signs of erosion on the piston, other than that visible in this figure. This is an indication of the localised nature of knock erosion, with the erosion zone adjacent to the expected position of the end-gas region.

Figure 10: Specimen #3

Of particular interest are the cavities above and below the first compression ring. Close examination of the piston revealed that a passage had been eroded around the back of the top ring. Similar eroded cavities around the rings were also observed in other specimens. The previous 3 specimens are typical examples of knock-related damage reported in literature [3,4,12,13,14].

Figure 11 (specimen #4) shows a piston which was removed after the engine experienced excessive blow-by and power loss. In this case, the knock erosion had formed a passageway around the rings through which blow-by had occurred. The surfaces of the passage had been burned to a smooth finish exhibiting a molten surface, but knock erosion was still clearly visible in the small cavities above the first and second rings and at the edges of the blow-by channel. Also of note was that the ring gap happened to coincide with the centre of the blow-by channel. This could only aggravate the amount of blow-by that occurred. In fact, it is possible that the coincidence of the ring gap with the end-gas region (forming an extended cavity) could have contributed to the deep erosion into the second-land.

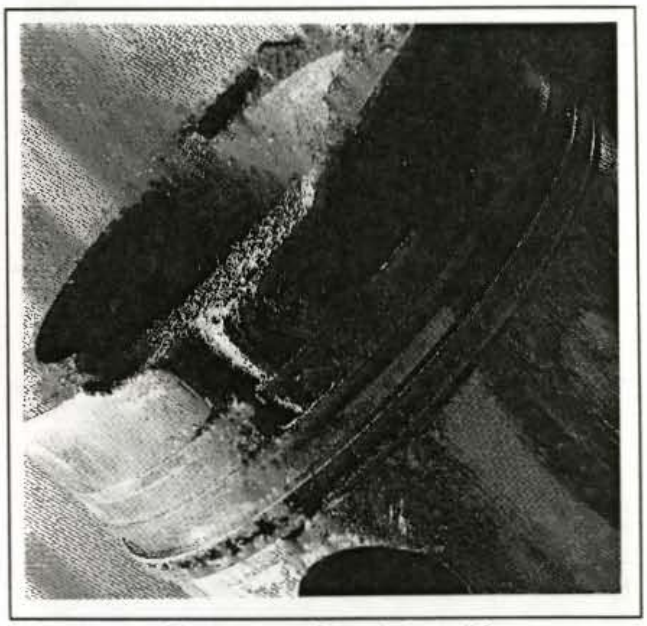

Figure 11: Specimen #4

Another piston with a similar history is shown in figure 12 (specimen #5), but in this case the vehicle was driven a considerable distance after the initial blow-by. It may be seen that, the blow-by had considerably enlarged the passage from combustion chamber to sump, but again erosion damage is still visible in what remains of the ring grooves and again at the edges of the blow-by channel.

In some instances, erosion damage was also observed on cylinder heads and, as in the case of the piston specimens already discussed, the damage was confined to localised regions. These eroded zones were always found at the edge of the cylinder, above the position of the

corresponding piston erosion. In all these cases, the erosion zone appeared in the squish region where piston-head clearances were small. Figure 13 shows an example of this type of damage. The erosion is seen to occur at the edge of the cylinder and has begun to undercut the head gasket. This head has a small ridge, 3mm inside the edge of the cylinder, and it is interesting to note that this has also been slightly undercut. This head was from the same cylinder as piston specimen #6 (figure 14) which will be discussed in detail in the following sections.

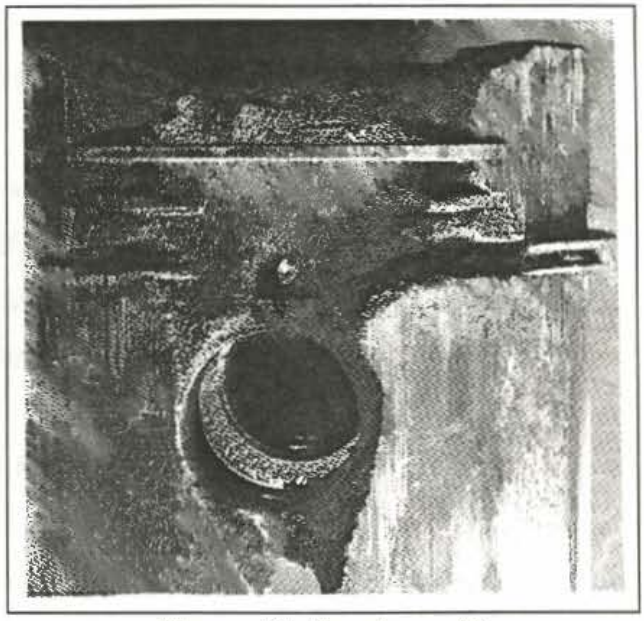

Figure 12: Specimen #5

Although there was no sign of damage on the head gasket in this case, other examples showed gasket erosion. Other researchers [14,45,46] have also reported gasket erosion as a result of knocking combustion.

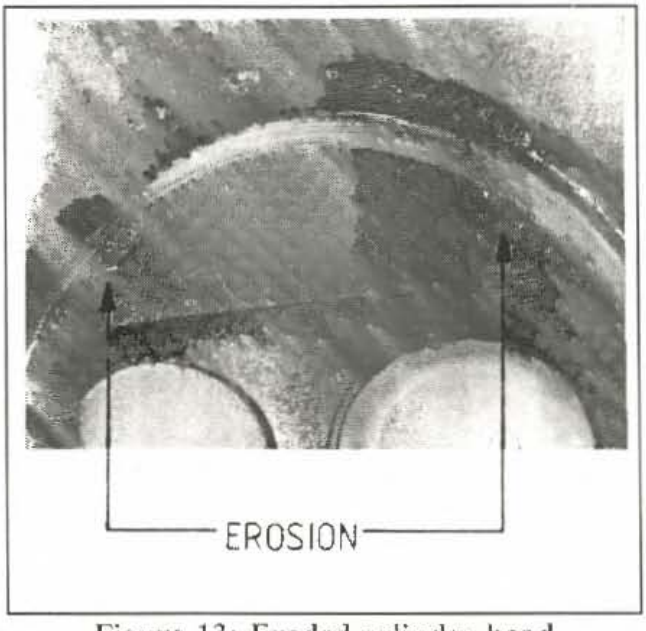

Figure 13: Eroded cylinder head

A final observation concerning erosion damage is that aluminium is preferentially attacked. In the case of rings, bores and cast iron heads, erosion damage was only observed in one instance. In this case, the cast iron head of a Ricardo E6 research engine was found to be lightly eroded next to the head gasket, and this was after operating for approximately 50 hours under heavy knocking conditions.

Sections of eroded piston surfaces were photographed at high magnifications for comparison to subsequent tests specimens, and will be discussed in the appropriate section.

bore seizure was in the upper cylinder region, indicating that the rings themselves had begun to seize. The compression rings were not broken, but they were jammed in their ring grooves (the top ring being the most firmly bound). On removing the rings (without breaking them) and fitting them into the lower, unworn end of the bore, the top ring was found to have a ring gap much greater than the specification. Figure 15 shows this ring fitted into the bottom of the cylinder bore. The second ring gap was also oversize by nearly 1 mm. No damage was visible at the ends of the rings. The ring gaps for the remaining, undamaged pistons were found to be within engine specifications. The significance of this example is discussed in section 3.2.3.

The damage symptoms of the remaining 16 useful piston specimens are summarised in the table below, which is presented for completion. The table indicates the number of pistons exhibiting a particular damage symptom.

DAMAGE SYMPTOM	NUMBER OF PISTONS
Erosion	16
Blow-by channel	8
Piston-lands cracked or fractured	3
Rings jammed in ring-grooves	13
Rings fractured	6
Piston seizure or scuffed piston skirt	9

3.2 DISCUSSION OF DAMAGE SURVEY

Having documented the characteristics of knock damage, as illustrated by the specimen collection, this section synthesises the observations with the current knowledge-base in order gain understanding of the mechanisms of knock damage. Each of the three main types of damage will be reviewed.

3.2.1 EROSION DAMAGE MECHANISM

Erosion was always found in localised regions at the outer extremities of the combustion chamber. This pointed to the end-gas energy release being responsible for the damage, since these regions appear to be adjacent to the expected end-gas location. This is supported by the current understanding of the knock mechanism [31,46] where auto-ignition can lead to "developing detonation" which is driven by the energy release of unburned mixture in the end-gas. It is this process that causes the local walls to be exposed to excessive pressure and thermal stresses. It is to be expected that when the shock wave moves into the burned-gas region, where no significant chemical energy release is possible, the wave intensities would diminish and the probability of erosion would be correspondingly reduced.

The most common observation concerning knock-induced erosion is that it occurs mainly in crevices, such as the top-land between the piston and bore. In all cases, it was observed that erosion damage on the piston top-land was far more extensive than on the piston crown. This is seen on specimens #2 to #6. The heavier erosion on the top-land compared to the crown could be explained by two independent characteristics of knock:

- Knocking combustion is able to penetrate into the top-land crevice, which under normal combustion conditions causes the flame to be quenched [66]. This means that at the point of auto-ignition, the top-land crevice volume is available for energy release (whereas it is not penetrated by the normal deflagration flame).
- The geometric confinement of the crevice volume ensures that the shock waves undergo multiple reflections compared to the relatively unconstrained end-gas in the combustion chamber itself [32,33,34].

The surfaces were rarely eroded by more than a millimetre in depth, except where a blow-by channel had been produced. The region of erosion damage tended to spread around the top-land as the general severity of damage increased. This seems to indicate that erosion into the material was self-limiting. Comparing the lightly eroded specimens to those more severe damaged, it would appear that erosion generally spreads around the top-land and down towards the rings as illustrated in figures 16(A) and 16(B) and also shown on specimen #6 (figure 14). This broad "V"-shaped erosion pattern was seen on other specimens and has

been reported previously [14].

The two facts, that the erosion is never deep and that it only occurs on the crown when head clearances are small, indicates a likelihood that critical crevice dimensions are necessary for erosion to take place. It was inferred that once these dimensions are exceeded, erosion no longer occurs. The erosion mechanism is seen to operate at the interface between a tightly constrained crevice and the neighbouring less bounded region. The detonation chamber tests of Maly et al [34] confirm this hypothesis.

In the case of 2-stroke pistons, it was observed that although erosion was found all around the circumference of the piston, damage was particularly severe in the region adjacent to the exhaust port (which operates at significantly higher temperatures). This could be explained by the weakening of the material at elevated temperatures.

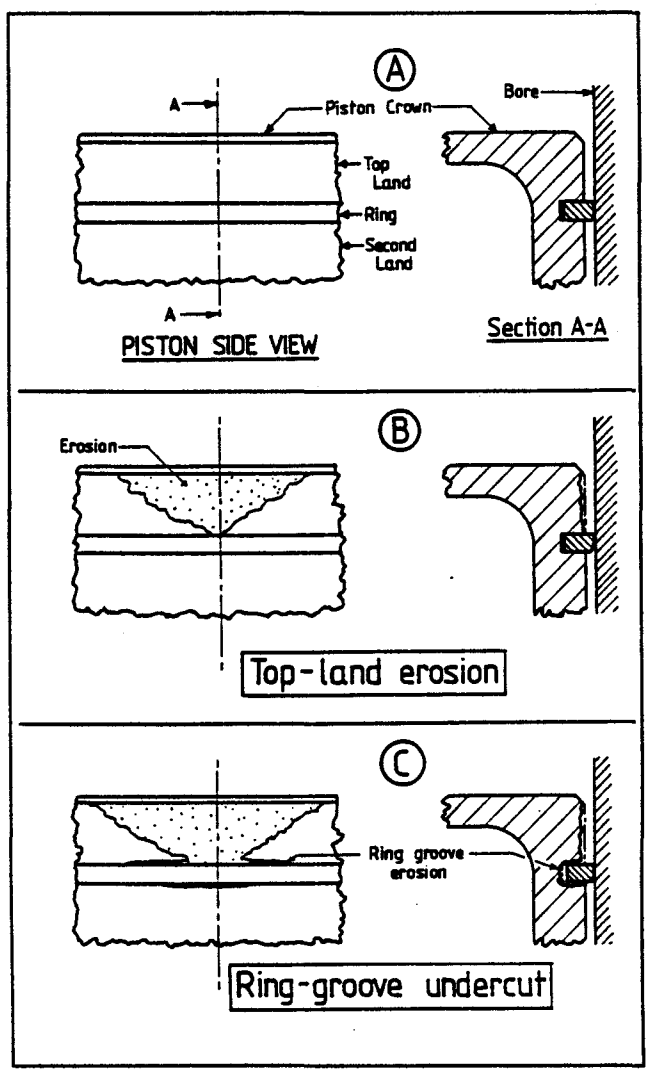

Figure 16: Progressive erosion damage

From the observations on the more severely damaged specimens, it appears that continuous operation under knocking conditions causes the erosion to spread downwards into the ring grooves (the rings being resistant to erosion). This forms a cavity around the first ring as illustrated in figure 16(C) and seen on specimen #3 (figure 10). By this stage, a blow-by path has been produced around the first compression ring. With further operation, hot combustion gases are forced through this cavity, burning the material and widening the blow-by path as illustrated in figure 17 and seen on specimen #4 (figure 11). In these cases, the channel surfaces were burned smooth and did not exhibit the typical pitted, erosion surface. The high temperature blow-by was thought to be responsible for obliterating the erosion

surface by further material removal. Continued operation would ultimately produce the result illustrated in figure 18 and seen on specimen #5 (figure 12). At this stage, the ring support has been removed and therefore ring fracture would be anticipated, as seen in specimens #4 and #5.

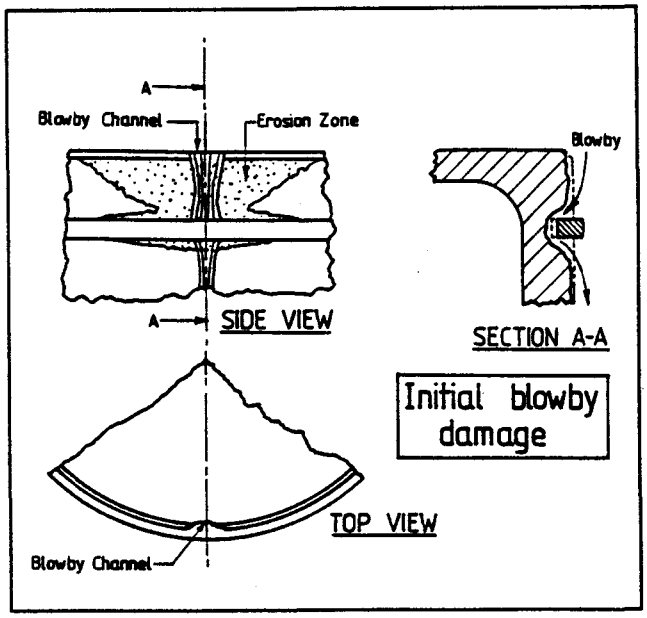

Figure 17: Initial blow-by damage

As discussed previously (section 3.1.1), pistons were not the only surfaces eroded by knock. Erosion also occurred on the head and head gasket which would eventually lead to coolant loss and blow-by into oil or water channels.

Pre-ignition at the burned piston surfaces could also arise, leading to runaway engine failure.

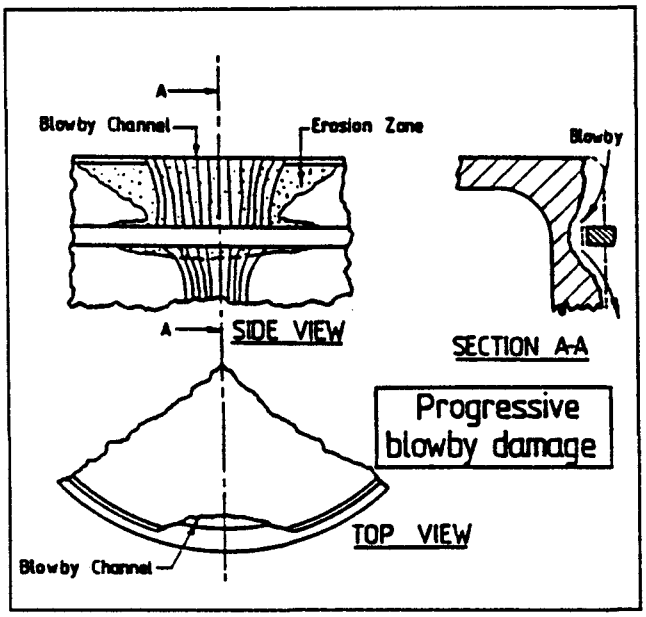

Figure 18: Progressive blow-by damage

The deductions made in this section stem from the events that follow from continuous knocking. The relationship between the intensity of knock and the level of damage cannot be ascertained. This is addressed with experimental and theoretical work in chapter 4.

3.2.2 PISTON SEIZURE MECHANISM

In cases exhibiting piston seizure against the bore, the seizure was attributed to excessive thermal expansion of the piston, due to increased heat flux.

The source of this heat flux, under knocking conditions, is found in the resonating pressure waves which disturb the thermal boundary layer. A further increase in heat flux may be caused by a blow-by path around the rings, due to piston erosion, land fracture, or ring fracture.

Finally, at the onset of piston seizure, the heat flux generated by the additional friction would complete the seizure process.

3.2.3 PISTON RING AND LAND FAILURE MECHANISMS

From the literature review, only one theory has been proposed to explain the occurrence of rings jammed in their grooves. Ricardo [22] suspected that the presence of free-carbon particles or erosion debris was the cause of this knock related feature. However, no sign of debris or carbon deposits was found in any of the specimens that were examined. Therefore, another mechanism was assumed to be responsible for this. The only possible explanations for jammed rings was that either the grooves had shrunk, or the rings had grown to cause an interference fit.

Cases of cracked or fractured piston lands were only found where the rings were jammed in their grooves. This seemed to indicate that these two phenomena were related.

No further explanations concerning these types of knock damage could be made from the specimen collection. A more detailed investigation is presented in chapter 5.

To summarise, it was apparent that two independent aspects of knock are responsible for the various forms of damage:

(1) Localised pressure-temperature transients causing localised erosion damage.
(2) Elevated heat flux causing global piston and ring problems.

As a result, the research effort diverged at this point into two investigations. Chapter 4 deals with the localised erosion damage, while chapter 5 covers the quantification of the global heat flux damage mechanisms.

CHAPTER 4

EROSION INVESTIGATION

This chapter concerns a study of the mechanisms by which knocking combustion causes erosion damage. This work was aimed at establishing a foundation for quantifying knock intensity in terms of its propensity to cause erosion damage.

The investigation was divided into the following components:

1) A computer model was used to estimate the shock wave conditions in the end-gas after the auto-ignition process. The model used the initial conditions in the end-gas (prior to knock) to calculate the characteristics of a detonation wave. The results of these simulations were used to examine how engine conditions and fuel composition affect the damage potential of the knock. From this analysis, a parameter was identified which could be used as a measure of erosion-damage intensity.

2) An analysis was performed to calculate the thermal stresses in the walls of the combustion chamber and piston. This model was used to investigate the contribution of thermal stresses to the knock-induced erosion process. A comparison of thermal stresses between knocking and non-knocking conditions was made using measured surface temperatures.

3) Detonation chamber tests were performed to study the effects of operating conditions on erosion damage, under controlled conditions, and to provide validation for the detonation model.

4) An engine was modified to accommodate an aluminium specimen which would be preferentially eroded under knocking conditions. The effects of fuel and operating conditions on erosion damage were investigated. The results of these tests were used as a means of validating the predictions of the theoretical analysis and to confirm the identification of the proposed knock intensity criterion.

4.1 DETONATION MODEL

It was the intention of the present research to quantify the knock intensity in terms of its potential to cause erosion damage. Therefore, of primary interest was the effect of the initial end-gas composition and conditions on the ensuing wall loading.

A computer model simulating a fully-developed Chapman-Jouguet detonation wave was developed which calculated the post-detonation conditions as a function of end-gas pressure, temperature and composition prior to knock. Although it is unlikely that the detonation which occurs in the end-gas is fully developed, it was thought that the model would provide useful information concerning relative effects of initial conditions. The fact that damage was thought to be caused by the superposition of these waves in no way detracts from investigating the characteristics of the shock itself, as any change in the wave condition would be reflected in the superpositional conditions as well.

The details of the detonation calculations and the computer code are presented in appendices B and I respectively. The model calculated the strong detonation conditions at the Chapman-Jouguet point based on continuity, conservation of both momentum and energy, and assuming ideal gas relationships. Specific heats for the main species present were determined as a function of temperature. The dissociation of water and carbon dioxide was also accounted for. The detonation condition was solved by means of a Newton-Raphson iteration of the post-detonation temperature. The initial conditions which could be controlled were as follows:

INPUT: **End-gas conditions prior to knock:**

- pressure
- temperature
- fuel type
- fuel-air equivalence ratio

The program was used to calculate the corresponding Chapman-Jouguet detonation wave condition, which was described by the following parameters:

OUTPUT: **Detonation conditions:**

- stagnation pressure
- temperature
- wave velocity
- gas velocity

The stagnation pressure was used to describe the impulse intensity of the wave, in terms of the static pressure together with the gas momentum. Throughout this work, unless otherwise stated, the term "detonation" pressure will refer to the stagnation pressure of the wave.

Octane, methanol and ethanol were modelled to evaluate the effect of diverse fuel composition. The model was also used to simulate the detonation of ethylene-oxygen mixtures, in order to test the accuracy of the model against experimental data and to explain the findings of erosion experiments using a detonation chamber.

4.1.1 ETHYLENE-OXYGEN DETONATION SIMULATIONS

Lewis and Von Elbe [67] presented data taken from three separate sources [68,69,70], each reporting measured detonation velocities for ethylene-oxygen mixtures. Figure 19 shows the fit of these data to the theoretical model which was run with the identical initial conditions as the experimental data. A relatively close correlation between the modelled and experimental data is seen, which served to confirm the general accuracy of the model. No reported data concerning octane could be found. However, as the model was to be used to investigate the trend of initial conditions on detonation characteristics, it was sufficient to validate the model using ethylene-oxygen data.

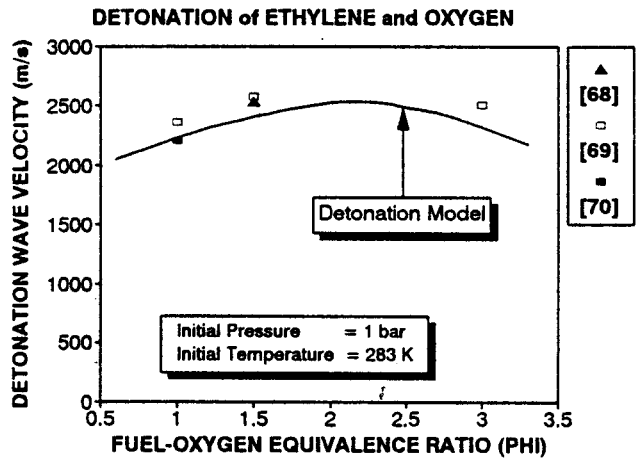

Figure 19: Theoretical and measured detonation velocities

A further validation was performed using experimental data from detonation chamber tests, detailed in Appendix D. Figure 20 shows the theoretical and measured detonation pressures over a range of ethylene-oxygen mixture strengths. It is seen that the experimental data systematically falls below the predicted values. The data follows a similar trend to the theoretical predictions, as illustrated by the least squares polynomial curve fit. The slopes of these two curves can be seen to be almost identical, indicating that the model accurately predicts the effect of changes in initial conditions on detonation pressure.

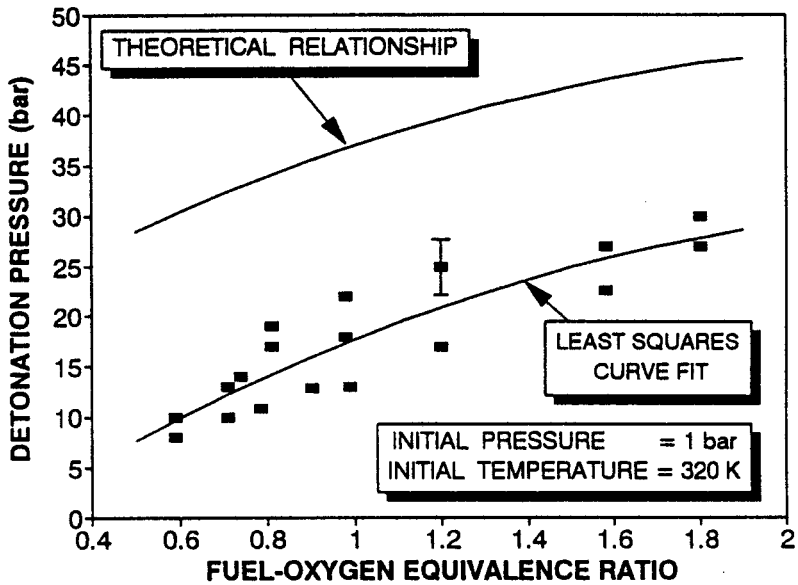

Figure 20: Theoretical and measured detonation pressure

The reasons for the close correlation of the detonation velocity data (with respect to the model) in comparison to systematic underestimate of the pressure measurements could be explained by the assumptions implicit in the model and the measuring techniques used in the experimentation. In the model, the detonation wave was assumed to be a discontinuity with no cognisance taken of reaction rates. Glassman [71] has discussed the accuracy of these types of models in relation to experimental data. He stated that the assumptions adopted are valid for the determination of the wave velocity as the equations place no restriction on the distance between the shock wave and the seat of the generating force. However, the peak pressure is a function of the structure of the wave, which comprises of a shock front followed by an induction and reaction zone. The Chapman-Jouguet conditions make no allowances for the wave structure, and therefore some discrepancy between calculated and measured pressures should be expected. Furthermore, the pressure transducer has a limited response

The lower measured pressure values are due to the integration effect induced by the finite sensitive surface of the transducer. Since the pressure wave is thin and will never hit the surface exactly normal, the transducer will indicate only an area averaged mean value, which would be composed of the real peak pressure times the actual loaded area plus a "no-pressure" times the remaining area, divided by the total transducer area. Notwithstanding these deficiencies, the measured pressure clearly follows the predicted trend, though at systematically lower values.

The direct stresses on the walls of the end-gas region in a knocking engine are caused by the reflection of the detonation waves. These results show that the model is capable of accurately simulating the effect of change in initial conditions on the detonation pressure, though it cannot predict the absolute values with accuracy. For this investigation, the effect of change in initial conditions was of interest and thus this model was considered adequate for the purpose.

4.1.2 EFFECT OF FUEL TYPE AND MIXTURE STRENGTH ON DETONATION

Simulations were performed over a range of typical engine end-gas conditions using the fuels previously mentioned. The full scope of these simulations may be found in Appendix B, while only the most relevant points are discussed here.

Figure 21 shows the effect of mixture strength on detonation pressure for 3 different fuels (the other detonation conditions such as temperature and velocities from these simulations are presented in appendix B). The initial conditions were the same for each fuel. The short carbon-chain alcohol fuels are seen to have greater detonation pressures than the long chain octane. This is primarily due to the increased energy density of the short carbon chain mixtures, relative to the longer chain fuel mixtures.

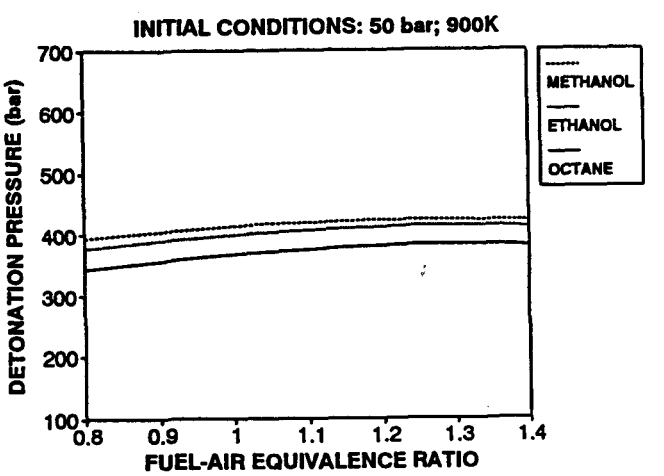

Figure 21: Detonation pressure vs equivalence ratio

It is also seen that over the equivalence ratio range of an engine (typically between 0.9 and 1.2), the detonation intensity will increase slightly with mixture strength.

The magnitude of the pressure is seen to be considerably higher than that for the detonation chamber simulation (figure 20), because the initial pressure is 50 bar compared to the detonation chamber value of 1 bar.

4.1.3 EFFECT OF INITIAL PRESSURE AND TEMPERATURE ON DETONATION

Figures 22 and 23 show the effect of initial temperature and pressure on detonation pressure. Increasing initial pressure is seen to have a near proportional effect on the detonation pressure. Conversely, increasing initial temperature is seen to cause a reduction in detonation pressure. The effects of temperature and pressure on detonation intensity are primarily due to their influence on the initial gas density. Both figures indicate that the mixture strength has a negligible effect on the detonation intensity.

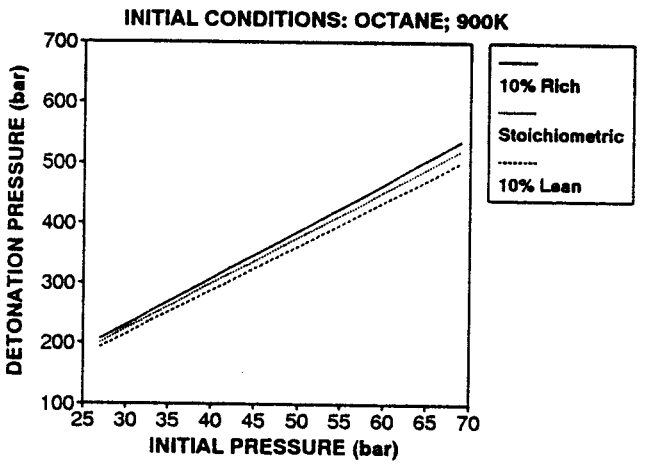

Figure 22: Detonation pressure vs initial pressure

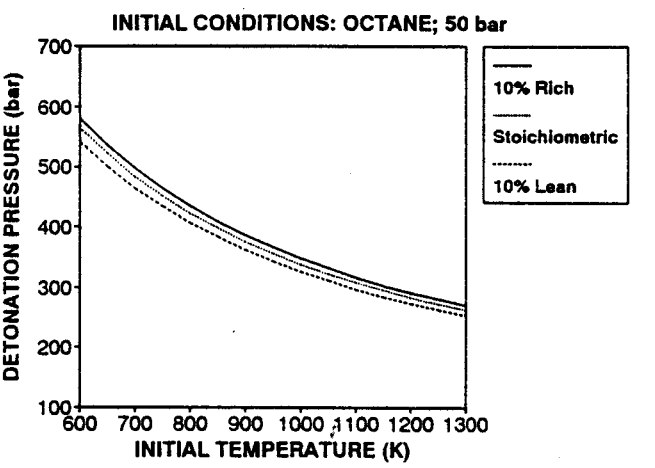

Figure 23: Detonation pressure vs initial temperature

Although auto-ignition temperatures are typically 1000K, the "developing detonation" wave has been shown to be capable of entering the crevices such as the region between the piston top-land and bore [66], where temperatures of the order of 600K may be expected. The

inverse relationship between detonation pressure and initial temperature illustrated in figure 23 suggests that the detonation pressure could be considerably higher in such crevice regions compared to the main chamber. This observation adds an independent explanation, besides the effects of geometric confinement, as to why the piston top land is preferentially eroded.

4.1.4 SENSITIVITY ANALYSIS OF INITIAL CONDITIONS

Erosion damage was considered to be caused by a combination of the pressure pulse, producing direct contact stresses in the walls, and the thermal stresses induced by the transient heat flux which is primarily influenced by the wave temperature.

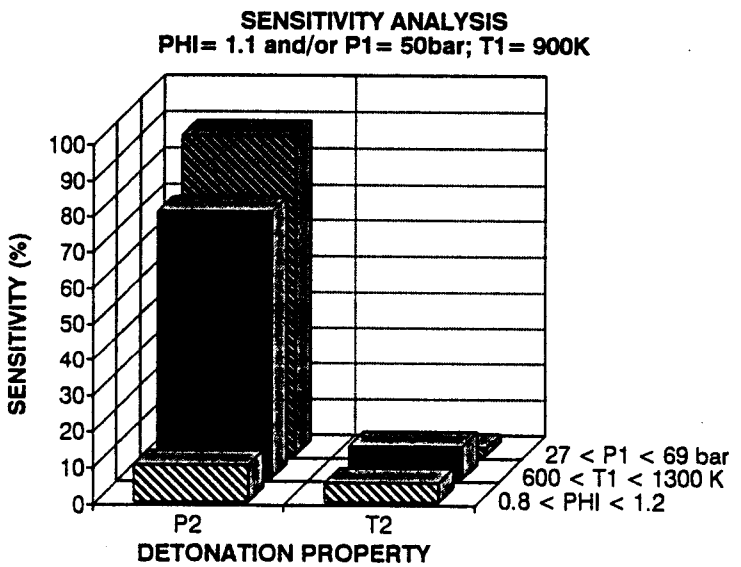

Figure 24: Sensitivity analysis

In an attempt to resolve the dominance of these two effects, an analysis was performed to compare the sensitivity of detonation pressure and detonation temperature to changes in initial conditions, as detailed in appendix B. The results, presented in figure 24, show again that the detonation pressure is very sensitive to initial temperatures and pressures, but relatively insensitive to mixture strength. By comparison, it is seen that the detonation temperature is extremely insensitive to the initial conditions. This observation provided a basis for testing whether erosion damage was caused mainly by the pressure wave, or the temperature shock, as described in section 4.3.

4.1.5 EFFECT OF ENGINE OPERATING CONDITIONS ON DETONATION

Using the insight gained from the detonation model, it was possible to predict the effect of some engine operating conditions on detonation pressure.

COMPRESSION RATIO, SPARK-TIMING AND FUEL TYPE

From the simulations, it was apparent that initial temperatures and pressures have significant, but opposite effects on the detonation intensity. Therefore, it was instructive to determine which of these effects was more dominant, under conditions of polytropic compression. For comparative conditions, it was assumed that knock occurs at approximately the same position in the cycle. The detonation intensity was thus determined by the extent of the end-gas compression prior to auto-ignition.

The model was run using initial conditions determined by a polytropic compression using typical engine conditions at inlet valve closure, as detailed in Appendix B. Both methanol and octane detonations were simulated over a range of engine compression ratios.

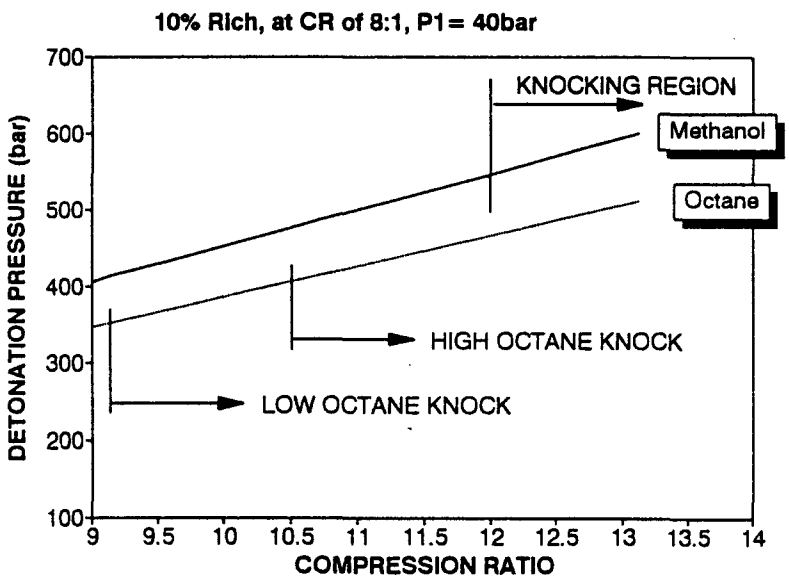

Figure 25: Detonation pressure vs compression ratio

Figure 25 shows the results of this simulation. The temperature of the methanol mixture at inlet was chosen to be 22°C lower than that of octane, as reported by Moran and Yates [72].

All other initial conditions were equivalent for both fuels.

From the graph, it is seen that the detonation pressure increases with increased compression ratio. This indicates that, with polytropic compression, the initial pressure at the point of auto-ignition dominates the detonation characteristics. This argument also applies to the effect of spark advance which causes a similar increase in polytropic compression of the end-gas. In general, engines are optimised by choosing their compression ratio and ignition-timing to correspond to a fuel of particular knock resistance. Engines running on higher octane fuels would be optimised for a higher compression ratio and/or spark-advance. Therefore, it was deduced that chemically similar fuels which have increased knock resistance (by means of anti-knock additives) would produce more intense detonation characteristics, assuming both are operating in engines optimised for their use.

Methanol was shown to produce significantly higher detonation pressures compared to octane, at equivalent operating conditions (see figure 21). In an engine, this difference is exacerbated by the greater evaporative cooling of the fuel, which has the combined effect of reducing end-gas temperatures and increasing the knock resistance. The reduced initial temperature would, in itself, cause higher detonation pressures, while the greater knock resistance means that the optimised engine would be running at higher compression ratios than a gasoline fuelled engine. Therefore, methanol should exhibit much greater detonation intensities than gasoline under engine knocking conditions, as shown in figure 25.

INLET TEMPERATURE

The effect of engine inlet temperature on detonation intensity cannot be assessed directly from the model. With increased inlet temperature (and all else unchanged) knock would occur earlier in the cycle (provided knock occurs after TDC). This means that both the initial temperature and pressure prior to knock would increase with increased inlet temperature. As these two parameters have opposite effects on detonation intensity, it is not possible to predict which would be dominant without knowledge of their functional relationship.

ENGINE SPEED

The effect of engine speed on detonation intensity is also an interesting area of study. In order to predict this effect it is necessary to know the relationship between the end-gas temperature and pressure as a function of engine speed. It has been shown that the mixture temperature at inlet valve closure increases with engine speed, due to reduced evaporative cooling of the fuel and increased inlet pumping losses [72]. This would cause the end-gas temperatures to increase with engine speed. However, the pressure of the end-gas as a function of engine speed is determined by the breathing characteristics of the particular engine.

For a speed range in which pressures are reduced with increased speed, it is expected that the detonation intensity will also reduce with engine speed. This prediction is based on the fact that with increased speed, the pressures are reduced and the temperatures increased, both parameters causing a reduction in detonation pressures.

In the case of a speed range in which the pressures at the onset of knock are increased with engine speed, no clear prediction can be made. This would provide an interesting area of study.

4.1.6 PROPOSED KNOCK INTENSITY-EROSION CRITERION

The theoretical study has demonstrated a strong influence of the initial temperatures and pressures on the pressure of the detonation wave. If the detonation wave pressure is largely responsible for the localised erosion damage, then the initial conditions prior to knock could be used to quantify the potential of knock to cause erosion damage.

In many cases (as discussed in the previous section), the initial pressure is the dominant factor controlling the detonation intensity. Therefore, it is proposed that the cylinder pressure just prior to knock be investigated as one possible indicator of erosion damage potential.

An advantage of this parameter is that, unlike the conventional knock intensity criteria (discussed in chapter 2), the measurement of cylinder pressure prior to knock is not confounded by high frequency sampling problems and system response limitations, and is therefore much easier to measure accurately. Furthermore, the measured cylinder pressure reflects conditions in the end-gas region, irrespective of the position of the pressure transducer, whereas, the conventional knock intensity measurements (like mean pressure amplitude) rely on the transducer being situated in the end-gas region (which is not always the case).

4.2 THERMAL STRESS ANALYSIS

As discussed in the previous section, erosion damage was considered to be caused by a combination of the pressure pulse, producing direct contact stresses in the walls, and also the thermal stresses induced by the transient heat flux. The transient heat flux in the crevice region is primarily a function of post-detonation temperatures (pressure and velocity being second-order effects). The sensitivity analysis of the detonation model indicated that the detonation temperature is very insensitive to initial conditions and thus it is expected that the local heat flux around the erosion regions would be relatively unaffected by changes in the initial conditions prior to knock (compared to their effect on detonation pressure). However, this does not imply that the thermal stresses are negligible, only that the they are relatively unchanged over the operating conditions analyzed. To study all the possible mechanisms of the erosion damage it was therefore necessary to evaluate the extent of the thermal stresses induced in the walls.

A detailed thermal stress analysis was undertaken to predict wall stresses under both knocking and non-knocking conditions. Maly et al [34] used a thermal contact model which estimated the thermal stresses to be between 4 MPa and 20 MPa, under knocking conditions. These stresses amounted to about half the values of the direct stresses estimated by the authors. However, their calculations made no allowances for material constraint and was not able to differentiate between compressive and tensile stresses induced.

The details of the thermal stress model are presented in Appendix C. A transient-conduction heat transfer model was used to calculate the temperature profile across the wall of the combustion chamber (or piston). From the literature [19], experimentally measured surface temperatures, based on film thermocouples, were used as input to calculate the temperature profile under knocking and non-knocking conditions. The temperature data were taken from thermocouples placed in the end-gas region and therefore reflected the localised effects of the knock phenomenon.

The stresses caused by thermal expansion were calculated from these temperature profiles using the Timoshenko equations for non-symmetrical temperature distributions [73]. The stresses determined in this manner result from the differential thermal expansion of the wall

material due to the temperature gradient. The model was able to calculate the stress as a function of depth into the wall for various overall wall thicknesses.

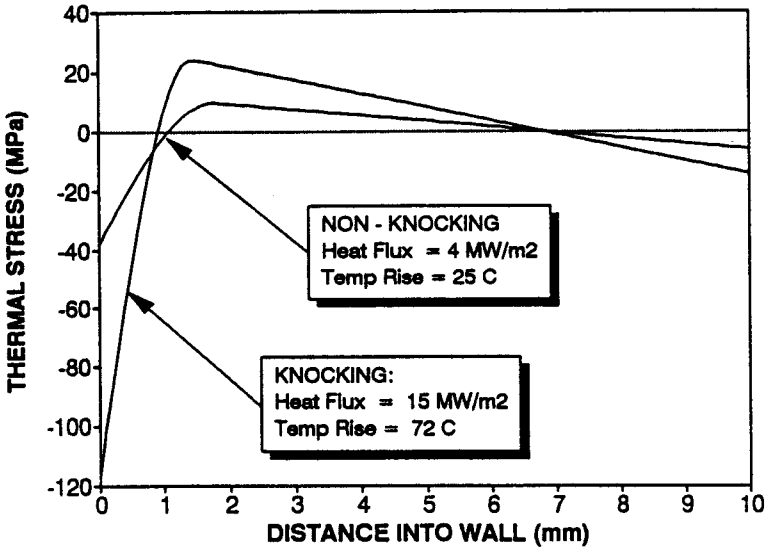

Figure 26: Comparative thermal stresses in a 10 mm wall

Figure 26 shows the resulting thermal stress distribution under knocking and non-knocking conditions for a wall thickness of 10 mm. Referring to the stresses under knocking conditions, the higher temperature at the outer surface (0 mm) produces extreme compressive stresses within the first 1 mm of the surface. Due to the compression in the skin, the central portion is placed in tension and the bending moment around the central zone causes the cooler outer surface to be in compression. The magnitudes of these stresses are considerably higher than reported by Maly et al [34]. With this more detailed analysis using experimentally-derived surface temperatures, the skin compressive stress was found to be nearly 70% of typical proof stresses (for piston alloys). These stresses are of similar magnitude to those produced by the pressure of the reflected detonation wave. The tensile stress below the surface could aggravate the Hertzian stresses produced by the shock wave pressures. However this is dependent on the relative strain rate and heat transfer rate. It is more probable that the thermal stresses would manifest themselves after the occurrence of the pressure induced stresses.

Figure 26 also reveals that, in comparison with normal operating conditions, the compressive thermal stresses are over 3 times greater for knocking combustion, while the tensile stresses

are more than double. Due to the thinner thermal boundary layer in the case of knock, the peak tensile stresses are closer to the surface than for normal operating conditions, which further aggravates the skin loading.

The wall thickness is a variable which affects the stress magnitude and distribution, and this was investigated in Appendix C. It was found that the compressive stress on the high temperature surface increased with greater wall thickness. It was also found that increased wall thickness would result in reduced tensile stresses, but elevated compressive stresses on the low temperature surface.

In performing these calculations, certain assumptions had to be made concerning the temperatures occurring on the inside (cold) wall. It was verified that the assumptions would cause the thermal stresses to be underestimated, and so this model could be considered to be conservative in its predictions. The details are presented in appendix C.

Clearly the thermal stresses caused by knocking combustion play a significant role in the surface destruction. However, from the detonation wave model, it was deduced that these stresses would be relatively unchanged over typical engine knocking conditions. It remained to be investigated whether the erosion damage rate was significantly influenced by changes in operating conditions, in order to ascertain the relative importance of the detonation pressure stress versus the thermal stress.

4.3 DETONATION CHAMBER EXPERIMENTS

Knock is a stochastic phenomenon and as such it is very difficult to produce controlled conditions using engine tests. The detonation chamber gives the researcher a controlled and repeatable tool to simulate conditions in the crevice regions of a knocking engine. The detonation experiments reported were aimed at the following objectives:

- providing experimental validation for the detonation model, in terms of predicting the characteristics of detonation waves based on the initial conditions, and;
- investigating the effect of operating variables on the amount of erosion damage induced by detonation waves.

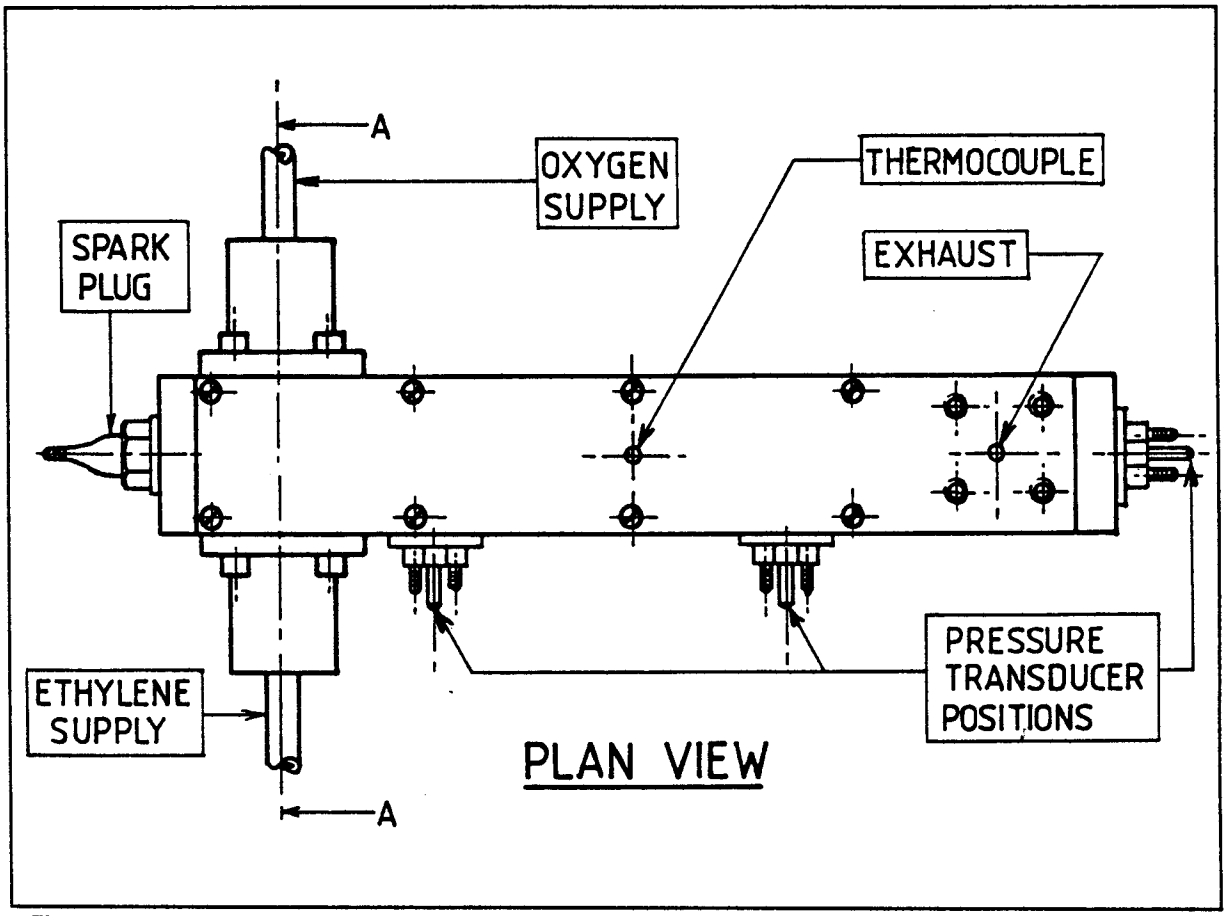

Figure 27: Plan view of detonation chamber showing mounting positions of pressure transducers

4.3.1 APPARATUS

Details of the apparatus, tests and results are presented in appendix D. The detonation chamber used in these tests followed the design reported by Maly et al [34] and comprised a rigid channel, with inlet and outlet ports at either end, as shown in figure 27. Fuel and oxidant were mixed and allowed to flow continuously through the channel. A spark-plug, positioned at the end of the chamber, was fired at regular intervals so that, with the correct choice of reactants, a detonation wave was produced. Either an aluminium specimen or a pressure transducer was mounted at the end of the chamber (opposite the spark-plug), to be exposed to the detonation conditions.

A gaseous mixture of ethylene and oxygen was used as it has an energy density at atmospheric pressures that is similar to the end-gas in an engine at auto-ignition. These reactants produce a detonation wave at atmospheric pressures. The shock intensity was adjusted by changing the mixture strength.

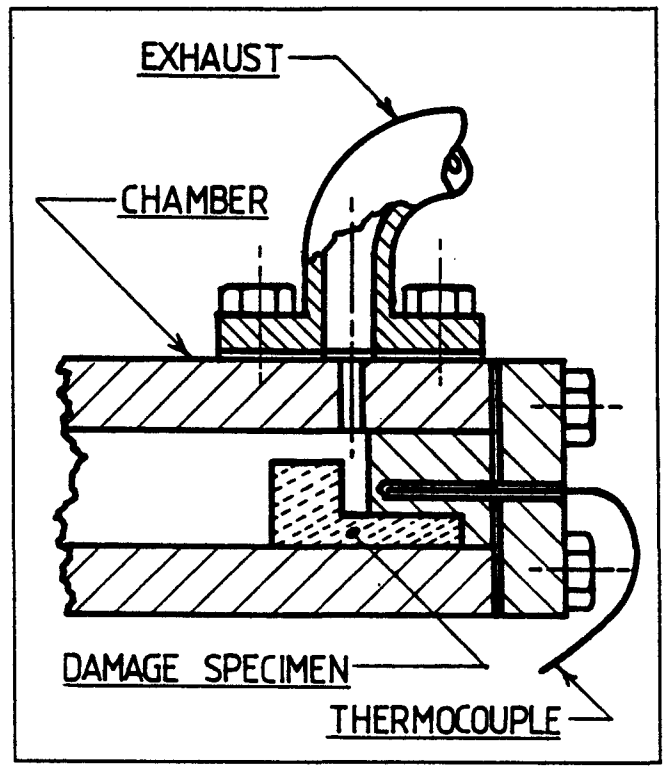

Figure 28: Section through specimen-end of detonation chamber

A cooling system was added to the chamber so that steady-state conditions could be maintained and that the damage specimen temperature could be controlled. Instrumentation used in these tests included pressure transducers and thermocouples positioned at various points (depending on the tests performed).

Figure 28 shows a cross-section of the chamber together with the damage specimen. The shape of the specimen corresponded to the top-land crevice region in an engine, as explained in appendix D. In some tests, the crevice gap was varied in order to investigate the effect

of geometry on erosion damage. As shown in figure 28, a thermocouple was placed close to the wall surface in order to investigate the effect of material temperatures on erosion damage.

4.3.2 EXPERIMENTAL METHOD

Using a pressure transducer mounted at the end of the chamber (in place of a damage specimen), tests were performed to determine the detonation pressure over a range of mixture strengths, see Appendix D. These tests and were used to validate the detonation model, as discussed in section 4.1.1.

Further tests were performed on damage specimens, which were subjected to 10 000 detonation pulses under controlled conditions. In these tests a subjective damage intensity scale was used to quantify the damage, similar to that described by Maly et al. Despite the limitations, it was possible to accurately order the specimens in terms of damage relative to each other.

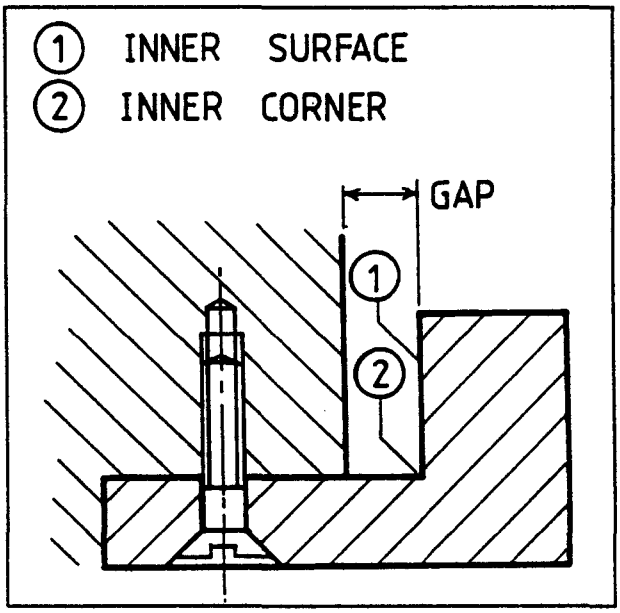

Figure 29: Regions evaluated for damage

The inner surface and the inner corner, shown in figure 29, were given damage ratings of between 0 (no damage) and 10 (extreme damage).

4.3.3 RESULTS AND DISCUSSION

Figure 30 shows the detonation chamber erosion damage intensity as a function of equivalence ratio with other initial conditions held constant (specimen temperature of 190°C). There was a progressive increase in erosion damage with increased mixture strength, which was also reported by Maly et al [34].

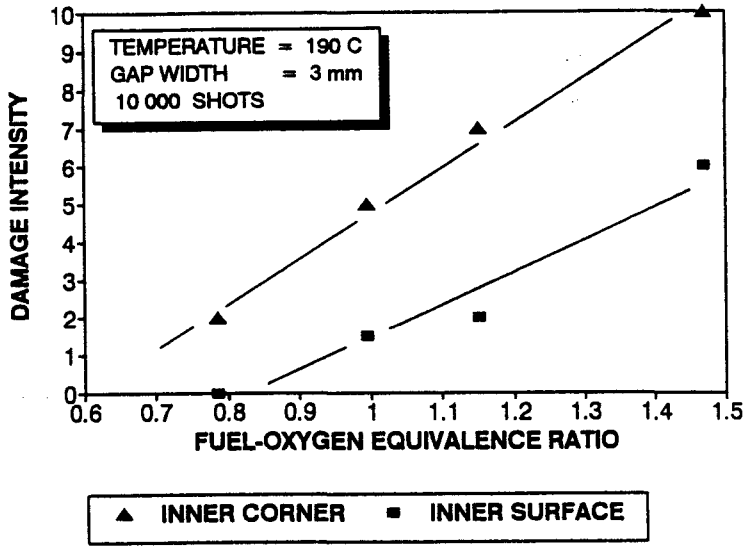

Figure 30: Effect of mixture strength on damage intensity

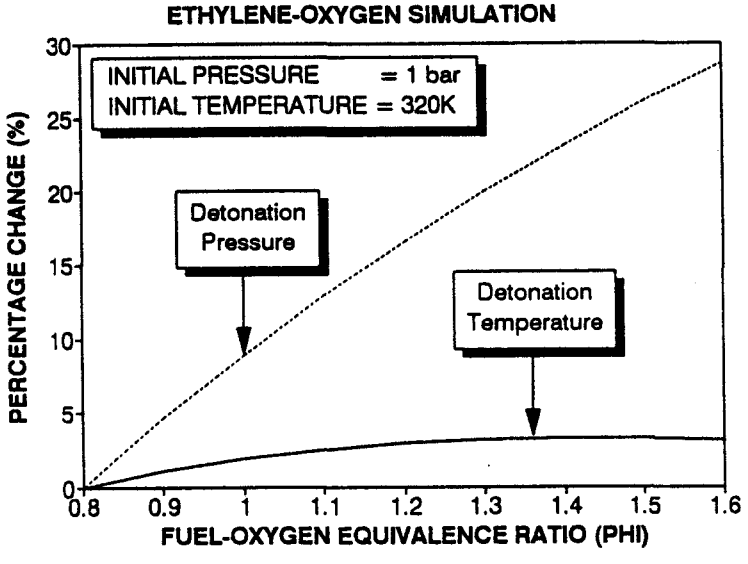

Figure 31: Detonation pressure and temperature vs mixture strength

Figure 31 shows the modelled detonation pressures and temperatures for the same initial conditions as the tests depicted in figure 30. These data are presented as percentage increases in temperature and pressure relative to conditions at an equivalence ratio of 0.8. It is seen that the detonation pressure increases by 30% over the equivalence range used in

the damage tests. Conversely, the detonation temperature increases by only 3% over the same mixture range.

It was concluded that the detonation pressure was a dominant parameter which influences the changes in damage intensities observed in these tests. Since the detonation temperature, as predicted by the model, was comparatively unchanged over the equivalence ratio tested, it could not be established to what extent the thermal effects might be involved in the surface destruction (see section 4.2).

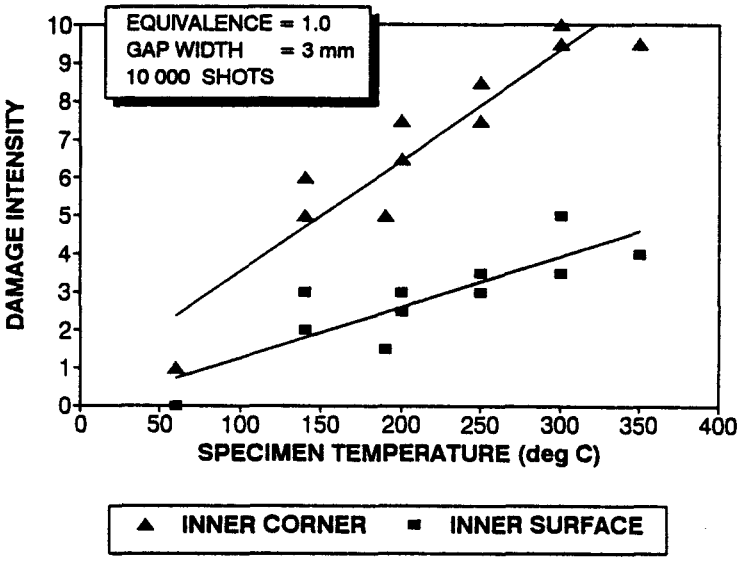

Figure 32: Effect of specimen temperature on damage intensity

Figure 32 shows the results of the damage tests performed over a range of specimen temperatures, in which it was seen that increased material temperature significantly increases the degree of erosion damage. The most significant erosion was found at the inner corner (marked 2 in figure 29) where an undercut developed on all specimens tested above 200°C. At temperatures above 300°C a cavity of over 1mm deep developed in the corner for all specimens. The increased damage at elevated temperatures was attributed to the reduction in yield strength. For this aluminium alloy, at 190°C the 0.2% proof stress is nearly halved, while at 350°C it is only 10% of its value at ambient temperatures [74].

In all the tests performed, the front surface of the specimens (facing the oncoming shock) was relatively undamaged, irrespective of the level of erosion occurring inside the crevice.

This illustrated the importance of the wave interaction in the crevice region, and explained why erosion is rarely found on unbounded piston and head surfaces.

Photographs, at high magnification, were taken of the damage specimens. Examination revealed that the surfaces were similar to the erosion structure found on the piston specimens. This will be discussed in a later section.

4.4 ENGINE TESTS

Engine experiments were conducted to test the reliability of the qualitative predictions made during the theoretical analysis. An important goal was the identification of a knock parameter which described the potential of knock to cause erosion damage.

4.4.1 DEVELOPMENT OF EXPERIMENTAL METHOD

The experimental approach adopted for this research included the following phases (see Appendix E for details):

(a) Engine modification:

A Ricardo E6 research engine was modified so that an aluminium specimen could be inserted into a cavity in the combustion chamber which was arranged to correspond to the end-gas zone. To accomplish this, a 12mm spacer plate was designed and fitted between the cylinder-head and bore. This is shown in figure 33.

A longer connecting-rod was manufactured and used to accommodate the increased cylinder volume, allowing the normal range of compression ratios to be achieved.

(b) Development of specimen geometry

The geometry of the specimen was optimised for greatest susceptibility to erosion damage. This was achieved by testing various specimen geometries under similar knocking conditions. The specimen geometry finally adopted, shown in figure 34, produced significant erosion after 15 to 30 minutes of testing.

The erosion was found to occur within the specimen crevice, as shown in figure 34. The inner corners of the crevice were seen to be preferentially damaged, as was the case in the detonation chamber experiments.

(d) **Erosion damage intensity measurement**

A method was developed to objectively measure the extent of the specimen erosion. This involved photographing cross-sections of the damaged specimens and digitizing the images. By subtracting the imaged area of the eroded specimen from the original profile, an objective measure of the magnitude of erosion was established, which will be referred to as the Damage Intensity (DI).

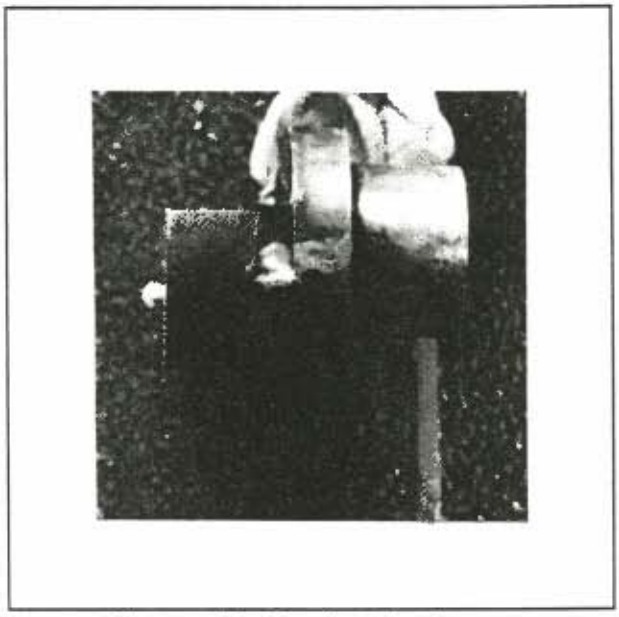

Figure 35: Engine Specimen showing erosion damage

4.4.2 EXPERIMENTAL METHOD

Specimens were tested over a variety of operating conditions and fuel types. The main control conditions chosen are shown in table I.

Table I: Operating conditions

Engine speed, load		1000 rpm, WOT	
Fuel-Air Equivalence Ratio		0.9	
Inlet air temperature		120°C and 165°C	
Fuel	Compression ratio	93 RON	8.5:1
		97 RON	9.7:1
		Methanol	9.5:1
Spark-Timing		10° to 40°CA BTDC	
Test duration		20 minutes	

A pressure transducer was positioned in the cylinder-head, adjacent to the specimen cavity (see figure 33). As detailed in Appendix E, the data collected included the cylinder pressure at the onset of knock and the maximum amplitude of the pressure oscillations, which were

averaged over 1000 cycles. Since an analogue filter was used, it was not possible to measure the absolute values of the amplitude of pressure oscillations. However, the measured output was proportional to the absolute pressure amplitude. The mean value of this parameter will be referred to as the Knock Intensity Factor (KIF).

4.4.2 RESULTS AND DISCUSSION

Examination of the specimens under optical and electron microscopes revealed a similar texture to the surfaces examined from the piston specimens (chapter 3) and the detonation chamber specimens (section 4.3). Figures 36, 37 and 38 show examples of electronmicrographs at similar magnifications of 1500 times.

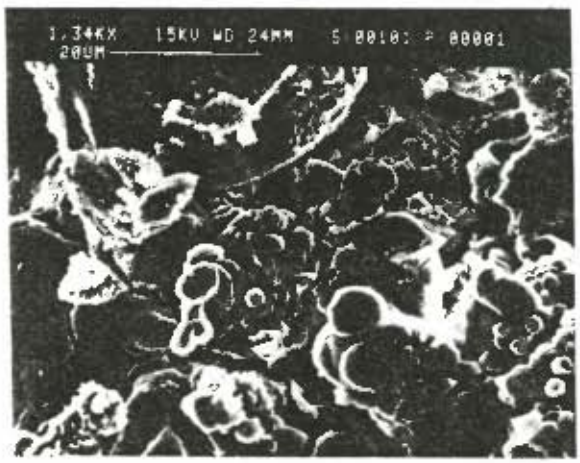

Figure 36: Micrograph from piston specimen #2

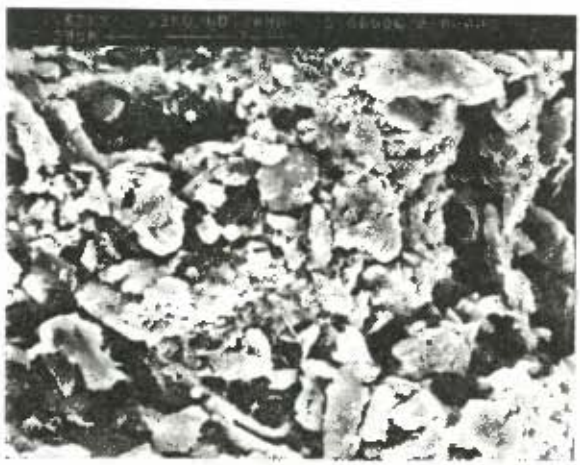

Figure 37: Micrograph from engine erosion tests

The detonation chamber specimen shown in figure 38 was tested at 350°C and illustrates the onset of molten structure on the protuberances. Specimens tested at lower temperatures did not exhibit this characteristic and were similar to those seen in figures 36 and 37. It was concluded that the erosion process was the same in all cases.

During the experimental phase of specimen geometry development, some specimens were tested with a thinner front wall than the one finally adopted. After testing under knocking conditions, it was found that the front wall of these specimens had been bent outwards by as much as 0.8mm. A fortuitous side-effect of these preliminary tests was the ability to estimate the true detonation pressure by considering the material properties and the mode of plastic deformation. The details of these calculations are presented in Appendix E.

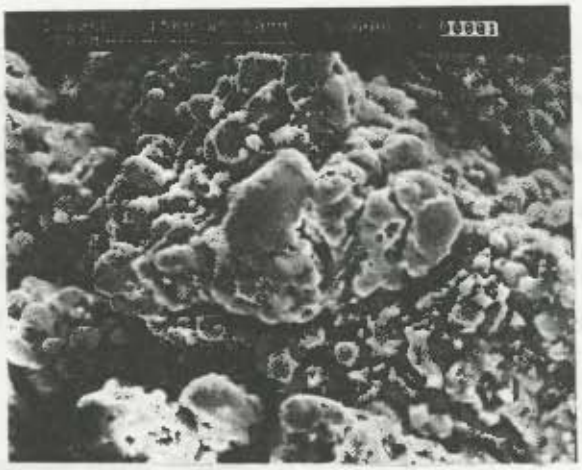

Figure 38: Micrograph from detonation chamber specimen at 350°C

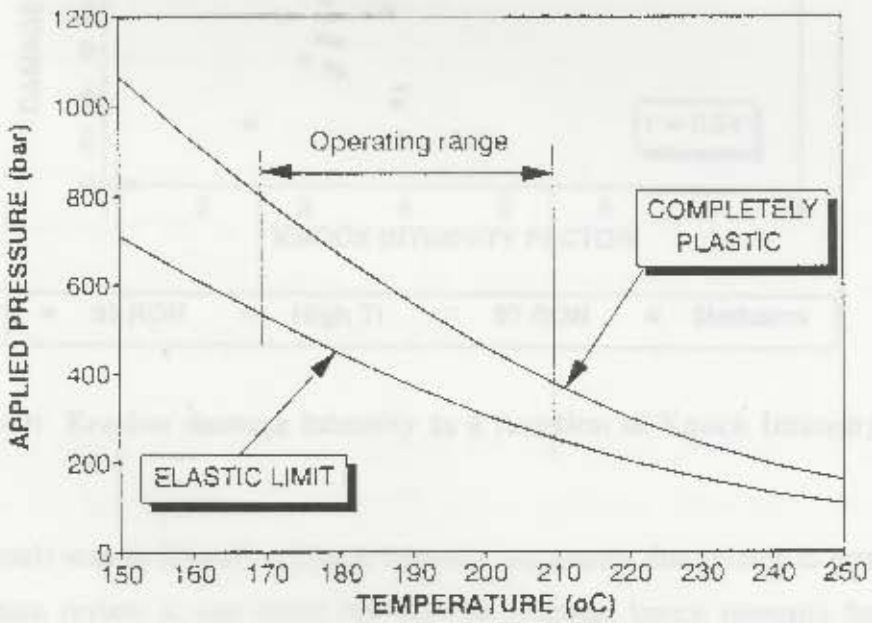

Figure 39: Pressure differential necessary to cause bending of specimen

Figure 39 shows the results of these calculations as a function of specimen temperature. The lower curve shows the pressure differential necessary to reach the elastic limit at the base of the wall, while the upper curve indicates the condition where the base has become completely plastic. It is probable that complete plasticity was attained, as indicated by the extent of the specimen deformation. Furthermore, due to assumptions made in the calculations, these

results constitute an under-estimate of the actual pressures occurring in the crevice. It was concluded that pressures in excess of 350 bar had been responsible for the observed damage.

With the limited ability of conventional pressure transducers to measure the true shock wave pressures, this analysis provided an independent estimation of local end-gas pressures (in the crevice regions). The estimated pressure in excess of 350 bar would correspond to a detonation pressure of about 200 bar (allowing for wave reflection at the wall [34]). This pressure is the same order of magnitude as the detonation pressures calculated with the detonation model.

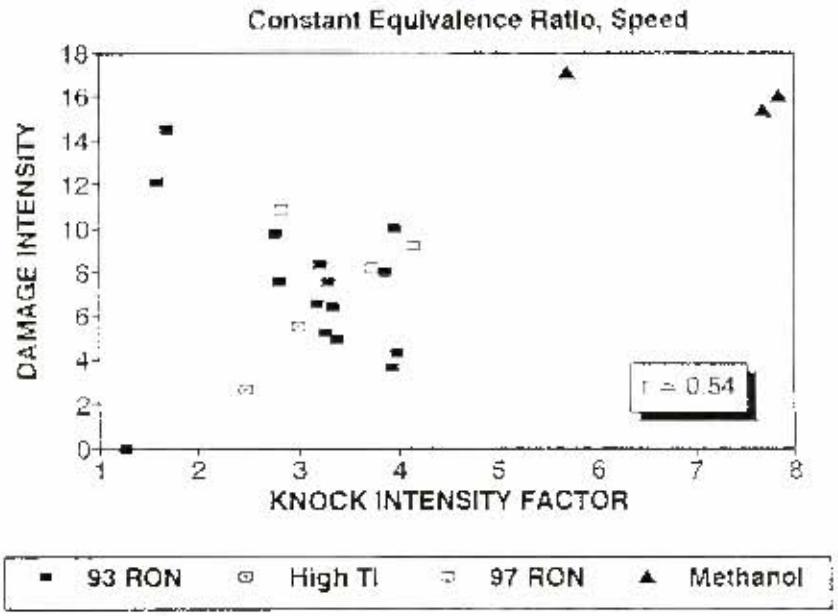

Figure 40: Erosion damage intensity as a function of Knock Intensity Factor

One of the goals was to identify a knock intensity parameter that relates to erosion damage. In the literature review it was noted that the conventional knock intensity factors (usually defined as a function of the maximum pressure amplitude of resonance) did not necessarily describe the localised conditions in the end-gas region. A series of erosion tests were performed over a wide range of spark-timing settings using 93 RON and 97 RON gasoline, and methanol. These tests were conducted at similar equivalence ratio and engine speed. Figure 40 shows the resulting damage intensity as a function of Knock Intensity Factor (mean maximum pressure amplitude). The two data points, indicated in the legend as "High Ti", were obtained with an inlet air temperature of 165°C, using 93 RON gasoline. The

remainder of the data were measured using an inlet temperature of 120°C.

A poor correlation coefficient of 0.54 was obtained for these 23 data pairs. If the methanol data were excluded from this graph, the remaining data would indicate a negative gradient of reducing damage with increased Knock Intensity Factor. This would completely contradict the use of this Knock Intensity Factor as an indicator of erosion damage.

Based on the detonation model (section 4.1.6), it was proposed that the cylinder pressure at the onset of knock may be a good indicator of damage intensity. Figure 41 shows the correlation between this knock parameter and damage intensity, using the same experimental data shown in figure 40.

The correlation coefficient for these 23 data pairs was 0.81, which was a significantly stronger correlation than that using the Knock Intensity Factor. These results illustrate that the cylinder pressure at the onset of knock is a reasonable indicator of the propensity of knock to cause erosion damage.

A linear regression through these data (also shown in figure 41) indicates that there should be no damage detected below pressures of 33 bar at the onset of knock. This is a very important observation, as it indicated that the knock parameter included a knock-damage criterion, below which no damage would occur.

The detonation model was used to simulate the detonation pressures for the operating conditions in the engine tests. Figure 39 shows predicted detonation pressures for the cylinder pressure range tested, using both methanol and octane. For octane, inlet air temperatures of 120°C and 165°C were used, which corresponded to those tested. The inlet temperature of methanol was reduced by 22°C relative to the test temperature, in accordance with the evaporative cooling effect [72], discussed previously in section 4.1.5. A polytropic relationship, described in section 4.1.5, was used to estimate the end-gas temperature at the onset of knock.

A comparison of figures 40 and 41 shows that the relative positioning of the data groups corresponded to that predicted by the model. The damage indices for the methanol data were

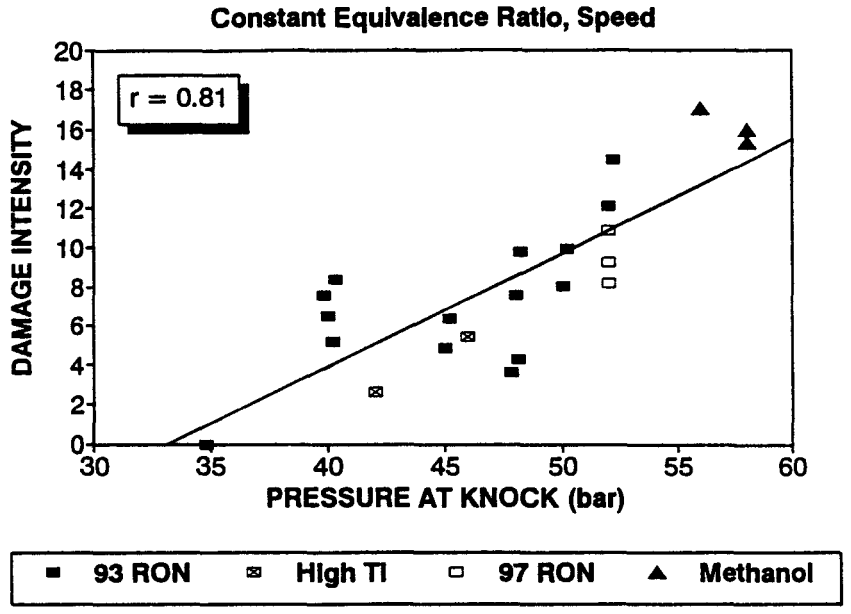

Figure 41: Erosion damage intensity as a function of cylinder pressure at knock

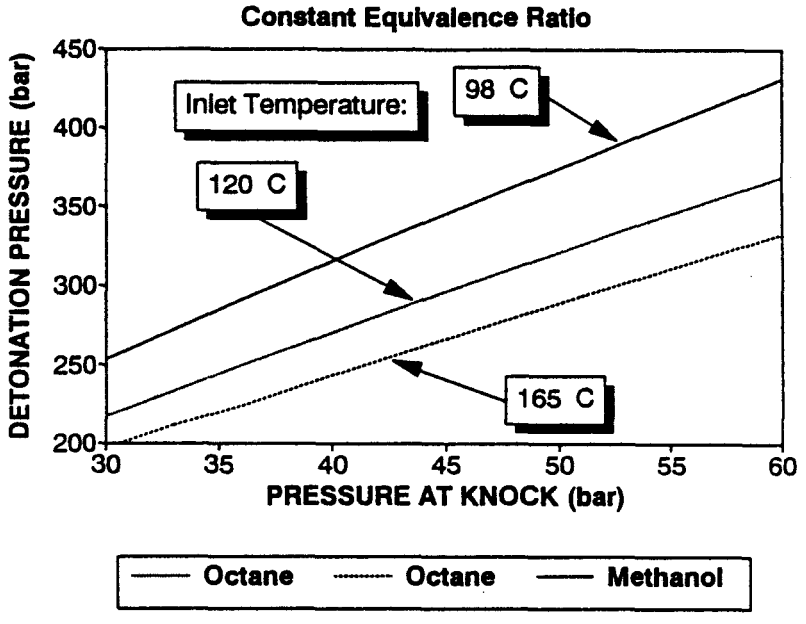

Figure 42: Modelled detonation pressure using engine test conditions

above the regression line, as expected, considering the predicted detonation pressures for this fuel. It should be noted that six specimens were tested with methanol, however three were completely disintegrated during the 20 minute duration. This indicates that the damage intensity using methanol is even higher than those illustrated in the data.

The damage indices for gasoline with high inlet temperature, are below the regression line,

as predicted in section 4.1.5.

The similarity between these two graphs is striking, and supports the use the detonation model for predicting the effect of engine operating conditions on erosion damage. Furthermore, it shows that the modelled detonation pressure is a reasonable indication of the erosion damage potential.

4.5 QUANTIFICATION OF EROSION DAMAGE

A means of quantifying knock in terms of the propensity to cause erosion damage was proposed. With a knowledge of the cylinder pressure (prior to knock) at which knock causes erosion damage, it was possible to establish a safety margin for all knocking conditions.

Before discussing the nature of this safety margin, the following methodology is proposed for recording the necessary data. An instrumented engine would be operated on a bench dynamometer under controlled knocking conditions by varying the spark-timing and holding load, fuel type, inlet air temperature and engine speed constant. Gradually increasing the spark-advance and checking for erosion damage (by dismantling the engine or using a borescope) the cylinder pressure at knock at which erosion is first detected would be established. This cylinder pressure (p_e) constitutes the damage criterion for the particular engine geometry and operating conditions.

A safety margin for erosion damage (SM_e) may be defined as the fraction of the damage criterion (p_k) remaining prior to the onset of erosion damage (p_e), as follows:

$$SM_e \equiv 1 - \frac{p_k}{p_e}$$

where p_k - cylinder pressure at the onset of knock for the particular knocking condition

Using this definition, the engine or fuel developer would have knowledge of the safety margin for engines and fuels operating with knock, but without erosion damage.

CHAPTER 5

HEAT FLUX INVESTIGATION

This investigation was aimed at understanding and quantifying the damaging effects of the increased heat flux caused by knock. Following the observations and deductions concerning the damaged specimens (chapter 3), it was suspected that the following types of failure were caused by knock-induced heat flux:

- Piston seizure
- Ring seizure
- Rings jammed inside ring grooves
- Fractured rings
- Fracture piston lands

Piston seizure due to knock is well documented and therefore the main focus of this chapter is on the failure of the compression rings and related damage. Some of the experimentation presented in this chapter was performed under the author's direct supervision and guidance, and is referenced accordingly.

The investigation into the heat flux mechanism of damage was assisted by the failure analysis of the piston specimen #6 (figure 14). A description of this eroded piston with fractured second land was given in section 3.1.3, together with additional details. Most of the damage features to be investigated in this chapter are found on this particular specimen. Both compression rings were jammed in their grooves and the ring gaps had significantly increased.

It was intriguing to note that a ring seizure (as seen on the bore) had occurred with an increase in ring gap. The ends of the rings were not damaged, indicating that the circumferential length of the rings had somehow shortened. Therefore, an explanation was sought that could relate the ring seizure, increase in ring gap and the jamming of the rings in their grooves. Furthermore, it was suspected that the fracture of the piston land, also

found on this piston, was a related symptom.

A hypothesis was developed which explained some of these observations and which is illustrated in figure 43. When cold, there is a ring gap of between 0.5 to 1 mm for a typical automotive engine [81], as shown in figure 43A. There is also side clearance between the groove and ring, of between 0.02mm and 0.1mm [81]. Under normal operating conditions, shown in figure 43B, the ring gap is reduced due to thermal expansion of the ring. In addition, the side clearance is increased by the relatively greater thermal expansion of the piston material.

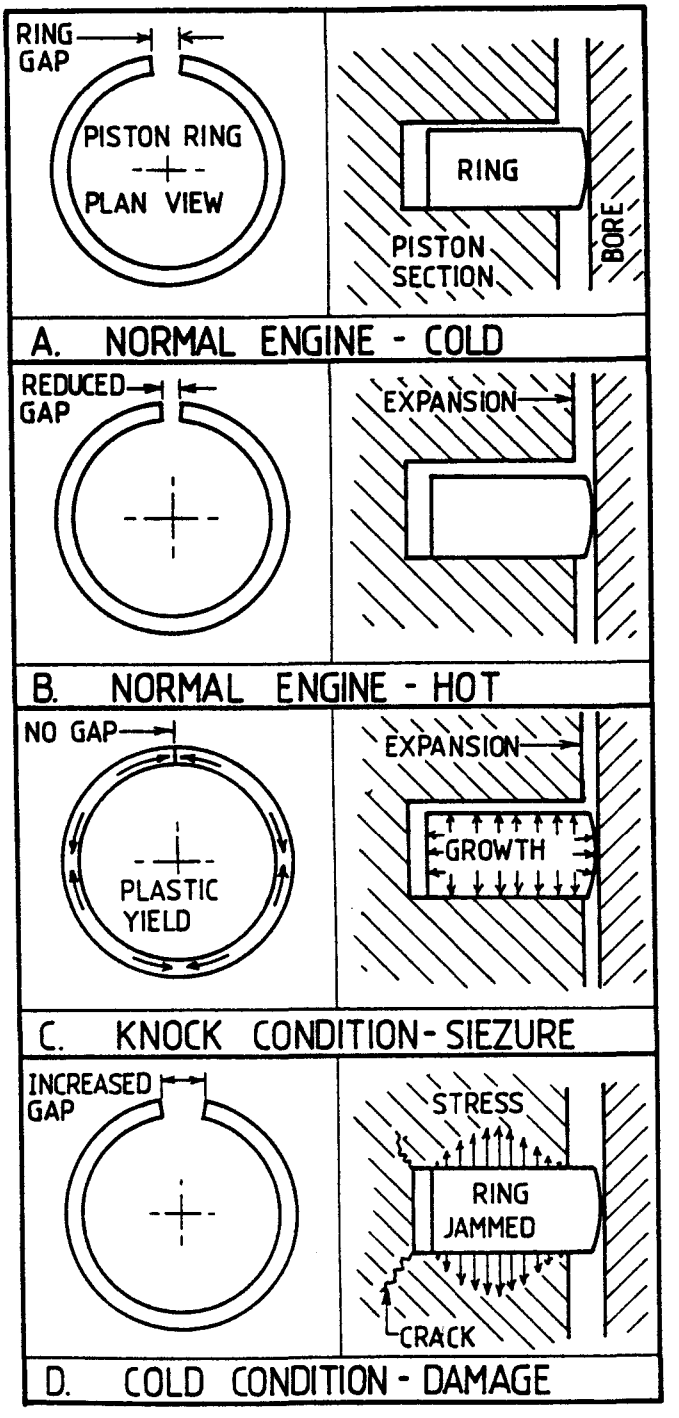

Figure 43: Ring gap closure and damage

During knocking operation, the ring gap may close due to elevated heat flux, as illustrated in figure 43C. Further thermal expansion caused by continued operation under these conditions would cause hoop and radial stresses to be set up in the ring with an attendant increase in friction and a drastic increase in the ring temperature. It is deduced that the elevated temperatures and stresses would cause the ring to plastically yield uniaxially in an attempt to relieve the stresses. During this high temperature phase, it is further proposed that a permanent increase in the ring thickness occurs. It was initially considered that the Poisson (lateral) strain was responsible for the permanent expansion.

On cooling, the piston would contract, jamming the thicker ring in the groove which would result in bending and shear stresses being applied to the piston lands as shown in figure 43D. Cracks would result from the normal low-cycle thermal loading produced by the duty cycle of the engine, ultimately resulting in piston land fracture. The cold ring gap would also have increased due to compressive yield that took place.

In order to validate this hypothesis, three questions needed to be answered:

- Is the effect of elevated heat flux from knock sufficient to close the ring gap?
- If the ring gap does close, will sufficient stress be developed to cause the ring to plastically yield in the circumferential direction?
- What mechanism causes the ring thickness to permanently increase?

The investigation was divided into the following sections:

(1) A theoretical and experimental study was performed to determine the effect of knock on the ring gap.

(2) The extent of plastic yield of the piston rings under simulated ring seizure was investigated.

(3) An investigation was undertaken to determine the cause of lateral ring growth (resulting in the rings jamming in their grooves).

The results of these studies were used to identify a knock intensity parameter and quantify the safety margin of knocking operation with respect to piston and ring failure mechanisms.

5.1 RING GAP INVESTIGATION

A means of measuring the ring gap in a running engine was developed. This tool was used to correlate the effect of knock intensity on the operational ring gap. This was preceded by a theoretical analysis of the problem. Together with experimental data, the theory was used to identify the knock intensity criterion which correctly quantifies the ring gap closure process.

5.1.1 THEORETICAL DEVELOPMENT

In order to interpret any experimental data, it was necessary to gain a theoretical understanding of the effect of knock intensity on thermal expansion of the piston ring. No theoretical model concerning this phenomenon could be found in the literature. An existing heat transfer model was modified to account for the effect of knock intensity and extended to include the thermal expansion of the ring. A relationship between knock intensity and changes in ring gap was established from this model. This was intended to be a first step in modelling this phenomenon. Two different knock intensity criteria were evaluated to identify the correct means of quantifying this phenomenon. The details of the model and its development are presented in Appendix F.

Taylor and Toong [75] correlated the overall heat transfer data from 19 engines and found they fitted the general form:

$$Nu = C\, Re^{n}$$

where	Nu	- Nusselt Number
	Re	- Reynold's Number
	$C,\ n$	- constants

The value of the constant "n" has been measured [76] and given a range between 0.6 and 0.8, depending on the choice of variables, engine types and conditions.

Under knocking combustion, there are gas velocities induced by the pressure variations associated with the chamber resonance. These velocities are responsible for the knock-induced global heat flux (as discussed in chapter 2) and are in addition to the velocities caused by piston motion and combustion turbulence. This analysis ignores the local heat flux caused by the auto-ignition process, which is confined to the end-gas region.

As a first approximation, it was assumed that the average conditions are unchanged (with respect to normal combustion) and the knocking pressure amplitude (of the resonance) was used to describe the additional gas velocity. The mean amplitude of the knock pressure fluctuations (Δp_k) was assumed to be related to the knock-induced gas velocities. This was done in a similar manner to the formulations based on the combustion pressure rise proposed by Woschni [77] for combustion heat transfer.

From the consideration of energy conservation (and with all else constant), a pressure difference (Δp_k) within a chamber would give rise to a proportionate increase in the kinetic energy of the gas. Expressed in terms of gas velocities (u_k):

$$u_k^2 \propto \Delta p_k$$

It is argued in Appendix F that the heat flux during knock dominates the heat transfer process, and thus the mean pressure amplitude could be combined with the Taylor-Toong relationship to give a hypothetical heat transfer coefficient describing the heat flux due to knock.

Assuming light knock implies that gas and coolant temperatures remain approximately unchanged from non-knocking conditions (such as might be obtained with a higher octane fuel). Under these circumstances, the temperature rise of the chamber walls, due to knock alone could be calculated.

The ring was considered to be part of the piston and was assumed to experience a temperature rise proportional to the rest of the wall material, as justified in Appendix F. The change in ring gap as a result of this temperature rise was determined using the thermal

expansion coefficient and the circumferential length of the ring.

It was assumed that the expansion of the bore, due to knocking heat flux, was negligible. This was justified by the fact that it is materially constrained compared to the free-floating rings, and that the heat flux is distributed over the length of the bore.

RING GAP MODEL #1

Two ring gap models were proposed (see Appendix F). The first was expressed as follows:

$$\Delta RG \approx C_2 (\Delta p_k)^{\frac{n}{2}}$$

where ΔRG - reduction in ring gap due to knock alone

Δp_k - mean pressure amplitude

C_2 - constant

and $0.6 < n < 0.8$

This model was developed with the assumption that the pressure oscillations which drive the heat transfer process occur repeatable (by using the Taylor and Toong equation). However, at light knock conditions, not all the cycles are knocking, as discussed in section 2.2. Therefore, a method had to be established to account for the effect of non-knocking cycles. A simple approach was to include the zero pressure values (for the non-knocking cycles) in the mean pressure amplitude. Thus, the **Knock Intensity (Δp_k) was defined as the mean pressure amplitude of all cycles**. It is emphasised that this knock intensity is, by definition, a function of the fraction of cycles knocking. A comparison between the experimental data and the model using this Knock Intensity was used to test the accuracy of this model.

These models represent a simplified attempt at predicting and understanding the general relationship expected in the experimental stage of this study. To have attempted to predict the absolute values of the ring temperatures as a function of knock amplitude would have meant developing a full heat transfer model of the piston-to-ring groove-to-ring heat transfer process, which is beyond the scope of this research. Therefore, the constant (C_2) was not analyzed, but its value was determined by a least squares fit to the experimental data.

5.1.2 EXPERIMENTAL STUDY OF RING GAP

The aim of this experimentation was to determine the effect of knock intensity on the ring gap in a running engine. To the author's knowledge, this is the first time that this type of measurement has been attempted. A portion of this study has already been published [78].

Details of the test methodology, equipment and results are presented in Appendix F. A Waukesha CFR engine was operated at steady-state conditions. Using low octane gasoline, knocking combustion was induced and its intensity varied by altering the ignition timing. High octane fuel was then tested, so that the effect of spark-advance, which itself causes a change in heat flux, could be eliminated. The high octane fuel did not knock under any of the operating conditions. To a first approximation, the data corrected in this way would satisfy the model assumptions whilst permitting the knock pressure amplitude to be varied.

Knock intensities Δp_k and Δp_{kk} were obtained from the mean pressure amplitude (peak-to-peak) for one hundred cycles as well as the fraction of cycles knocking.

A method of measuring the operational ring gap was developed. A mechanical system was used which necessitated the removal of the piston between each test run. The ends of the top compression ring were machined into sharp scribes and an aluminium shim was placed behind the scribes. A curved spring steel plate was placed behind the aluminium shim, inside the ring groove so as to force the shim against the scribes. As the ring gap closed during engine operation, two witness marks were made on the aluminium by the scribes. After completion of a test run, the plate was removed and the minimum ring gap was measured.

To cross-check the experimental method, the ring temperature was measured during testing. A thermocouple was placed in the ring groove, in contact with the inside surface of the ring. The thermocouple wire led out of the block by means of a mechanism designed for the purpose.

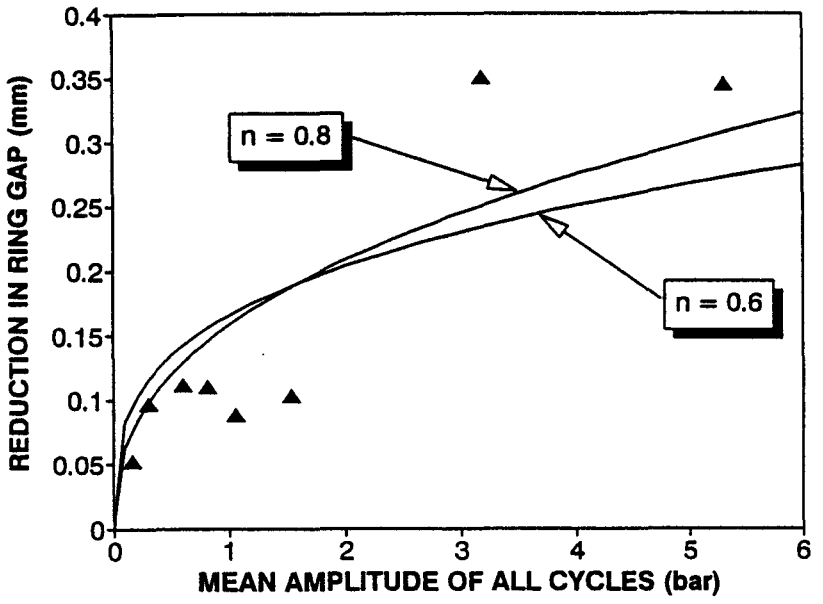

Figure 44: Experimental and Theoretical results based on mean pressure amplitude of all cycles

Figure 44 shows the change in ring gap plotted against the knock intensity Δp_k defined as the mean pressure amplitude of all cycles, used in the first model.

The second model was tested by plotting the ring gap data against the alternative knock intensity Δp_{kk} defined as the mean pressure amplitude of knocking cycles, which is shown in figure 45.

The theoretical curves in these figures corresponds to the models based on the appropriate definition of knock intensity. The modelled relationships have been plotted for the extremities of the exponent n, reported by Ferguson [76]. It is expected that the true engine condition would lie between these two curves. In each case, a least squares fit was performed to estimate the constant C_2.

Comparing figures 44 and 45, it is seen that the second model (figure 45), based on the mean

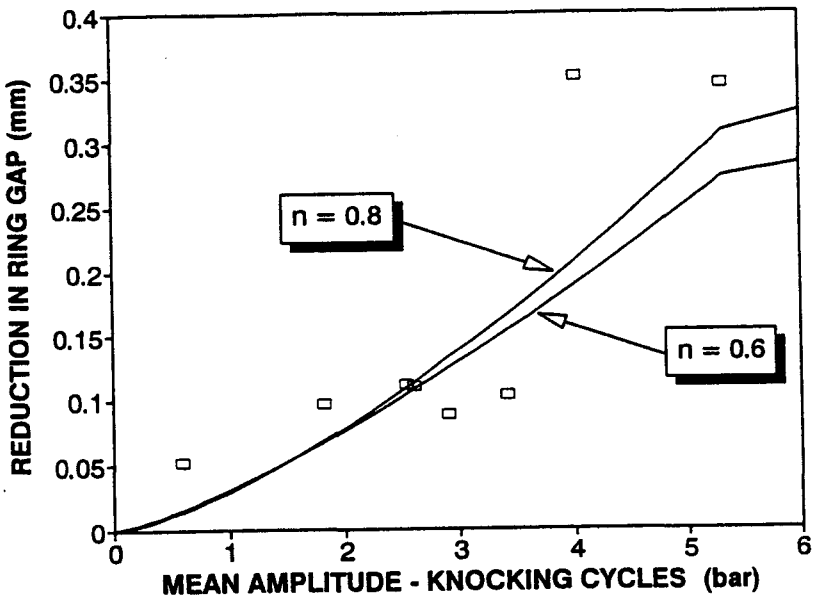

Figure 45: Experimental and Theoretical results based on mean pressure amplitude of knocking cycles alone

amplitude of knocking cycles, fits the experimental data with greater accuracy. This suggests that the effect of non-knocking cycles is to modify the amount of heat transfer, and not the knock intensity itself. Furthermore, it establishes (to within the limits of these data) that the knock intensity, defined as the mean pressure amplitude of knocking cycles, is the correct index to use in cases where global heat flux effects are of interest.

The ring temperature together with measured ring gap data were used to calculate the apparent coefficient of thermal expansion of the ring. As shown in appendix F, the value derived in this manner was sufficiently close to the coefficient for ring material, so as to confirm the accuracy of this ring gap measurement procedure.

A significant observation was the magnitude of ring gap closure due to knock. A ring gap closure of 0.3 mm constitutes a large fraction of the cold ring gap, which is typically between 0.5 and 1mm [81]. Furthermore, this value of ring gap closure was measured at relatively light knocking conditions. Extrapolating this data to higher knock intensities (using the modelled trend) indicates that total ring gap closure could occur at medium to heavy knock conditions, depending on the cold ring gap and engine configuration.

5.2 RING SEIZURE AND YIELD STUDY

Under heavy knock, at the point of ring gap closure, the compression ring becomes a solid ring confined by the bore. Under these conditions, the ring would be expected to seize in the bore and, due to friction, its temperature would rise rapidly. Commensurate with the temperature increase, the ring would experience a compressive stress caused by the thermal expansion of the ring and the confinement of the bore.

This section investigates the extent of plastic yield of the ring under these conditions. This theoretical and experimental study was motivated by a need to understand the mechanism by which the ring gap increased in the Specimen #6 case study. The details of the work discussed in this section are presented in Appendix G.

5.2.1 ANALYSIS OF STRAIN IN A SEIZING RING

In contrast to the ring, the bore would experience only a minor temperature increase as the heat flux from the seizing ring is spread over the entire length of the externally cooled cylinder. Therefore, the change in bore dimension was ignored.

To model the seizure process, a ring was confined in a constant diameter bore and was heated. As a consequence, hoop (circumferential) stresses were developed to levels determined by the temperature and material properties of the ring. When the applied stress exceeded the yield stress of the material, plastic yield occurred, permanently shortening the length of the ring. On cooling, the cold ring gap would have increased.

A simple model was developed using standard equations to describe thermal expansion and material properties. The plastic strain (ε_p) was calculated from the difference between the total thermal strain and the maximum permissible elastic strain as follows:

$$\varepsilon_p = \alpha \Delta T - \frac{\sigma_y}{E}$$

where	α	-	coefficient of expansion (1/°C)
	ΔT	-	temperature increase above the point of gap closure (°C)
	σ_y	-	yield stress (MPa)
	E	-	elastic modulus (Mpa)

5.2.2 EXPERIMENTAL STUDY OF RING YIELD

Details of this test procedure are presented in appendix G. A test rig was developed comprising of a water cooled cylinder and a gas burner. A standard compression ring was fitted into the bore. The ring gap was measured and then blocked by means of an adjustable wedge. The ring was heated to the test temperature, as monitored by thermocouples. After cooling, the ring gap was measured again. The difference in ring gap was used to produce data pairs comprising of the test temperature and measured plastic strain. Nineteen rings were tested in this manner over a temperature range of 200°C to 450°C. The apparatus was not able to operate at higher temperatures, as the combination of burner and cooling system was unable to maintain a high temperature differential between the ring and cylinder.

To obtain data at higher temperatures, a test procedure was developed which involved the shrink-fitting of a heated, undersize cylinder over a cold, oversize ring-piston assembly. The differences in the thermal expansion of the ring and bore, together with the interference fit, were used to achieve the appropriate thermal stresses at elevated temperatures. The whole assembly was maintained at a test temperature inside a furnace. The piston and ring were then removed from the bore and allowed to cool. The change in ring gap was determined from measurements in an oversize reference cylinder, made before and after each test.

As these tests were to be used together with the burner test data, a means of applying equivalent thermal stress (at the test temperature) had to be established. Using the material properties of the ring and bore, together with thermal expansion relationships, an equation was developed relating the initial ring gap to the desired test temperature, as detailed in appendix G.

specimen #6.

It is interesting to note that, after the knock-induced yield had occurred and the engine allowed to cool, subsequent knocking operation was unlikely to repeat this process. Much greater temperatures would be necessary to cause the increased ring gap to close a second time.

5.3 RING GROWTH STUDY

The results of the ring seizure study, indicated an obvious mechanism for lateral ring growth. A ring experiencing a permanent longitudinal compression would show a corresponding increase in the transverse strain, as described by the Poisson's Ratio of the ring material. Based on the measured dimensions in the case study and typical values of the Poisson ratio, it was estimated that the increase in ring thickness would amount to about 0.002mm. These data and calculations are presented in Appendix H. It was apparent that this small amount of growth could not be responsible for the jamming of the rings in their grooves, given typical side clearances of between 0.02mm and 0.1mm [81]. Therefore the Poisson effect was not responsible for this damage.

To investigate the cause of the ring growth, a material examination was carried out on the compression rings from specimen #6, and new rings were used as a control. Dimensions were checked, Vicker's Hardness tests were made and the microstructures examined. Details of these data are contained in Appendix H.

Increases in both the lateral dimensions and hardness were evident from these data. Top ring width and thickness showed an increase of 10.5% and 11.7% respectively, relative to the reference rings. The second ring showed increases of 4.7% and 5.3%. If the growth had been caused by a thermal phenomenon, it was expected that the top ring would show a greater effect than the second ring, as it would have been exposed to higher temperatures [4]. Correspondingly, the hardness measurements also showed a progressive increase from control to top ring. It was therefore concluded that the process involved an increase in hardness and thickness with temperature.

The specimen #6 rings and the new rings were examined under a microscope. Details of the specimen preparation and photographs of the microstructure are presented in Appendix H. The examination was able to differentiate between the occurrence of flake graphite in pearlite and spheroidal free graphite in the cast iron matrix. It was found that the control rings contained a negligible amount of spheroidal graphite, while the specimen #6 rings possessed significant levels of the deposit. Spheroidal deposits in the top ring were in general greater than in the second ring. It was also observed that the length of the graphite flakes were in

general longer in the control rings compared to the specimen #6 rings.

Angus [79] reported that permanent dimensional growth occurs in grey cast iron at temperatures above 350°C, by the process of spheroidization. He attributed this growth to the breakdown of combined graphite and pearlite into spheroidal free graphite. Furthermore, he reported that an attendant increase in hardness was found with increased levels of spheroidization. From this description it was inferred that the final condition of the specimen #6 rings was due to spheroidization of the graphite.

5.3.1 EXPERIMENTAL STUDY OF RING GROWTH

Because the case study rings had not been examined prior to the failure, it was thought necessary to investigate whether the change could be re-created in the laboratory. To this end an experiment was devised to confirm this theory.

An apparatus was constructed to expose a piston and ring assembly (mounted in a bore) to high temperatures [80]. Details of this equipment and test procedure are presented in Appendix H. The lateral dimensions and hardness of a new compression ring was measured and fitted into the test rig. A gas burner was used as a heat source and together with thermocouples fitted against the test ring, the rig was allowed to soak at a chosen temperature. A temperature range from 280°C to 600°C was used in 11 separate tests. After cooling, the ring was removed and remeasured in terms of lateral dimensions and hardness, and its microstructure was examined.

5.3.2 RESULTS AND DISCUSSION

Three tests performed at temperatures below 315°C showed no significant changes in the dimension, hardness and microstructure.

At the conclusion of all tests performed at temperatures greater than 350°C, the rings were found jammed in the ring groove and had to be forcibly removed. The microstructures of these rings were found to contain significant levels of spheroidal free graphite, as in the case of the specimen #6 rings.

Surface hardness was found to increase progressively with temperature above 350°C, as shown in appendix H. At 600°C the hardness had increased by over 45%. The hardness values at the upper temperatures were slightly lower than those recorded on the specimen #6 rings, indicating that the case study rings were probably exposed to even higher temperatures than those tested. This is reasonable, as the source of the heat in the case study would have been the seizure of the rings themselves. In the case of this experiment the heat was supplied to the piston material, which thus limited the maximum temperature.

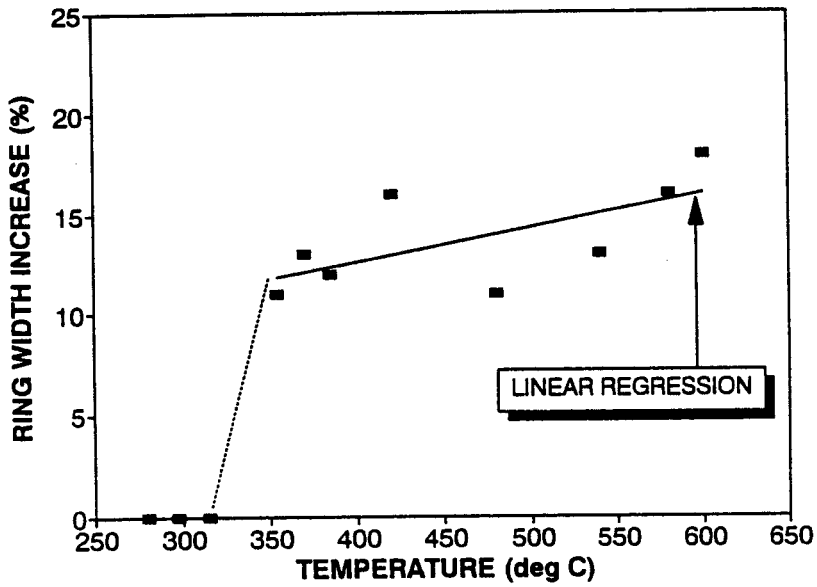

Figure 47: Lateral ring growth as a function of temperature

The results of the ring growth data are shown in figure 47, in which a linear regression has been performed to show the general trend. A lateral growth of between 11% and 18% was measured over the temperature range tested. The growth was relatively insensitive to temperature.

From the dimensional and hardness data, as well as the observations of the microstructure, it was clear that lateral ring growth has been caused by exposure to elevated temperatures which caused the diffusion of flake graphite to form spheroidal free graphite.

Spheroidization would also cause an increase in the circumferential length of the ring. However, it is evident from the results of the previous section that this growth is suppressed by the compressive strain during ring seizure.

5.4 RING DAMAGE MECHANISMS

The combination of these studies provided a reasonable explanation for the knock-induced mechanisms causing ring problems and fractured piston-lands. Knock causes elevated heat flux which in turn results in ring gap closure. At gap closure the ring begins to seize against the bore, substantially raising the ring temperature further and causing the formation of spheroidal free graphite which permanently increases the lateral dimensions of the ring. On cooling, the greater thermal contraction of the piston material results in the ring being jammed in its groove and producing bending and shear stresses on the piston lands. The low frequency duty cycle intermittently releases the ring when hot and jams the ring when cool, ultimately producing a fatigue failure of the piston land. Furthermore, the cold ring gap would also have increased due to the plastic yield that occurred under the knocking conditions, when the ring gap had completely closed. The longitudinal yield of the ring would relieve the ring seizure slightly.

At the beginning of this chapter a hypothesis was proposed to explain the observations from the knock-damaged specimens. Three questions were posed which have now been answered.

- Elevated heat flux due to knock is sufficient to cause complete ring gap closure.

- With complete gap closure, additional heat generated by seizure would cause the ring to plastically yield in the longitudinal direction.

- At temperatures above 350°C, the spheroidization of free graphite in the cast iron matrix causes a permanent dimensional growth of the ring.

These processes also serve to explain failure mechanisms not necessarily related to knock. For instance, abnormal ring temperatures would also occur during a cooling or lubrication system failure.

5.5 PISTON SEIZURE MECHANISMS

Reports of piston seizure, due to knock, were discussed in chapters 2 and 3. This damage mechanism was attributed to excessive thermal expansion of the piston caused by the elevated heat flux. Hence, the process follows an identical path to that causing complete ring gap closure.

The similarity between these two processes permits the relationship between piston seizure and knock intensity to be analyzed in the same manner. In the case of piston seizure, the "gap" now refers to the clearance between the piston and the bore.

5.6 QUANTIFICATION OF HEAT FLUX DAMAGE

One of the main goals of this thesis was to quantify knock in terms of its potential to cause damage. As shown in the literature review, previous knock intensities have been based on criteria which were chosen for the purpose of comparing parameters in terms of their propensity to cause knock. In contrast, it was the intention of this thesis to identify the knock intensity parameter which accurately describes the propensity to cause damage. Using this knock intensity, together with the theoretical model (developed in this chapter), a method was proposed to determine the safety margin of knocking conditions relative to failure.

Prior to determining the quantifying parameter, the particular type of damage had to be established. In this case, the propensity to cause damage related to heat flux was to be quantified. As shown in this chapter, knock-induced heat flux could result in many different types of failure. However, all these failure mechanisms are initiated by thermal expansion of the piston and rings.

The analytical and experimental work, earlier in this chapter, identified the appropriate knock intensity parameter (Δp_{kk}) related to these failure mechanisms. To simplify the notation to follow, the Knock Intensity (KI) is defined as the mean pressure amplitude of knocking cycles, that is:

$$KI \equiv \Delta p_{kk}$$

The ring modes of failure result from the complete closure of the ring gap, and in the case of piston seizure, it is the piston-bore clearance that closes. The condition which produces either type of gap closure, establishes a critical criterion for the onset of knock-induced failure. With the knowledge of this critical knock intensity, together with the theoretical relationship developed in this chapter, the safety margin for a particular operating condition may be evaluated.

Before discussing the nature of this safety margin, the following methodology is proposed for recording the necessary data, as follows. Operating an instrumented engine on a bench dynamometer, the knock intensity may be increased until partial seizure occurs (as seen by

a drop in torque from the dynamometer). This measured knock intensity (KI_s) constitutes the point at which total gap closure has occurred (either due to ring gap closure or piston seizure). It is noted that to apply the theoretical model (which is based on the effect of knock alone), the knock intensity would have to be increased by reducing the octane of the fuel. This could be accomplished by fitting a controllable mixing system using a high and a low octane fuel.

It is also necessary to measure knock intensity above which all cycles are knocking (KI_{100}). With these two data points (KI_s and KI_{100}) a safety margin may be established for all knock intensities (at this engine operating condition) by utilizing the ring gap model detailed in Appendix F.

The safety margin (SM) is defined as the fraction of the gap (either ring or piston-bore) remaining at a particular knock intensity (KI), as follows:

$$SM \equiv 1 - \frac{\Delta RG_{KI}}{\Delta RG_s}$$

where ΔRG_{KI} - change in gap due to the operating knock intensity (KI)

ΔRG_s - change in gap to produce seizure

The theoretical model establishes the change in gap as a function of knock intensity. There are two different expressions for this relationship, depending on whether or not all the cycles are knocking (ie: whether $KI >$ or $< KI_{100}$). Substituting the modelled function into the above equations results in:

$$for \qquad KI \; ; \; KI_s \leq KI_{100}:$$

$$SM = 1 - \left(\frac{KI}{KI_s}\right)^{\frac{n}{2}} \left(\frac{KI}{KI_s}\right)$$

$$for \quad KI \leq KI_{100} \quad and \quad KI_s > KI_{100}:$$

$$SM = 1 - \left(\frac{KI}{KI_s}\right)^{\frac{n}{2}}\left(\frac{KI}{KI_{100}}\right)$$

$$for \quad KI\ ;\ KI_s > KI_{100}:$$

$$SM = 1 - \left(\frac{KI}{KI_s}\right)^{\frac{n}{2}}$$

where $0.6 < n < 0.8$ [76]

Using these relationships, the engine or fuel developer is able to assess the safety margin at any knock intensity.

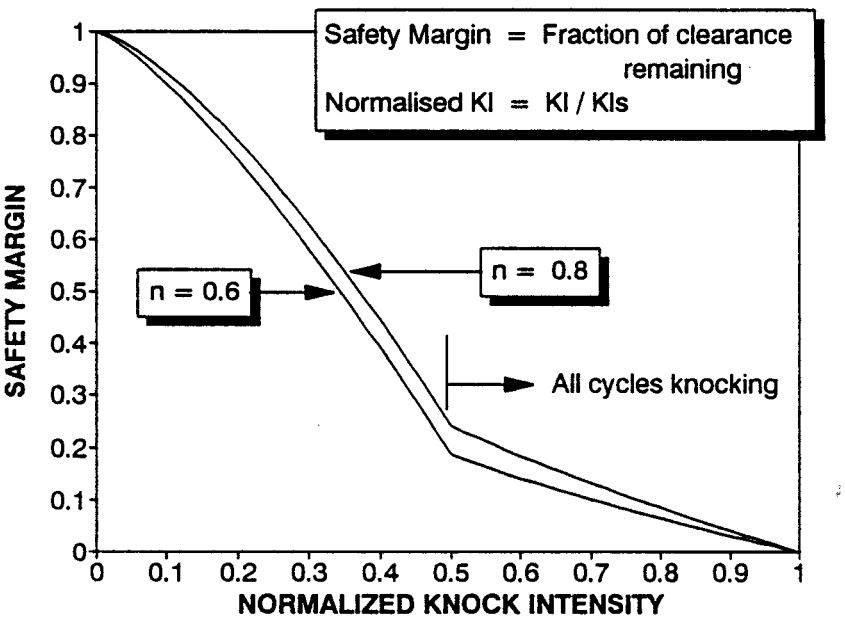

Figure 48: Safety margin as a function of knock intensity for assumed data

Using hypothetical data with these equations shows the relationship between the knock intensity and safety margin. To provide a general illustration, the knock intensity (*KI*) was

normalised relative to the knock intensity at seizure (KI_s). It was assumed for the purposes of this example that the knock intensity above which all cycles are knocking (KI_{100}) occurs at a lower value than the point of seizure.

Figure 48 shows the safety margin as a function of knock intensity. The two curves plotted represent the extremities of the exponent n in the model. From the figure, it is noted that the value of n has only a small effect on the estimated safety margin.

It is seen that in the region where all cycles are knocking, the remaining ring gap reduces at a considerably slower rate compared to the transition region.

CHAPTER 6

PATHWAYS TO KNOCK DAMAGE

Combining the results of chapters 3,4 and 5, it is now possible to construct the pathways by which engine failure may arise as a result of knock. This is summarised as a flow chart in figure 49.

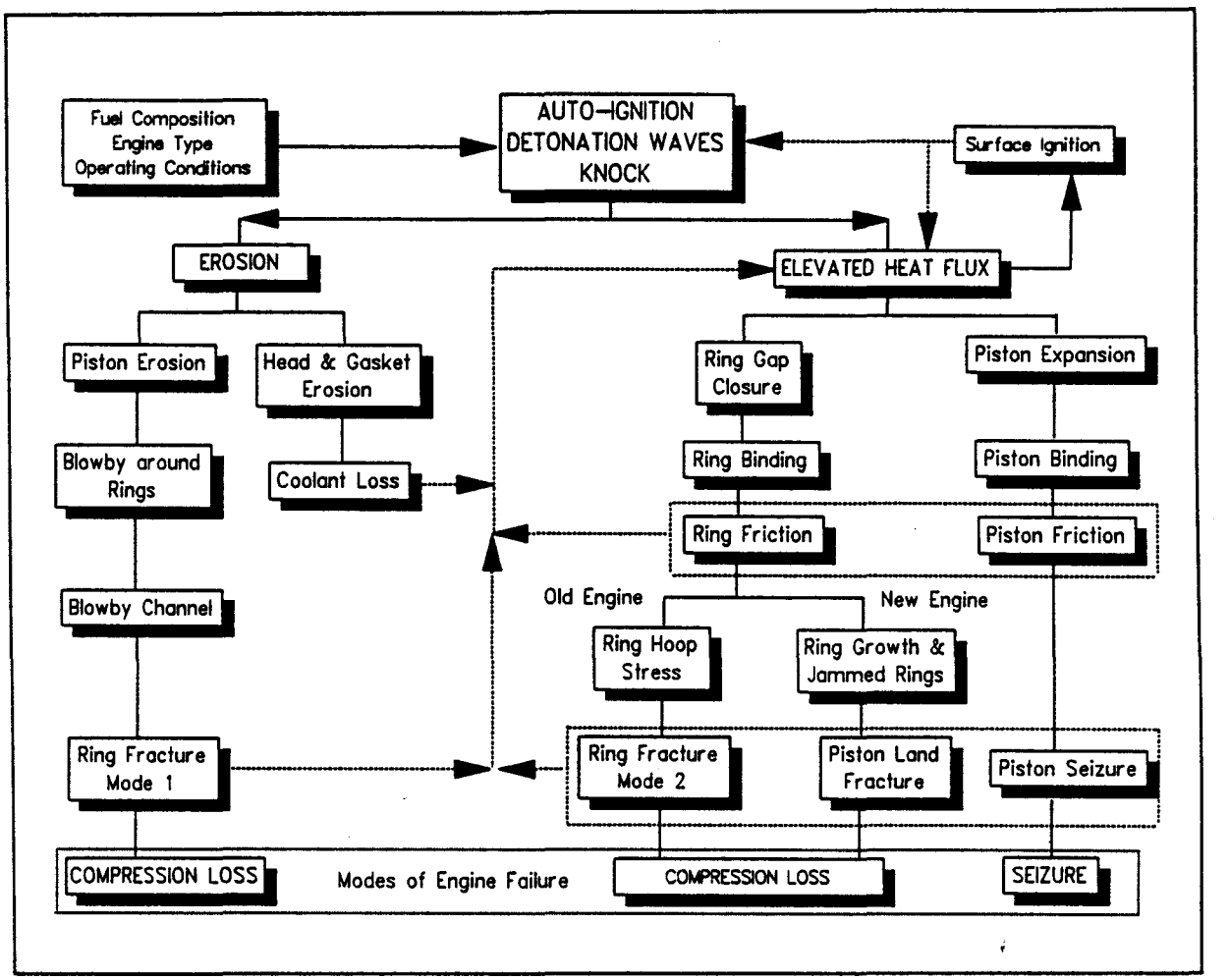

Figure 49: KNOCK DAMAGE PATHWAYS

Whether or not an engine will knock (ie: the propensity of the mixture to auto-ignite) is determined by the fuel properties, engine type and operating conditions, as described by conventional knock research. Under knocking conditions, the end-gas will auto-ignite producing a rapid energy release.

Following auto-ignition, the intensity of the subsequent developing detonation is a function of air-fuel properties and end-gas conditions. This is not the same relationship that governs the propensity of the mixture to auto-ignite. Furthermore, the ensuing shock waves have two distinctly different effects on the combustion chamber.

- Firstly, a localised effect in the end-gas region during the rapid energy release phase is able to cause erosion damage on the surrounding surfaces. The extent of this damage is determined by the properties of the shock waves together with the engine geometry in that region.

- Secondly, the shock waves cause a chamber resonance which effectively degrades the thermal boundary layer on the chamber surfaces. This is a global effect resulting in a bulk increase in heat flux to the piston, bore, rings and head.

These processes will produce two different pathways leading to damage. The particular path taken is a function of engine type and operating conditions.

6.1 EROSION PATHWAY

Depending on the physical geometry of the surfaces in the end-gas region, erosion may occur on the head, gasket and/or piston. If the head and gasket are attacked, a blow-by path to the coolant will eventually develop, leading to coolant loss and subsequent engine failure.

Continuous piston erosion eventually results in a blow-by path around the rings, resulting in compression loss and a significant increase in the heat flux to the piston. The compression loss is, in itself, an engine failure. If operation is continued with this blow-by, the piston lands would be burned and the blow-by channel enlarged until ring fracture results, due to lack of ring support (mode 1 in figure 49).

Blow-by could also lead to pre-ignition from the hot piston surfaces causing runaway failure.

6.2 HEAT FLUX PATHWAY

The increased heat flux resulting from chamber resonance (and blow-by if present) results in a general increase in surface temperatures. Depending on the relative tolerances of the piston/bore and ring gap, one of the following two damage paths exist:

- With a marginal piston/bore tolerance, the expansion of the piston under increased heat flux would cause a piston/bore partial seizure. The friction resulting from the seizure would further increase the heat flux to the piston assembly, and eventually lead to a complete piston seizure.

- If the ring gap is marginal, it will close due to the thermal expansion of the ring. At the point of ring closure, the ring will begin to seize in the bore, causing an additional increase in heat flux through friction. Further increases in ring temperature due to the partial seizure will result in severe hoop stresses being set up in the ring, aggravating the seizure and temperature. These extreme temperatures and stresses result in circumferential plastic yield of the ring material which has the effect of relieving the hoop stress but increasing the ring thickness. An increase in the ring thickness would result from the phase change in the material at these elevated temperatures.

In the case of a new engine, on cooling after this sequence of events, the increased ring thickness would produce severe bending stresses on the piston lands, jamming the rings in their grooves. Each time the engine is operated thereafter, the hot piston would release the rings from their grooves (due to the thermal expansion of piston material being greater than that of the ring). After use, on cooling, the rings will again be bound into their grooves, causing low-frequency fatigue which would eventually lead to piston land fracture and seizure as a result of the debris.

In an old engine, with worn ring grooves, there is space for the lateral ring expansion to occur and the high temperature yield would be expected to relieve the seizure. The ring may fractured during the high temperature hoop stress phase (mode 2 in figure 49), due to the

side clearance, which would cause bending and buckling to be added to the compressive stresses.

Increased heat flux may also produce surface ignition, further aggravating the knock intensity. Unless checked, this path would lead to pre-ignition runaway failure.

This chapter explains how damage results from knocking combustion. Apart from erosion damage, the other forms of knock damage have, previously, not been studied in detail.

CHAPTER 7

CONCLUSIONS AND RECOMMENDATIONS

The following conclusions are drawn from the work performed in this thesis:

7.1 GENERAL

- The mechanisms of knock-induced engine damage have been identified and quantified.

- Knock damage was found to be caused by two independent processes, namely, localized pressure-temperature transients resulting in surface erosion and elevated heat flux producing global piston and ring problems.

The following conclusions were drawn from the independent studies:

7.2 CONCLUSIONS FROM EROSION INVESTIGATION

- A detonation model was shown to be a useful means of predicting the effect of fuel and operating conditions on the propensity of knock to cause erosion damage.

- The inverse relationship between initial temperature and detonation pressure adds an independent explanation, besides geometric confinement, as to why the crevice regions are preferentially eroded.

- Thermal stresses contribute a major proportion of the surface loading during the erosion process. However, based on theoretical analysis, thermal stresses were shown to be relatively insensitive to operating conditions.

- It was deduced that the extent of surface erosion was controlled primarily by changes in the detonation pressure.

- The cylinder-pressure at the onset of knock was identified and correlated as a better indicator of erosion damage potential, compared to conventional knock intensity definitions.

- A criterion was established to determine the safety margin of knocking conditions, relative to the onset of erosion damage.

7.3 CONCLUSIONS FROM HEAT FLUX INVESTIGATION

- The ability of knock to cause ring seizure was demonstrated by direct measurement of the ring gap under knocking conditions.

- It was shown that with complete ring gap closure, the additional heat generated by seizure would cause the ring to plastically yield in the circumferential direction.

- The mechanism of rings jamming in their grooves and piston-land fracture were shown to be due to lateral growth of the rings at seizure temperatures, caused by spheroidization of flake graphite in the cast iron matrix.

- The maximum amplitude of pressure oscillations of knocking cycles was identified and correlated as being a strong indicator of the propensity of knock to cause global piston and ring problems.

- A criterion was established to determine the safety margin of knocking conditions with respect to the onset of piston or ring seizure.

7.4 RECOMMENDATIONS

The following recommendations are made for the purposes of extending this research:

- The theoretical analysis indicated that the thermal stresses due to knock are relatively insensitive to the operating conditions. This needs to be confirmed experimentally, by applying the thermal stress analysis to heat flux data, over a wide range of operating conditions.

- The rate of erosion-damage with respect to time should be researched. This would resolve the extent to which surface fatigue influences erosion damage, which was not addressed in this thesis.

- As discussed in Chapter 4, the effect of engine speed on erosion damage was not resolved by the theoretical and experimental analysis. With continued concerns over the damaging effects of high-speed knock, this effect needs to be researched.

- The design of the specimen shape and mounting, used in this thesis, was problematic. In some cases the specimen fractured, while in others, the chamber seal developed leaks. It is recommended that an alternate method of specimen mounting and sealing be developed. If possible, a smaller specimen should also be designed so that the mass-loss can be measured.

- Only a limited amount of ring gap data was measured from the engine tests, due to the difficulty of applying the mechanical scribe system. The development of an electronic ring gap transducer would provide on-line data and obviate the problems of piston removal between tests.

- An investigation is recommended to develop a ring material which is less prone to graphite spheroidization. This would limit the lateral growth of the rings and hence prevent the problems of rings jamming in ring-grooves and piston land cracking.

CHAPTER 8

REFERENCES

1. Clark, D., Trans. Faraday Soc., Vol 22, p.338, 1926.
2. Litzinger, T.A., "A review of experimental studies of knock chemistry in engines", Proc. Energy Comb. Sci., Vol.16, 1990.
3. Taylor, C.F., "The Internal Combustion Engine in Theory and Practice", Vol.2, The MIT Press, Massachusetts, 1980.
4. Heywood, J.B., "Internal Combustion Engine Fundamentals", McGraw-Hill Book Company, New York, 1988
5. Midgeley, T., "The Combustion of Fuels in Internal-combustion Engines", SAE Trans. 15, 659, 1920.
6. Westbrook, C.K., Warnatz, J. and Pitz, W., "A detailed chemical kinetic reaction mechanism ... and its applications to analysis of engine knock", 22nd Int. Symp. on Combustion, 893, The Combustion Institute, 1988.
7. Pitz, W., Westbrook, C.K. and Leppard, W.R., "Auto-ignition chemistry of n-butane in a motored engine: A comparison of experimental and modelled results", SAE Paper 881605, 1988.
8. Colins, D., "Gasoline combustion chambers", SAE Paper 830866, 1983.
9. Gatowski, J. and Heywood, J., "Faster burning in spark-ignition engines", Energy Lab Report, MIT, July-September 1985.
10. Yates, A. and Dutkiewicz, R.K., "Petrol Octane Requirements for South Africa", Report No. GEN 123, Energy Research Institute, January 1988.
11. ASTM, "Test methods for rating motor, diesel and aviation fuels", Annual Book of Standards, Vol.5.04, ASTM, 1988.
12. Betts, W.E., "Avoiding High Speed Knock Engine Failures", Int. Symp. on Knocking Combustion Engines, Wolfsburg, Nov 1981.
13. Betz, G. and Ellerman, J., "Knock-Related Piston Damage in Gasoline Engines, Knock Measurement Technique, Aspects of Knock Failure", Int. Symp. on Knocking Combustion Engines, Wolfsburg, Nov 1981.
14. Essig, G., "Piston Loading at Knocking Combustion (Detonation)", Int. Symp. on Knocking Combustion Engines, Wolfsburg, Nov 1981.

15. Davis, H.P., Uyehara, O.A. and Myers, P.S., "The Effects of Knock on the Hydrocarbon Emissions of a Spark-Ignition Engine", SAE Paper 690085, 1969.

16. Obert, E.F., "Internal combustion engines and air pollution", 3rd Ed., Harper & Row Publishers, N.Y., 1973.

17. Miller, C.D., "Roles of Detonation Waves and Auto-ignition in Spark-ignition Engines", SAE Trans., Vol.1, No.1, 1947, p98.

18. Robert Bosch GmbH, "Automotive Handbook", 32rd Ed., Robert Bosch Publishers, Stuttgart, 1993.

19. Yates, A.D.B., "Abnormal Combustion - Methanol versus Gasoline", PhD Thesis, University of Cape Town, August 1988.

20. Taylor, C.F. et al, "A New Instrument Devised for the Study of Combustion", SAE Journal, Vol.34, No.2, February 1934.

21. Chun, K.M. and Heywood, J.B., "Characterization of Knock in a Spark-ignition Engine", SAE Paper 890156, 1989.

22. Ricardo, H.R.,"The High-speed Internal-combustion Engine", 1st Ed., Blackie & Son Ltd., London, 1923.

23. Male, T., "Photographs at 500 000 frames per second of Combustion and Detonation in a Reciprocating Engine", 3rd Int Symp Combustion, 1949.

24. Franklin, M.L. and Murphy, T.E., "A Study of Knock and Power Loss in the Automotive Spark Ignition Engine", SAE Paper 890161, 1989.

25. Litzinger, T.A., "A review of experimental studies of knock chemistry in engines", Prog. Energy Combustion Sci., Vol.16, pp155-167, 1990.

26. Oppenheim, A.K., "The knock syndrome - Its cures and victims", SAE Paper 841339, 1984.

27. Goyal, G., Maas, U. and Warnatz, J., "Simulation of the transition from deflagration to detonation", SAE Paper 900026, 1990.

28. Abdel-Gayed, R.D., Bradley, D and Lung, F,K-K.,"Combustion regimes and the straining of turbulent flames", Combustion and Flames, 76, pp213-218, 1989.

29. Pan, J. and Sheppard, C.G.W., "A theoretical and experimental study of the modes of end-gas auto-ignition leading to knock in S.I. engines", SAE Paper 942060, 1994.

30. König, G. and Sheppard, C.G.W., "End-gas auto-ignition and knock in a spark-ignition engine", SAE Paper 902135, 1990.

31. König, G., et al, "Role of exothermic centers on knock initiation and knock damage",

SAE Paper 902136, 1990.

32. Klein, R., "Shock initiated ignition in an L-shaped Duct; Two aspects of its numerical simulation", Notes on Numerical Fluid Mechanics, Ed: M. Deville, Vieweg, 20, pp138-145, 1988.

33. Klein, R., "Detonation initiation due to shock wave-boundary interactions", Notes on Numerical Fluid Mechanics, Ed: J. Ballmann, R. Jeltsch, Vieweg, 24, pp279-288, 1988.

34. Maly, R.R., Klein, R., Peters, N. and König, G., "Theoretical and experimental investigation of knock induced surface destruction", SAE Paper 900025, 1990.

35. Griffiths, J.F. et al, "Application of CFD to the modelling of auto-ignition at high pressure in a cylinder", I.Mech.E., C448/030, 1992.

36. Schreiber, M. et al, "Spatial structure in end-gas auto-ignition", SAE Paper 932758, 1993.

37. Brussovansky, S., Heywood, J.B., and Keck, J.C., "Predicting the effects of air and coolant temperature, deposits, spark timing and speed on knock in spark-ignition engines", SAE Paper 922324, 1992.

38. Young, M.B., "Cyclic dispersion in the homogeneous-charge spark-ignition engine-A literature survey", SAE Paper 810020, 1981.

39. Hancock, M.S. et al, "The influence of arc parameters on combustion in a spark-ignition engine", SAE Paper 860321, 1986.

40. Hill, P.G., "Cyclic Variations and Turbulence Structure in Spark-ignition Engines", Combustion and Flame, Vol.72, 1988, p73.

41. Chun, K.M. and Heywood, J.B., "Characterization of Knock in a Spark-ignition Engine", SAE Paper 890156, 1989.

42. Leppard, W.R., "Individual-cylinder knock occurence and intensity in multicylinder engines", SAE Paper 820074, 1982.

43. Haghgooie, M., "Effects of fuel octane number and inlet air temperature on knock characteristics of a single-cylinder engine", SAE Paper 902134, 1990.

44. Renault, F., "A New Technique to Detect and Control Knock Damage", SAE Paper 820073, 1982.

45. Lee, W. and Schaefer, H.J., "Analysis of Local Pressures, Surface Temperatures and Engine Damages under Knocking Conditions", SAE Paper 830508, 1983.

46. Maly, R. and Ziegler, G., "Thermal Combustion Modelling - Theoretical and Experimental Investigation of the Knocking Process", SAE Paper 820759, 1982.

47. Boehm, G. and Harrer, J., "Nickel coated pistons for improved durability in knock control engines", SAE Paper 900453, 1990.

48. French, C.C. and Atkins, K.A., "Thermal Loading of a Petrol Engine", Proc. of IMechE, Vol.187, No.49/73, 1973.

49. Casci, C. and Ferrari, G., "Analisi del carico termico dello startuffo in condizioni di detonazione", ATA, January 1971.

50. Zhao, H., Collings, N. and Ma, T., "Characterization of knock and its effect on surface temperatures", SAE Paper 920514, 1992.

51. Lu, J.-H., Ezekoye, D., Iiyama, A., Greif, R. and Sawyer, R.F., "Effect of knock on time-resolved engine heat transfer", SAE Paper 890158, 1989.

52. Hickling, R., Chen, F.H.K. and Feldmaier, D.A., "Pressure pulsations in engine cylinders", GM Symp. on Engine Noise, Excitation, Vibration and Radiation, Plennum Press pp3 to 33, 1982.

53. Stone, R., "Introduction to Internal Combustion Engines", MacMillan Pub.Ltd, 1985.

54. Bogen, J.S. and Faust, W.J., "Aircraft Detonation Indicators", SAE Quarterly Trans., Vol.1, No.3, July 1947.

55. Bennett, K.F., Priede, T. and Yates, A.D.B., "An Accoustic Technique to Determine the Ignition Quality of Spark and Compression Ignition of Fuels", National Energy Council, File No. EVB 11, May 1986.

56. ASTM, "ASTM Manual of Engine Test Methods for rating Fuels", ASTM, Philadelphia, March 1948.

57. Huang, J.C. and Borman, G.L., "Measurements of Instantaneous Heat Flux to Metal and Ceramic Surfaces in a Diesel Engine", SAE Paper 870155, 1987.

58. Williams, D. and Dale, D.L., "Recent Trends in Knock Rating Methods and Engine Damage Tests", Int. Symp. on Knocking Combustion Engines, Wolfsburg, Nov 1981.

59. Klimstra, J., "The Knock Severity Index - A Proposal for a Knock Classification Method", SAE Paper 841335, 1984.

60. Robert Bosch GmbH, "Automotive Electric/Electronic Systems", Robert Bosch Publishers, Stuttgart, 1988.

61. Nakagawa, Y. et al, "Laser Shadowgraphic Analysis of Knocking in SI Engine", SAE

Paper 845001, 1984.

62. Horowitz, P. and Hill, W., "The Art of Electronics", Cambridge University Press, Cambridge, 1981.

63. Najt, P.M., "Evaluating Threshold Knock with a Semi- empirical Model- Initial Results", SAE Paper 872149, 1987.

64. Shigley, J.E., "Mechanical Engineering Design", 1st Metric Edition, McGraw-Hill, New York, 1986, p275.

65. Nates, R.J. and Yates, A.D.B., "Knock Damage Mechanisms in Spark-Ignition Engines", SAE Paper 942064, 1994.

66. Saika, T. and Korematsu, K., "Flame propogation into the ring crevice of a spark-ignition engine", SAE Paper 861528, 1986.

67. Lewis, B. and Von Elbe, G., "Combustion, Flames and Explosions of Gases", 3rd Ed., Academic Press, 1987.

68. Dixon, H.B., Phil. Trans. Royal Society, A184, 1903.

69. Bone, W.A. and Townend, D.T.A., "Flame and Combustion in Gases", Longmans, London, 1927.

70. Layffitte, P., "Science of Petroleum", Vol.4, Oxford University Press, London, 1938.

71. Glassman, I., "Combustion", Academic Press, London, 1977.

72. Moran, D.P. and Yates A.D.B., "The effects of evaporative cooling on engine knock", Technical Report for SASTECH (Pty) Ltd., Dept of Mech Eng, University of Cape Town, June 1993.

73. Timoshenko, S.P., "Theory of Elasticity", McGraw-Hill, 3rd Ed., New York, 1970.

74. Smithells Metal Reference Book, 6th Ed., Edited by Brandes, E.A., Butterworths, 1983.

75. Taylor, C.F. and Toong, T.Y., "Heat transfer in internal combustion engines", ASME Paper 57-HT-17, 1957.

76. Ferguson, C.R., "Internal Combustion Engines - Applied Thermosciences", John Wiley & Sons, New York, 1986, pp340.

77. Woschni, G., "A universally applicable equation for instantaneous heat transfer coefficient in internal combustion engines", SAE Paper 670931, 1967.

78. Fitton, J.C. and Nates, R.J., "Investigation into the relationship between knock intensity and piston seizure", Journal of (SA)IMechE, Vol. 8, No. 2, July 1992.

79. Angus, H.T., "CAST IRON: Physical and Engineering Properties", Butterworths, London, 1978.

80. Bamber, A., "Piston ring seizure", Mech Eng Project No. 19/93, Dept of Mech Eng, University of Cape Town, 1993.

81. Calcutt, B., Peruch O. and Vosloo, M., "Auto Data Digest", Goldfields Press Pty (Ltd), 1991.

82. Chapman, D.L., Phil. Mag., [5] 47, 1899.

83. Jouguet, E., "Mecanique des explosifs", J. Mathematique, p.347, 1905.

84. Becker, R., Z. Physik 8, 321, 1922.

85. Benson, R.S., "Advanced Engineering Thermodynamics", 2nd Ed., Pergamon Press, Oxford, 1977.

86. Janna, W.S., "Engineering Heat Transfer", SI Ed., Van Nostrand Reinhold, London, 1988.

87. Hearn, E.J., "Mechanics of materials, Vol 2", 2nd Ed., Pergamon Press, Oxford, 1985.

88. Jones, N., "Structural Impact", Cambridge University Press, Cambridge, 1989.

89. Fitton, J.C., "Investigation into the relationship between heat flux and thermal expansion of piston rings", Mech Eng Project No. 9/91, Dept of Mech Eng, University of Cape Town, 1991.

90. Jastrzebski, D., "Nature and Properties of Engineering Materials", John Wiley & Sons, Inc., 1969, pp153.

APPENDIX A: SPECIMEN DATA SHEETS

This appendix contains the data sheets for the selected knock-damaged piston collection discussed in chapter 3.

PISTON No: 4/91 (Specimen #1)

Engine . . . . . 4-cylinder, 1.8 litre, 4-stroke, Fiat

Vehicle . . . . . Fiat

Material . . . . . aluminium alloy

HISTORY:

Age of engine . . . . . about 90 000km

State of tuning . . . . poor

Fuel type . . . . . 97 RON

Altitude . . . . . sea level

Additional details . . . engine was using oil prior to failure, probably from worn valve guides

Operator report . . . Engine was knocking in low gear up inclines (full load) for at least two months prior to failure. Sudden misfire was noticed together with a large amount of black smoke from exhaust

OBSERVATIONS:

Erosion:

Piston crown . . . . . deposit removed and surface polished in a crescent shaped region around the inlet valve.

1st Land . . . . . surface polished below crescent region on crown

1st Ring groove . . . . N/A

Other . . . . . N/A

Surface texture . . . . polished

Blow-by channel . . . no

Lands cracked . . . . no

Rings jammed . . . . no

Rings broken . . . . . no of one another

Deposits . . . . . heavy carbon deposit (about 1mm thick) over crown, except in polished, crescent shaped region under inlet valve

Skirt seizure . . . . . no

Additional . . . . . oil ring broken

PISTON No: 5/92 (Specimen #2)

Engine . . . . . single-cylinder, 125cc, 2-stroke, Yamaha

Vehicle . . . . . Yamaha DT125 motorcycle

Material . . . . . aluminium alloy

HISTORY:

Age of engine . . . . . new piston, about 4 hours usage

State of tuning . . . . tuned for racing

Fuel type . . . . . high octane racing fuel

Altitude . . . . . sea level

Additional details . . . N/A

Operator report . . . engine knocking during race, overhaul after race.

OBSERVATIONS:

Erosion:

Piston crown . . . . . light erosion on edge of crown, all round circumference

1st Land . . . . . light erosion all around circumference on upper edge of 1st land, and in the region of the exhaust port erosion was seen to progress downwards towards the ring.

1st Ring groove . . . . no

Other . . . . . no

Surface texture . . . . pitted

Blow-by channel . . . no

Lands cracked . . . . no

Rings jammed . . . . compression ring jammed in groove

Rings broken . . . . . no

Deposits . . . . . no

Skirt seizure . . . . . no

Additional . . . . . N/A

PISTON No: 9/92 (Specimen #3)

Engine . . . . . 4-cylinder, 1.8 litre, 4-stroke, Volkswagen

Vehicle . . . . . VW Combi

Material . . . . . aluminium alloy

HISTORY:

Age of engine 60 000km

State of tuning . . . . good

Fuel type . . . . . contaminated gasoline with significantly reduced octane

Altitude . . . . . sea level

Additional details . . . N/A

Operator report . . . damage occurred at high speed on long incline, engine was knocking at the time of failure

OBSERVATIONS:

Erosion:

Piston crown . . . . . heavy erosion at edge of crown over 1/8 circumference

1st Land . . . . . heavy erosion with cavities above 1st ring over 1/6 circumference

1st Ring groove . . . . 2 cavities eroded in ring groove

Other . . . . . light erosion on 2nd and 3rd lands below 1st land zone

Surface texture . . . . pitted

Blow-by channel . . . no

Lands cracked . . . . 2 vertical cracks in the 2nd land, one in the centre of the erosion zone, the other at about 20mm from the erosion zone

Rings jammed . . . . both compression rings jammed in grooves

Rings broken . . . . . no

Deposits . . . . . no

Skirt seizure . . . . . light scuffing below 2nd crack in piston land

Additional . . . . . no

PISTON No: 7/92 (Specimen #4)

Engine . . . . . 4-cylinder, 1.6 litre, 4-stroke, Ford

Vehicle . . . . . Ford Escort

Material . . . . . aluminium alloy

HISTORY:

Age of engine 60 000km

State of tuning . . . . poor, timing over advanced

Fuel type . . . . . 97 RON

Altitude . . . . . sea level

Additional details . . . N/A

Operator report . . . during long trip knock was noticed, but ignored, eventually sudden power loss caused the operator to halt the vehicle to be stopped and towed in for repairs

OBSERVATIONS:

Erosion:

Piston crown . . . . . no

1st Land . . . . . small region showing heavy erosion, with a cavity formed above the 1st ring

1st Ring groove . . . . heavy erosion below the 1st land erosion site

Other . . . . . 2nd land and 2nd ring groove also eroded. ring gap coincides with the erosion site

Surface texture . . . . pitted at edges of erosion site, molten surface at centre of site

Blow-by channel . . . blow-by channel under 1st ring

Lands cracked . . . . no

Rings jammed . . . . both compression rings jammed in grooves

Rings broken . . . . . no

Deposits . . . . . no

Skirt seizure . . . . . medium to heavy scuffing all around the piston

Additional . . . . . no

PISTON No: 1/92 (Specimen #5)

Engine . . . . . 4-cylinder, 1.6 litre, 4-stroke, Ford

Vehicle . . . . . Ford Escort

Material . . . . . aluminium alloy

HISTORY:

Age of engine . . . . . about 70 000km

State of tuning . . . . good, except for radiator leak

Fuel type . . . . . 97 RON

Altitude . . . . . sea level

Additional details . . . N/A

Operator report . . . knocking engine started to overheat on long uphill climb, followed by progressively heavier knock, finally misfire, at which time the vehicle was stopped

OBSERVATIONS:

Erosion:

Piston crown . . . . . Heavy erosion at edge of crown over 1/4 of circumference

1st Land . . . . . heavy erosion

1st Ring groove . . . . heavy erosion

Other . . . . . heavy erosion all the way under the 2nd compression ring. When looking at the side of the piston, the shape of the eroded region was that of an inverted triangle, with apex at the bottom (around the oil ring).

Surface texture . . . . pitted at the sides of damaged region and molten in the centre of the blow-by channel

Blow-by channel . . . large channel under the rings

Lands cracked . . . . no

Rings jammed . . . . both compression rings jammed in their grooves

Rings broken . . . . . 2nd compression ring and oil ring broken in the blow-by channel

Deposits . . . . . no

Skirt seizure . . . . . heavily scuffed skirt at ends of gudgeon pin

Additional . . . . . no

APPENDIX B: DETONATION MODEL

The aim of this work was to develop a computer code to predict the characteristics of a detonation wave based on the initial conditions and gas composition.

The approach adopted was somewhat simpler than existing models which include chemical-hydrodynamic coupling. These programs include the chemical kinetics driving the detonation wave and they yield discrepancies of less than 2% compared to experimental data. However, the objectives of this work were to evaluate relative and not absolute relationships. A computer model was developed from an analytical solution which had been shown to be accurate to within 10% of measured values [67]. This approach assumes instantaneous release of chemical energy in the wave front itself. The solution was founded on the original work of Chapman [82], Jouguet [83] and Becker [84], and was further developed by Lewis and Von Elbe [67] and Glassman [71].

The primary goal of this analysis was to predict and understand the effects of initial conditions on the post detonation characteristics.

Nomenclature:

C_p	-	specific heat (constant pressure)	[J/kg.K]
C_v	-	specific heat (constant volume)	[J/kg.K]
p	-	pressure	[Pa]
q	-	heat release	[J/kg]
R	-	gas constant	[J/kg.K]
R_u	-	universal gas constant	[J/mole.K]
T	-	temperature	[K]
u	-	velocity	[m/s]
γ	-	ratio of specific heats	
ϕ	-	fuel-air equivalence ratio	
ρ	-	density	[kg/m^3]

Subscripts:

1	-	initial conditions (reactants)
2	-	detonation conditions (products)

Consider a detonation wave travelling from left to right at velocity u_1 through a stagnant unburned gas mixture. The velocity of the burned gas relative to the wave is u_2 as shown in figure B1.

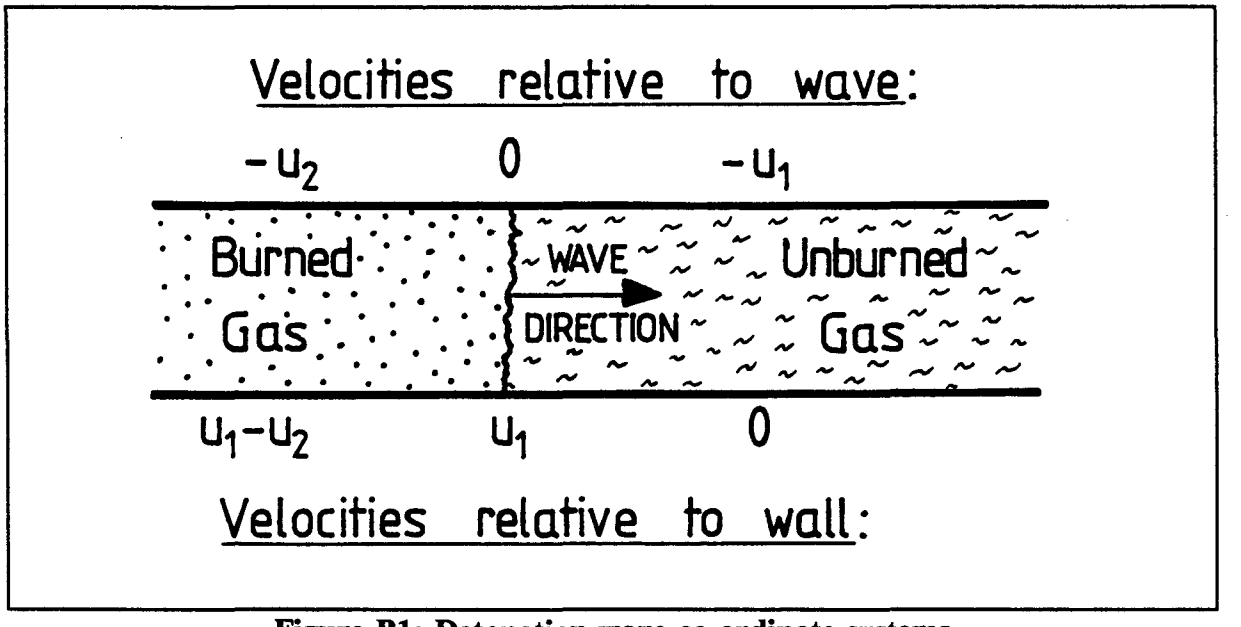

Figure B1: Detonation wave co-ordinate systems

$\Delta u = u_1 - u_2$ is the burned gas velocity relative to the wall.

Taking velocities relative to the wave, the conservation and equations of state are:

Mass: $$\rho_1 u_1 = \rho_2 u_2 \quad (1)$$

Momentum: $$p_1 + \rho_1 u_1^2 = p_2 + \rho_2 u_2^2 \quad (2)$$

Energy: $$C_p T_1 + \tfrac{1}{2} u_1^2 + q = C_p T_2 + \tfrac{1}{2} u_2^2 \quad (3)$$

State: $$p_1 = \rho_1 R_1 T_1$$
$$p_2 = \rho_2 R_2 T_2 \quad (4)$$

Assumptions made are:

1. Ideal gas equation of state.
2. Specific heats are a function of temperature.

Thus the unknowns are: u_1 ; u_2 ; ρ_2 ; T_2 and p_2

As there are only 4 equations, but 5 unknowns, an eigenvalue solution cannot be obtained. Experimentally it has been shown that the detonation velocity is uniquely constant for given initial conditions.

Lewis and Von Elbe [67] used the conditions of minimum entropy and strong detonation wave ($p_2 \gg p_1$) to produce an additional relationship. In conjunction with the 4 equations above, the following 5 relationships are presented by Glassman [71] to solve for the unique strong detonation condition, known as the Chapman-Jouguet result.

For convenience: $$\mu \equiv \frac{\rho_1}{\rho_2}$$

$$\mu^2 - \mu\left[\left(\frac{1}{\gamma_2}\right) + 1 - \left(\frac{R_1 T_1}{R_2 T_2}\right)\right] - \left(\frac{R_1 T_1}{R_2 T_2}\right) = 0 \qquad (5)$$

$$p_2 = p_1 \mu \left(\frac{R_2 T_2}{R_1 T_1}\right) \qquad (6)$$

$$n_2 E_2 - E_1 = \frac{1}{2} n_2 R_u \left(\frac{T_2}{\gamma_2}\right) \qquad (7)$$

$$u_1 = \mu \sqrt{\gamma_2 R_2 T_2} \qquad (8)$$

$$\Delta u = u_1 - \sqrt{\gamma_2 R_2 T_2} \qquad (9)$$

where: E - Total internal energy (ie the sum of the component internal energies)

and $n_2 = MW_1 / MW2$ MW is the Mean Molar Mass

To solve these equations (5 to 9) the following procedure was used. A value of T_2 was assumed and estimates of γ_2 and MW_2 were made (both being relatively insensitive to temperature).

The quadratic equation (5) was solved as follows:

$$\mu = \frac{1}{2}\left[\frac{1}{\gamma_2} + 1 - \frac{R_1 T_1}{R_2 T_2}\right] + \frac{1}{2}\sqrt{\left(\frac{1}{\gamma} + 1 - \frac{R_1 T_1}{R_2 T_2}\right)^2 + 4\left(\frac{R_1 T_1}{R_2 T_2}\right)} \qquad (10)$$

The detonation pressure was calculated using equation (6) and the assumed value of T_2 was checked with equation (7). However to do so, the equilibrium composition of the burned gas had to be determined so as to calculate the total internal energy of the reactants and products (E_1 and E_2).

The chemical balance describing this combustion process for a hydrocarbon (C_nH_m) is as follows (alcohols may be treated by using $C_n H_m O_p$ as the fuel molecule):

$$C_m H_m + \left(n+\frac{m}{4}\right)\frac{1}{\phi} O_2 + 3.76\left(n+\frac{m}{4}\right)\frac{1}{\phi} N_2$$

$$\rightarrow a_1 CO_2 + a_2 CO + a_3 H_2O + a_4 H_2 + a_5 O_2 + a_6 N_2 \qquad (11)$$

For the detonation chamber simulations, where a mixture of ethylene and oxygen was used, the nitrogen (N_2) coefficient was omitted from the analysis.

In order to determine the internal energy of the products, it was necessary to solve for the coefficients a_1; a_2; ...; a_6.

The following two dissociation reactions are the most dominant in the temperature range to be modelled [85]:

$$CO + H_2O \rightleftharpoons CO_2 + H_2 \tag{12}$$

$$CO + \frac{1}{2}O_2 \rightleftharpoons CO_2 \tag{13}$$

These are governed by the equilibrium constant K_{p1} and K_{p2} respectively, which are functions of temperature. Equilibrium compositions of CO, CO_2, H_2 and O_2 are described by:

$$K_{p_1} = \frac{a_1 a_4}{a_2 a_3} \tag{14}$$

$$\frac{p_2}{M_p} K_{p_2}{}^2 = \left(\frac{a_1}{a_2}\right)^2 \frac{1}{a_5} \tag{15}$$

where M_p is the total moles of product per mole of fuel.

Applying a mass balance to the overall reaction (11):

Carbon: $$n = a_1 + a_2 \tag{16}$$

Hydrogen: $$\frac{m}{3} = a_3 + a_4 \tag{17}$$

Oxygen: $$2\left(n+\frac{m}{4}\right)\frac{1}{\phi} = 2a_1 + a_2 + a_3 + 2a_5 \tag{18}$$

Equations 14, 15, 16, 17 and 18 were combined to solve for the 5 unknown coefficients (a_1; a_2; ... a_5). This combination produces a quartic function of the coefficient a_1:

$$f(a) = (a - B) - \frac{m}{2}\left[\frac{n-a}{n-Ca}\right] + \frac{2}{D}\left(\frac{a}{n-a}\right)^2 = 0 \qquad (19)$$

where:

$$a = a_1$$

$$A = \frac{p_2}{M_p}$$

$$B = \frac{2}{\phi}\left(n + \frac{m}{4}\right) - \left(n + \frac{m}{2}\right)$$

$$C = \frac{1}{K_{p_1}} - 1$$

$$D = AK_{p_2}{}^2$$

Solving for "a" in the quartic equation (19), then:

$$a_1 = a$$

$$a_2 = n - a$$

$$a_5 = \left(\frac{a_1}{a_2}\right)^2 \frac{1}{D}$$

$$a_4 = a_1 + 2a_5 - B$$

$$a_3 = \frac{m}{2} - a_4$$

$$a_6 = \frac{3.76}{\phi}\left(n + \frac{m}{4}\right)$$

Having determined the burned gas composition, the accuracy of the assumed wave temperature (T_2) was checked using equation (7) which had been rearranged as follows:

$$f(E) = n_2 E_2 - E_1 - \frac{1}{2} n_2 R_u \left(\frac{T_2}{\gamma_2} \right) = 0$$

The total internal energy of the reactants and products at their appropriate temperatures are determined as follows [85]:

$$E = \sum_{i=1}^{7} a_i \left[e_i^o + e_i(T) \right]$$

where
- i - component
- a_i - moles of component
- e_i^o - component internal energy of formation (J/mole)
- $e_i(T)$ - component internal energy which is a function of temperature (J/mole)

A Newton-Raphson iteration of equation (20) produces a new estimate of T_2.

$$[T_2]_N = [T_2]_{N-1} - \frac{f(E)_{N-1}}{\left(n_2 M_p C_v(T_2) - \frac{1}{2} n_2 \frac{R_u}{\phi} \right)}$$

This iteration was performed until the error between $[T_2]_N$ and $[T_2]_{N-1}$ was less than 0.5K. At this point, the remaining two unknowns u_1 and Δu were determined from equations (8) and (9) respectively.

The detonation wave static pressure calculated was converted stagnation (total) pressure. This was done to describe the intensity of the wave impact on a solid surface, which is a combination of the static pressure and the burnt gas momentum transfer to the walls. The isentropic expression for the ratio of stagnation (p_0) to static (p) pressure was used with Mach number (M) and specific heat ratio (γ) calculated at burnt gas conditions, as follows:

$$\frac{p_0}{p} = \left[1 + \left(\frac{\gamma - 1}{2}\right)M^2\right]^{\frac{\gamma}{\gamma-1}}$$

Throughout this work, unless otherwise stated, the term "detonation pressure" refers to the stagnation pressure of the wave.

Enthalpy (h), internal energy (e), specific heat (C_v) and equilibrium constants (K_p) as a function of temperature were calculated using 5th order polynomial for the enthalpy. These algorithms were developed by Benson [85]. The subscript (i) was used to denote the particular species as follows:

Species:	CO_2	CO	H_2O	H_2	O_2	N_2	C_8H_{18}	Methanol	Ethanol
Subscript: (i)	1	2	3	4	5	6	7	8	9

Each species (i) has 7 coefficients denoted by the subscript (j), such that j = 1, 2, ...7. Thus, a 9 x 7 matrix was used in the code for all these coefficients ($C_{i,j}$). The properties of each species as a function of temperature were derived from the algorithm defining enthalpy, as follows:

$$h_i(T) \equiv R_u\left(\sum_{j=1}^{5} C_{i,j}T^j\right) + C_{i,7} \qquad (J/mol)$$

and $$e_i(T) = h_i(T) - R_uT$$

$$\therefore \quad e_i(T) = R_u\left[\left(\sum_{j=1}^{5} C_{i,j}T^j\right) - T\right] + C_{i,7} \qquad (J/mol)$$

and $$C_{v_i}(T) \equiv \left[\frac{\partial e_i(T)}{\partial T}\right]_v$$

$$\therefore \quad C_{v_i}(T) = R_u\left[\left(\sum_{j=1}^{5} j\,C_{i,j}T^{j-1}\right) - 1\right] \qquad (J/mol.K)$$

To determine the two equilibrium constants, an intermediate function *V(T)* was evaluated:

$$V_i(T) = \sum_{j=2}^{5} \left(\frac{C_{i,j}}{j-1} \right) T^{j-1}$$

Using this function, the equilibrium constants were determined as follows:

$$\ln(K_{p_1}) = [\, C_{2,1} + C_{3,1} - C_{4,1} - C_{1,1} \,](1 - \ln T)$$

$$- [V_2(T) + V_3(T) - V_4(T) - V_1(T)]$$

$$- [C_{2,6} + C_{3,6} - C_{4,6} - C_{1,6} \,] + \frac{0.4047\ 10^8}{R_u\ T}$$

$$\ln(K_{p_2}) = [C_{2,1} + 0.5 C_{5,1} - C_{1,1}](1 - \ln T)$$

$$- [V_2(T) + 0.5 V_5(T) - V_1(T)]$$

$$- [C_{2,6} + 0.5 C_{5,6} - C_{1,6}] + \frac{2.707\ 10^8}{R_u\ T}$$

The BASIC computer code developed for this simulation is presented in Appendix I. The input into the program included all initial conditions, as follows:

Input: Pressure (p_1), Temperature (T_1), Equivalence ratio (ϕ) and Fuel Type ($C_n H_m O_p$)

The code included thermodynamic data for the following types of fuels:

N-Octane, Methanol, Ethanol and Ethylene

When simulating ethylene, the code was modified to use only oxygen as the oxidant, to conform to the detonation chamber tests.

The output produced from the simulation included the following detonation wave characteristics:

Output: Pressure (p_2, p_{02}), Temperature (T_2), Wave Velocity (U_1) and Particle Velocity (Δu)

Lewis and Von Elbe [67] presented data from three separate sources [68,69,70], each reporting measured detonation velocities for ethylene-oxygen mixtures. These data were used to check the accuracy of the model, which was given the identical initial conditions as the test data. Figure B2 shows the fit of this data to the theoretical model, which served to confirm the general accuracy of the model.

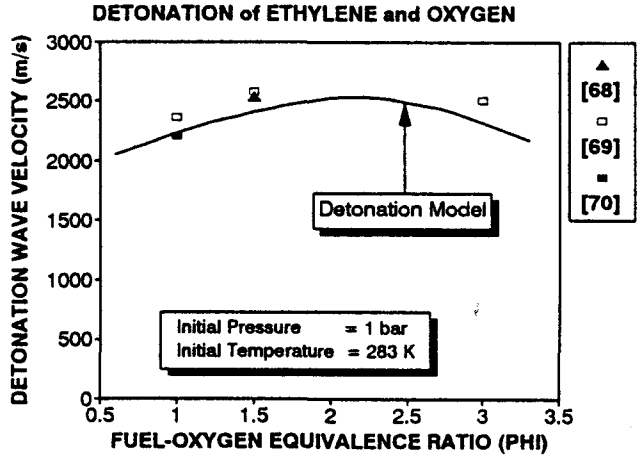

Figure B2: Theoretical and Experimental Data

The following graphs illustrate simulations, showing detonation characteristics as a function of equivalence ratio and fuel type.

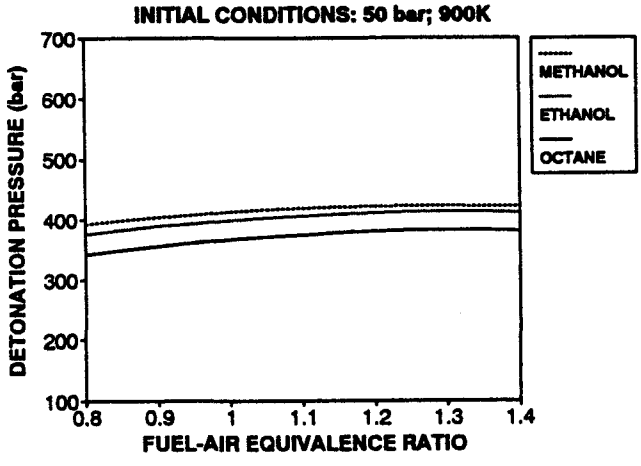

Figure B3: Detonation Pressure vs Equivalence Ratio

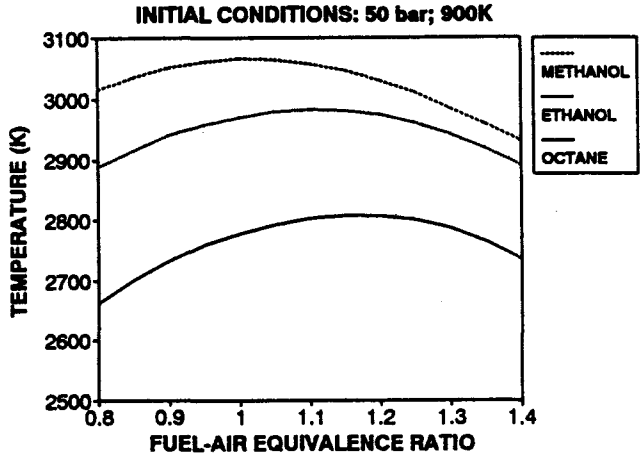

Figure B4: Detonation Temperature vs Equivalence Ratio

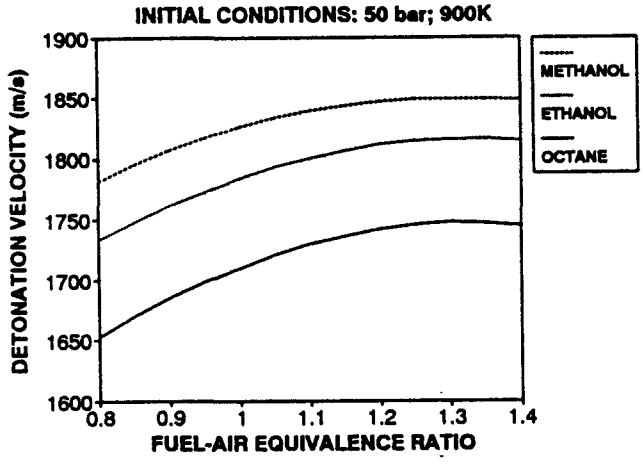

Figure B5: Wave Velocity vs Equivalence Ratio

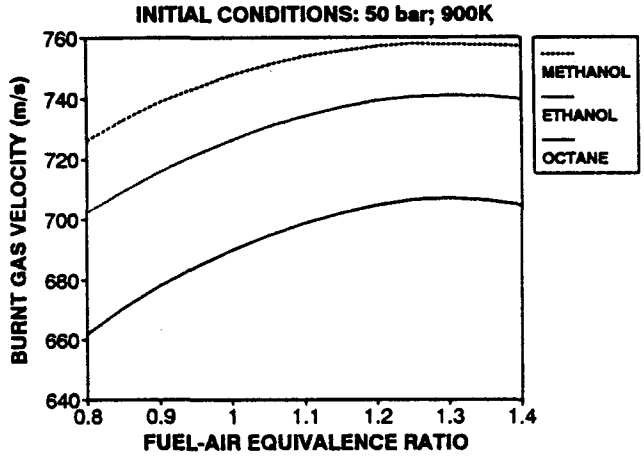

Figure B6: Burnt Gas Velocity vs Equivalence Ratio

Figures B3 to B6 show the detonation wave characteristics as a function of mixture strength for three different fuels under identical initial conditions.

Figure B7 illustrates the contribution of the burned gas velocity towards the stagnation (total) pressure. The dynamic pressure constitutes nearly 25% of the total pressure in these shock waves.

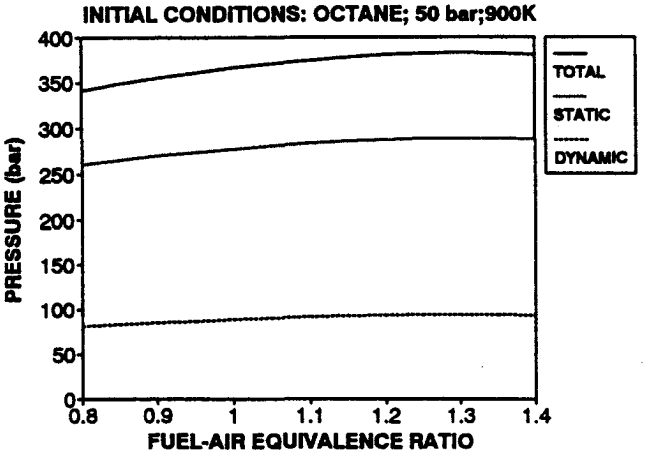

Figure B7: Pressure vs Equivalence Ratio

Simulations were run to assess the effects of the other initial conditions. For the remainder of this section, effects on the detonation pressure will be evaluated, as it is primarily this parameter that is thought to be responsible for erosion damage. Eitherway, the detonation temperature generally follows the pressure trends, as illustrated in figures B3 and B4. Figures B8 and B9 show the effects of initial pressure on detonation pressure.

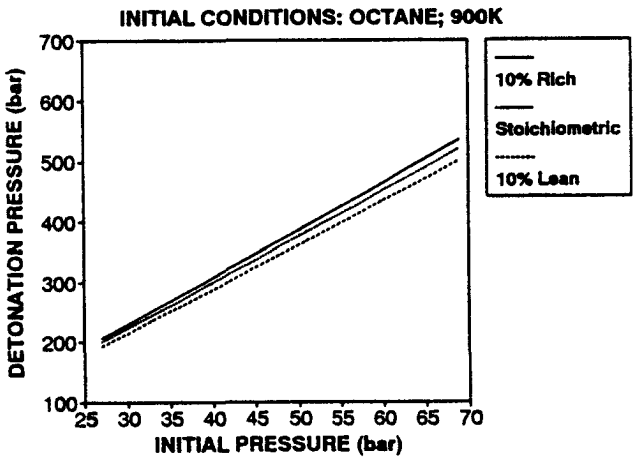

Figure B8: Detonation Pressure vs Initial Pressure and Mixture

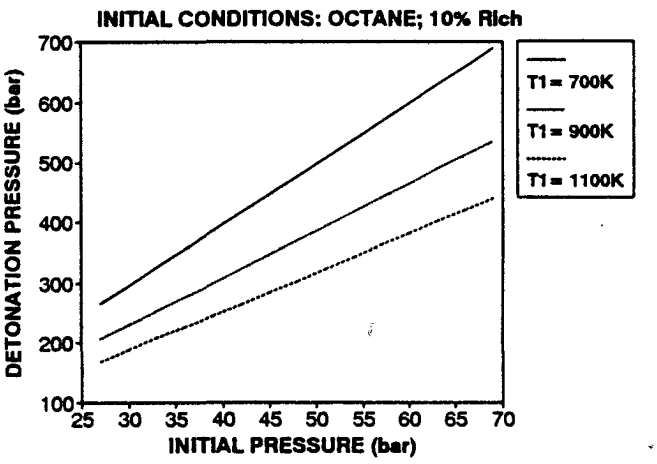

Figure B9: Detonation Pressure vs Initial Pressure and Temperature

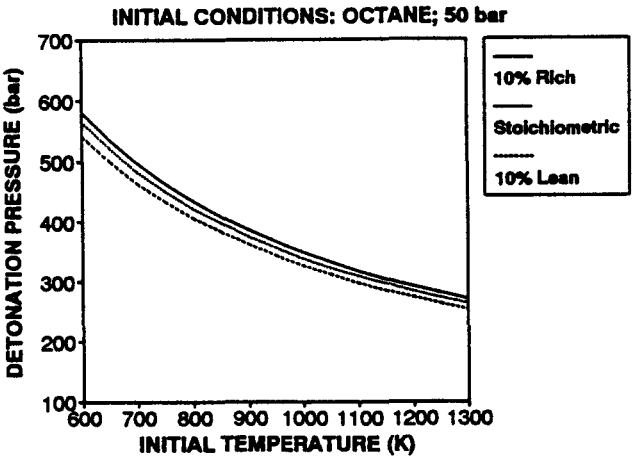

Figure B10: Detonation Pressure vs Initial Temperature and Mixture

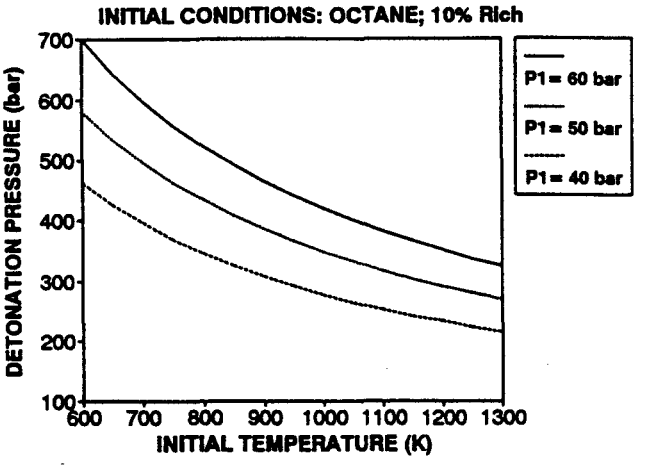

Figure B11: Detonation Pressure vs Initial Temperature and Pressure

Figures B10 and B11 show the results of simulations run with initial temperature as the independent variable. From all these simulations, it is evident that the general effect of initial conditions on detonation intensity is easily understood by their effect on the initial gas density.

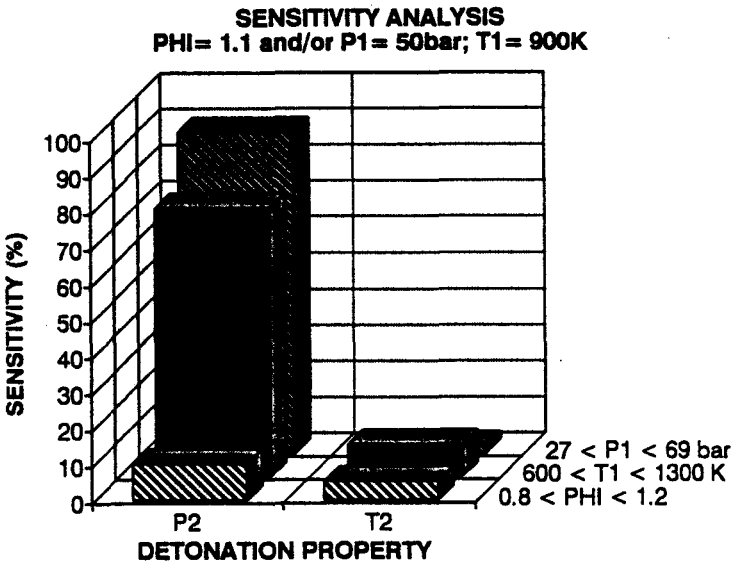

Figure B12: Sensitivity Analysis

A sensitivity analysis of all this data was undertaken to check the dominance of these initial conditions on both the detonation pressure (p_2) and temperature (T_2). The sensitivity of the dependent variables (p_2 and T_2) was calculated as their maximum (percentage) change relative

to their mean, for each range of the independent variables (p_1, T_1 and ϕ). In each case, two independent variables were held constant. Figure B12 illustrates the results of this analysis. The results of the detonation pressure sensitivity confirm that this parameter is very sensitive to initial pressures and temperatures, but relatively insensitive to mixture strength. Conversely, the detonation wave temperature is seen to be relatively insensitive to all the independent variables.

The initial pressure and temperature referred to in these graphs corresponds in an engine to the end-gas condition at which knock occurs. This condition is established by the following:

- **Pressure-Temperature History** during inlet, compression and combustion and is influenced by local heat transfer.
- **Knock Resistance** of the fuel will determine the extent of polytropic compression the mixture can withstand prior to auto-ignition.

From these results it is apparent that the initial pressures and temperatures have significant, but opposing effects on the intensity of detonation and therefore it was imperative to ascertain which of these effects is more dominant. A method of examination is to investigate the effect of compression ratio on detonation conditions.

The relationship between temperature and pressure in the end-gas may be described by a polytropic compression process, with an appropriate choice of polytropic exponent. At a compression ratio of 8:1, an end-gas condition at the onset of knock was chosen as 900K and 40 bar. By assuming that the extent of flame compression is relatively unchanged, the end-gas conditions at other compression ratios were calculated using the polytropic compression relationship.

$$\frac{T_2}{T_1} = \left(\frac{p_2}{p_1}\right)^{\frac{n-1}{n}} = \left(\frac{V_1}{V_2}\right)^{n-1}$$

where $n = 1.35$

In this manner, initial pressures and temperatures were calculated over a range of

compression ratios and used as input to the detonation model. Figure B13 shows the results of this simulation. This graph makes no allowance for the likelihood of knock occurring, but shows the intensity of knock if it did happen. However, the main objective of this analysis is achieved, in that it is evident that under polytropic compression, the initial pressure is the dominant independent variable. Detonation pressures are significantly increased with additional compression.

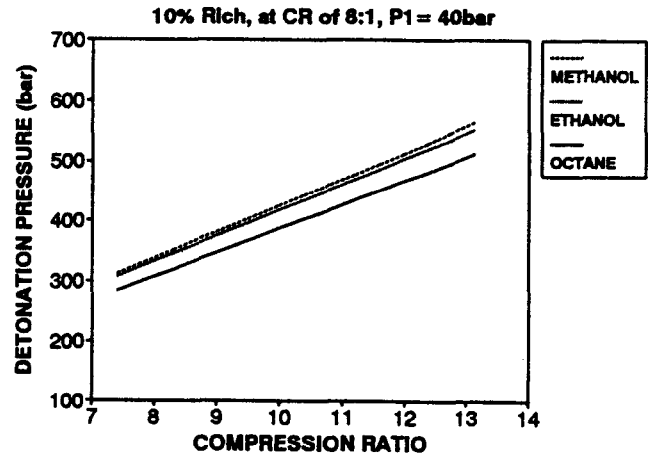

Figure B13: Effect of Polytropic Compression on Detonation Intensity

An immediate criticism of the relationships shown in figure B13 is that the end-gas temperatures for alcohol and octane would not be similar (at equivalent compression) due to evaporative cooling differences during the inlet process. An investigation by Moran and Yates [72] has shown that at low engine speeds the mixture temperature during the inlet process is about 22°C lower for methanol relative to gasoline. Reducing the methanol mixture temperature at inlet (ie: at a pressure of 1 bar) by 22°C and reworking the polytropic compression data, the two fuels may be compared on a more realistic basis. The reduction in end-gas temperatures (for methanol) would result in higher mixture densities (at equivalent compression), causing a more severe detonation pressure. The results of this analysis are shown in figure B14, from which it is predicted that methanol would exhibit a more severe detonation wave relative to octane. The complete explanation of this observation is as follows:

- Methanol exhibits a higher knock intensity due to the increased energy density at similar initial conditions to octane.
- The additional evaporative cooling, during the inlet process (gained from the higher heat of evaporation) for methanol, ensures lower end-gas temperatures and subsequently higher gas densities at similar initial conditions to octane.

- Methanol possesses a greater knock resistance than octane which indicates that knock would occur later in the compression process (from both piston and flame), further increasing the detonation pressures relative to octane.

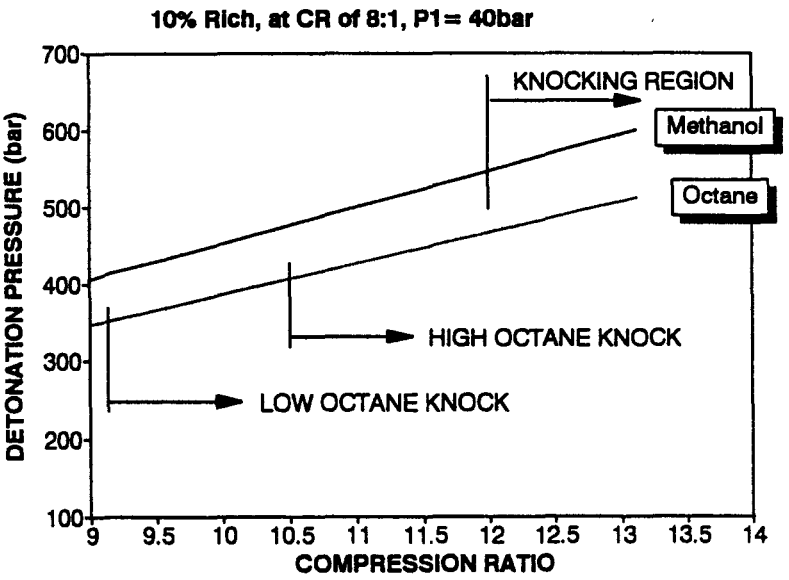

Figure B14: Comparison of Fuels at Realistic Operating Conditions

A further prediction can be made from the curve for octane in figure B14. Consider a range of gasolines with constant basic composition, but with increased quantities of an anti-knock additive (eg: TEL, TML, etc.). It is assumed that the additive does not fundamentally alter the energy density of the fuels. The gasoline with greater Octane Number will begin to knock at compression conditions higher than that of the lower Octane Numbers. From figure B14 it is predicted that the higher the Octane Number, the greater the detonation pressure (once the engine is knocking). This prediction will hold, whether knock is induced by increased compression ratio or spark advance, as in both cases the initial conditions are similar and the end-gas undergoes similar compression (ignoring relatively small differences in heat transfer). If knock is induced by increased inlet temperature (for the high Octane relative to the low Octane), this relationship will not apply as the inlet conditions are changed and effectively the increased inlet temperature, magnified to the point of knock could result in lower detonation pressures for the higher Octane fuel.

Production engines are usually optimised for a particular fuel by adjusting the mixture and spark timing maps. This work predicts that operating under equivalent knocking conditions

(with similar spark advance beyond the point of trace knock), the high Octane fuel will produce more violent shocks in the end-gas zone, than low octane fuels. More erosion damage would be expected from high Octane fuels under knocking conditions.

The addition of alcohol to the fuel in the form of gasoline-alcohol blends would further aggravate the situation. The alcohol would cause additional inlet cooling resulting in higher end-gas densities at the onset of knock. Provided the blend is used at similar equivalence ratios, the presence of alcohol constitutes an increased energy density in the end-gas. Together these effects would cause alcohol blends to exhibit stronger detonation characteristics, resulting in greater erosion.

were determined. Surface temperatures are nearly constant during compression, but show a sharp peak at the point of flame (or auto-ignition) arrival. Data from this work was as follows:

Knocking :	Initial Temperature	:	150 °C
	Peak Temperature	:	222 °C
	Peak Heat Flux	:	15 MW/m^2
Normal :	Initial Temperature	:	130 °C
	Peak Temperature	:	155 °C
	Peak Heat Flux	:	4 MW/m^2

The knocking data, above, were recorded at conditions which destroyed the surface thermocouples after a few minutes of operation. These data correspond to similar values reported by others [45,50,51].

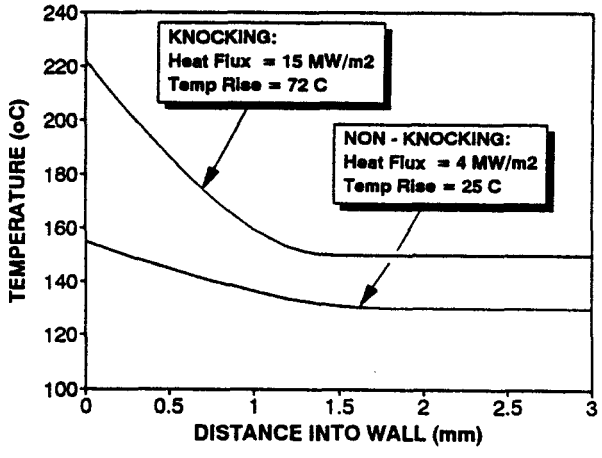

Figure C1: Temperature Profiles based on experimental surface temperatures

In order to model the correct temperature profile, the temperature gradient at the hot surface was matched to the heat flux as follows:

$$\frac{q}{k} = \left[\frac{\partial T}{\partial z}\right]_{z=0} = (T_s - T_i)\left[-\frac{3}{2}\frac{1}{\sqrt{8\,\alpha_d t}}\right]$$

where q - heat flux (W/m^2)

k - thermal conductivity (204 W/m^2°C)

α_d - thermal diffusivity (6.676 10^{-5} m^2/s)

By substituting the measured data into this relationship, the time (t) was solved which models the temperature profile at the instant of the measured heat flux:

Knocking conditions: $t = 0.0040$ seconds

Non-knocking conditions: $t = 0.0062$ seconds

The temperature profiles calculated in this manner are shown in figure C1. Having established a time instant, the thermal boundary layer thickness becomes a constant δ for each operating condition:

Knocking Combustion: $\delta = 1.46$ mm

Non-knocking Condition: $\delta = 1.82$ mm

Equation (2) for the temperature profile within the thermal boundary layer was simplified by using additional constants A and B as follows:

$$T(z) = T_s - Az + Bz^3$$

$$\textit{where} \qquad A = \frac{3(T_s - T_i)}{2\delta}$$

$$\textit{and} \qquad B = \frac{(T_s - T_i)}{2\delta^3}$$

Timoshenko [73] developed the analysis for thermal stresses due to non-symmetrical temperature distributions. Considering a plate of appreciable length and breadth, and of depth $2c$ (in the y direction), as shown in figure C2. A temperature distribution within the plate was assumed which varied as a function of y, such that the surface at $y = -c$ is at temperature T_s and the surface at $y = c$ is at temperature T_i. The thermal stress (σ_x), which is orthogonal to the temperature profile was described by:

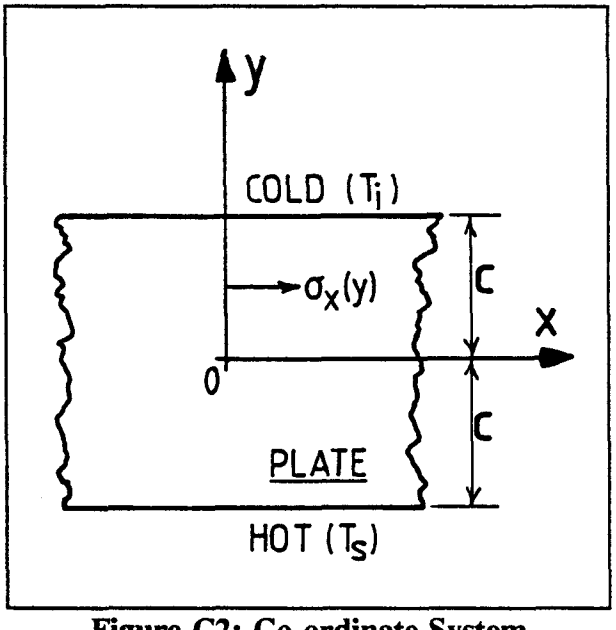

Figure C2: Co-ordinate System

$$\sigma_x(y) = \frac{\alpha E}{1-\nu}\left[-T + \frac{1}{2c}\int_{-c}^{+c} T dy + \frac{3y}{2c^3}\int_{-c}^{+c} T y dy\right]$$

where $T = T(y)$

and α - coefficient of thermal expansion

E - modulus of elasticity

ν - Poisson's ratio

The co-ordinate system (y) is relative to the centre of the plate, whereas the temperature profile previously developed (equations 1 and 2), used a co-ordinate system (z) relative to the hot surface. This necessitated the transformation of the z-axis to the y-axis by means of:

$$z = y + c$$

$$\therefore \quad T(y) = T_s - A(y + c) + B(y + c)^3$$

Simplifying this equation and assigning constants K, M and N, the temperature profile in the y co-ordinate system was as follows:

$$\text{For } y < (\delta - c): \quad T(y) = K + My + Ny^2 + By^3$$

$$\text{For } y \geq (\delta - c): \quad T(y) = T_i$$

$$\text{where} \quad K = T_s - Ac + Bc^3$$

$$M = 3Bc^2 - A$$

$$N = 3Bc$$

This temperature profile was integrated over the range - c to + c in order to produce the constant terms in the thermal stress equation. The integrals concerned were divided into

separate ranges due to the nature of the temperature profile, as follows:

$$\int_{-c}^{+c} T(y)\,dy = \int_{-c}^{\delta-c} T(y)\,dy + \int_{\delta-c}^{+c} T_i\,dy = I_1$$

$$\therefore\ I_1 = K\delta + \frac{M}{2}\left[(\delta-c)^2 - c^2\right] + \frac{N}{3}\left[(\delta-c)^3 + c^3\right] + \frac{B}{4}\left[(\delta-c)^4 - c^4\right] + T_i(2c - \delta)$$

$$\int_{-c}^{+c} T(y)\,y\,dy = \int_{-c}^{\delta-c} T(y)\,y\,dy + \int_{\delta-c}^{+c} T_i\,y\,dy = I_2$$

$$\therefore\ I_2 = \frac{K}{2}\left[(\delta-c)^2 - c^2\right] + \frac{M}{3}\left[(\delta-c)^3 + c^3\right] + \frac{N}{4}\left[(\delta-c)^4 - c^4\right] + \frac{B}{5}\left[(\delta-c)^5 + c^5\right] + \frac{T_i}{2}\left[c^2 - (\delta-c)^2\right]$$

The thermal stress as a function of depth into the wall was determined by substituting these integrals together with the temperature profile into the stress function, as follows:

$$\text{For } y < (\delta-c): \quad \sigma_x(y) = \alpha E\left[-K - My - Ny^2 - By^3 + I_1 + I_2 y\right]$$

$$\text{For } y \geq (\delta-c): \quad \sigma_x(y) = \alpha E\left[-T_i + I_1 + I_2 y\right]$$

Material properties for typical piston aluminium are as follows [34]:

α_d - 6.676 10^{-5} m^2/s (diffusivity)

k - 204 W/m°C

E - 64 10^3 MPa

α - 21.6 10^{-6} (coefficient of expansion)

σ_{max} - 171 MPa

These properties together with the established temperature profiles were used in a spreadsheet to calculate the stress within the walls of the piston or combustion chamber. Figure C3 shows the thermal stress distribution inside a 10 mm thick wall under knocking conditions. The higher temperature gradient at the hot surface (0 mm) produces extreme compressive stresses within 1 mm of the surface. Due to the compression in the skin, the central portion is placed in tension and the bending moment around the central zone causes the cold surface to be in compression. The magnitudes of the hot surface stresses are considerably higher than reported by Maly et al [34], whose thermal contact model estimated the stresses at between 4 MPa and 20 MPa. In contrast, this more detailed analysis used experimentally derived surface temperatures, and results in skin compressive stress are nearly 70% of typical proof stress values. The tensile stresses below the surface would aggravate the Hertzian stresses produced by the shock wave pressures.

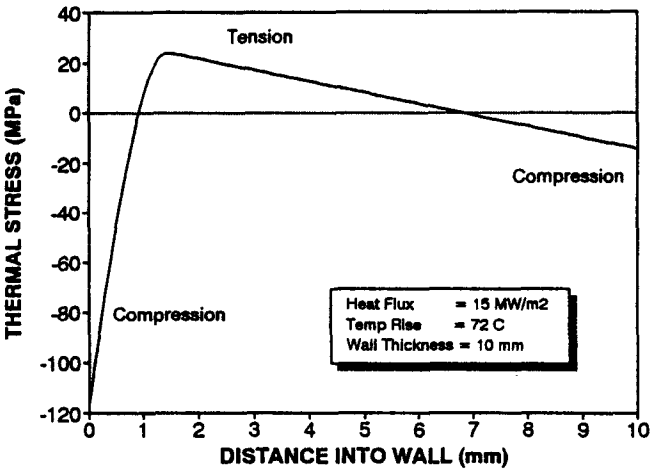

Figure C3: Thermal Stress inside the wall for Knocking Conditions

The wall thickness is another variable affecting the stress magnitude and distribution. Figure C4 shows the stress profile under knocking conditions for 3 different wall thickness. The compressive stress in the high temperature region increases with greater wall thickness. Conversely, it is seen that the thicker the wall the lower the tensile stress levels.

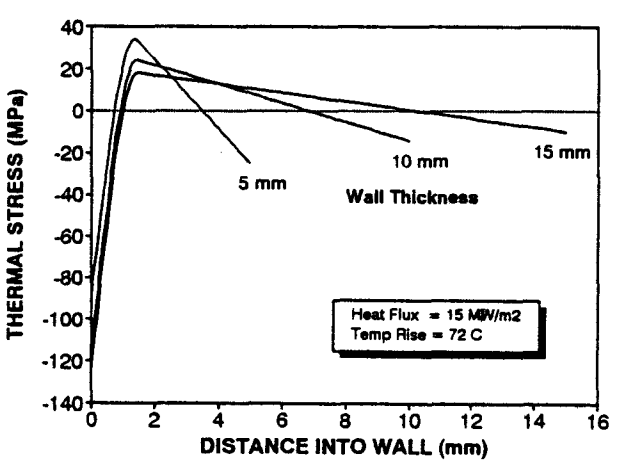

Figure C4: Effect of Wall Dimensions on Thermal Stresses under Knocking Conditions

Figure C5 compares the stresses between knocking and non-knocking conditions inside a 10

mm wall. In comparison to normal operating conditions, the compressive thermal stresses are over 3 times greater for knocking combustion, while the tensile stresses are more than double. Due to the thinner thermal boundary layer in the case of knock, the peak tensile stresses are closer to the surface than for normal operating conditions, which would further aggravate the skin loading.

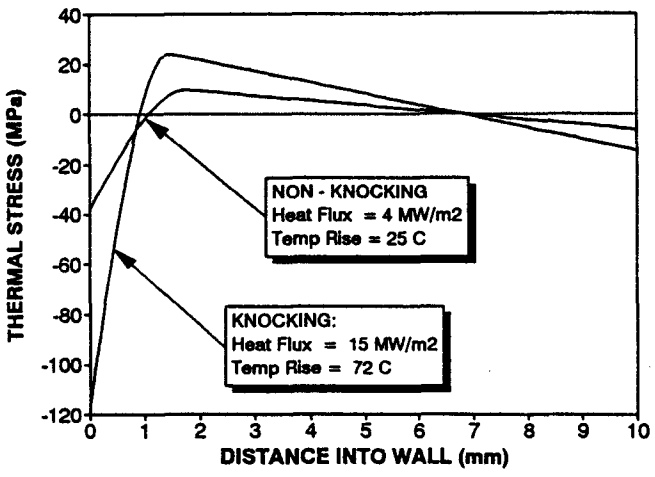

Figure C5: Comparative Thermal Stresses in a 10 mm wall

Figure C6 shows the comparison between knocking and normal combustion for a 5 mm wall. Although the hot surface compressive stresses are reduced, the maximum tensile stress of the knocking condition is increased relative to the non-knocking condition.

It was the intention of this model to provide a first order analysis of the thermal conditions within the walls of the combustion chamber and piston. With this in mind, the accuracy of the analysis warrants consideration.

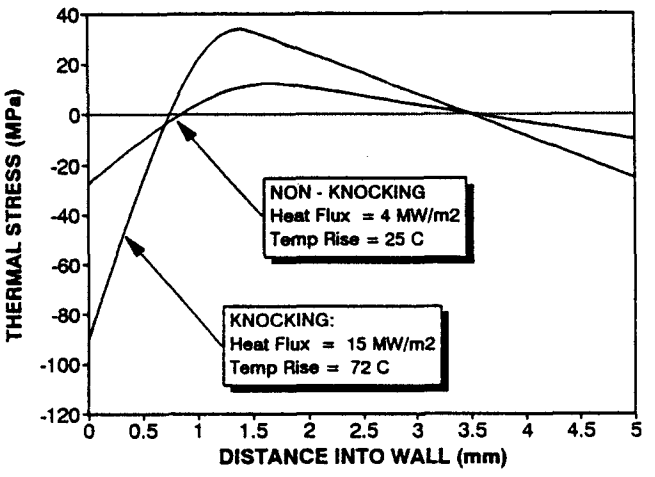

Figure C6: Comparative Thermal Stresses in a 5 mm wall

Although experimental data was used for the hot surface, it was assumed that the cooler surface was at the initial temperature (T_i). In reality, the cooler surface is either air, water or oil cooled, depending on the engine type and the surface concerned. It is expected that the cooler surface would thus operate at lower temperatures than the mean temperature of the hot surface, thereby causing a general increase in the temperature gradient (relative to the gradients used in this analysis). Thus the thermal stresses in an engine should be even greater than those predicted by the model.

The relationships used in this analysis includes stress conditions in 3-dimensions (by accounting for the Poisson Ratio effects). However, Timoshenko's equation was based on the assumption that the temperature on a surface parallel to the walls was constant [73]. In engines, it is unlikely that planes parallel to the walls would exhibit constant temperatures, due to heat transfer along the walls. An additional temperature gradient along the walls would increase the local thermal stress (in the area of steepest temperature gradient) above the levels calculated with the modelled temperature profile.

The model made no allowance for the time related effects, as the analysis was based on the peak transient temperature profile. The thermal stresses will naturally rise with the onset of the shock and fall with the passage of this thermal wave through the material. Because the model was based on the maximum measured temperatures, it was assumed that this represents the maximum thermal stress condition, other effects notwithstanding.

All these items indicate that this analysis is a conservative indicator of the true operating conditions, and that in reality the thermal stresses would be greater than those predicted.

APPENDIX D: DETONATION CHAMBER TESTS

As discussed in chapter 2, the circumstances that produce knock in an engine are erratic and therefore it is very difficult to produce controlled conditions using engine tests. The detonation chamber gives the researcher a controlled and repeatable tool to simulate conditions in a knocking engine. Maly et al [34] have used a detonation chamber for these purposes, with encouraging success. The detonation experiments described in this appendix were aimed at fulfilling the following objectives:

- To provide experimental validation for the detonation model, in terms of predicting the characteristics of detonation waves based on the initial conditions.
- To investigate the effect of some operating and geometric variables on the amount of erosion damage induced by detonation waves.

The detonation chamber used in these tests comprised of a rigid channel, with inlet and outlet ports at either end. Fuel and oxidant were mixed and allowed to flow continuously through the channel. A spark-plug, positioned at the end of the chamber, was fired at regular intervals so that, with the correct choice of reactants, a detonation wave was produced. Either an aluminium specimen or a pressure transducer was mounted at the end of the chamber (opposite the spark-plug), to be exposed to the detonation conditions.

D.1 CHAMBER DESIGN

The design of the chamber used in this work was based on the information contained in the Maly et al publication [34]. The internal cross section of the chamber was chosen to be 20mm by 20mm with a length of 200 mm. The chamber was constructed from 12mm thick, SS304 stainless steel.

A gaseous mixture of ethylene and oxygen was used because it has a similar energy density at atmospheric pressures to the end-gas in an engine at to auto-ignition. This mixture produces a detonation wave at atmospheric pressures. The shock intensity was adjusted by changing the mixture strength.

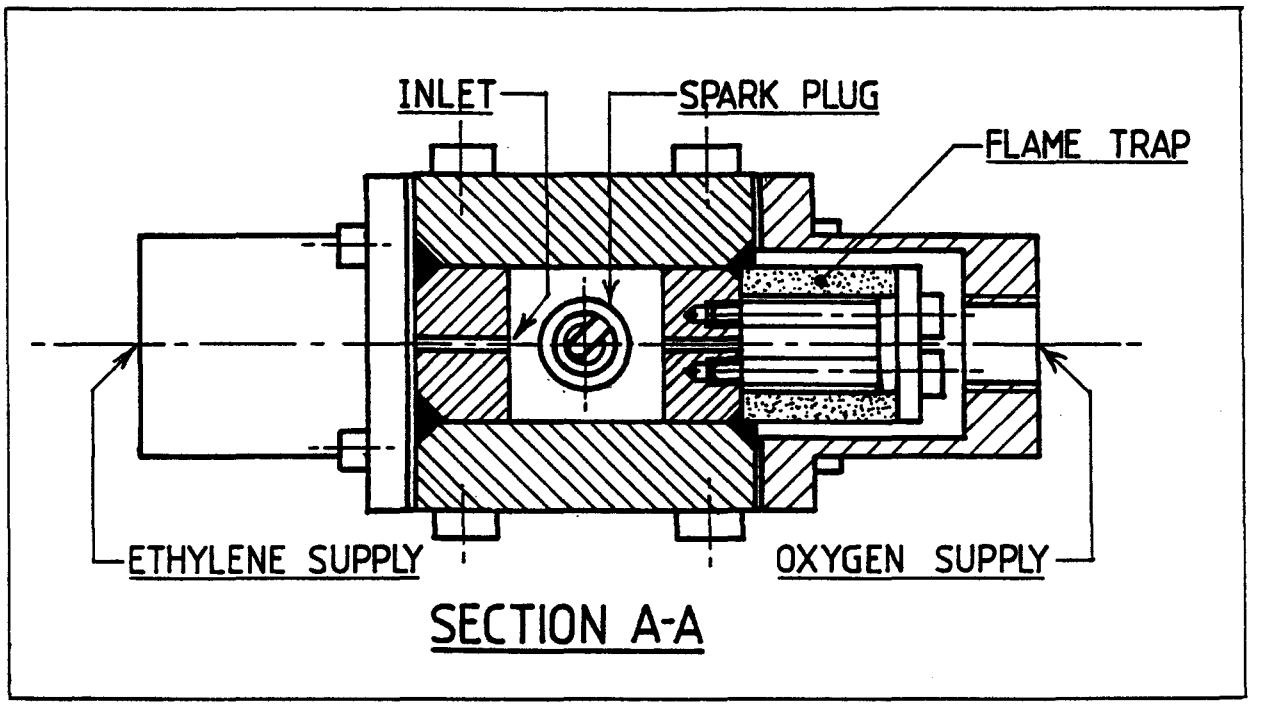

Figure D1: Sectional views through chamber showing inlet ports

A continuous flow system with opposed inlet ports for ethylene and oxygen was used to provide good mixing. Flame suppressors comprising of sintered phosphor bronze where fitted upstream of the inlet ports to prevent flashbacks. A sectional view of the inlets and chamber are shown in figure D1. Gas flow for each stream was controlled using pressure regulators and needle-valves which were calibrated regularly by timing a unit volume of gas bubbled into an inverted measuring cylinder filled with water. The mixture strength is presented in terms of the fuel-oxygen equivalence ratio.

A muffler was constructed and fitted to the exhaust. An air supply from an external compressor was attached to the muffler to lean out any combustibles remaining in the exhaust. The combined exhaust and excess air was directed into an extraction system for additional safety.

The spark-ignition system was constructed from a capacitive discharge ignition (CDI) and coupled to a variable-frequency pulse generator. A standard automotive spark-plug was used as the ignition source. The frequency of ignition and the combined gas flow rate were established as follows. Running the chamber with the desired mixture strength at a combined flow rate of about 3 litres/minute, the frequency was set at about 2 Hz. The excess air to the muffle was shut off and the frequency slowly reduced, until the mixture in the muffle

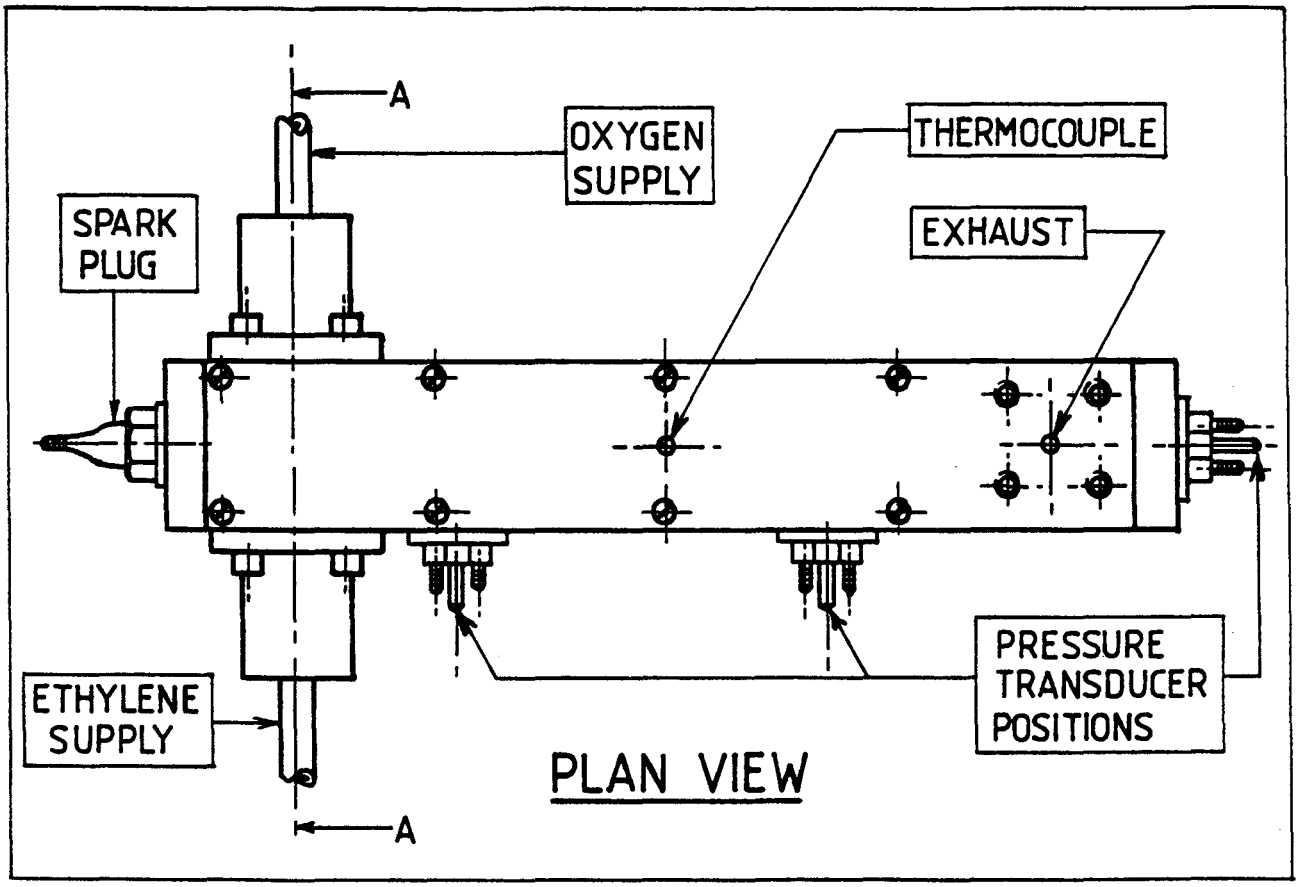

Figure D2: Plan view of detonation chamber showing mounting positions of pressure transducers

began to ignite. This was taken as the point at which complete scavenging occurred (notwithstanding zones of recirculation). The frequency was further reduced at this flow rate to ensure effective scavenging. The ignition frequency established by this method was just under 1 Hz.

In order to maintain steady state operation, an aluminium sheet casing was fashioned to fit around the chamber with an air gap of about 10 mm all around. A fan, with an adjustable baffle on the inlet, was connected via a duct to this casing (at the specimen end). The fan provided sufficient cooling to maintain a constant operating temperature, which was controlled by the position of the baffle. However, the range of specimen temperatures was somewhat limited by this system, and other methods had to be used to achieve extremely high and low temperatures.

Instrumentation used in these tests included pressure transducers and thermocouples to

measure both material and gas temperatures. A thermocouple was placed in a stainless steel pocket protruding 4 mm into the chamber and positioned midway between spark and specimen. It was used when calibrating the mass flow rates, and also used as an indicator for steady state conditions. Three tapped holes were machined into the chamber to allow pressure transducers to be mounted flush with the inner walls, as shown in figure D2. The mounting points used for the transducers were dependent on the tests being performed, which will be discussed in the following section. Two AVL 12QP pressure transducers were used together with charge amplifiers and digital oscilloscope as detailed in Appendix F.

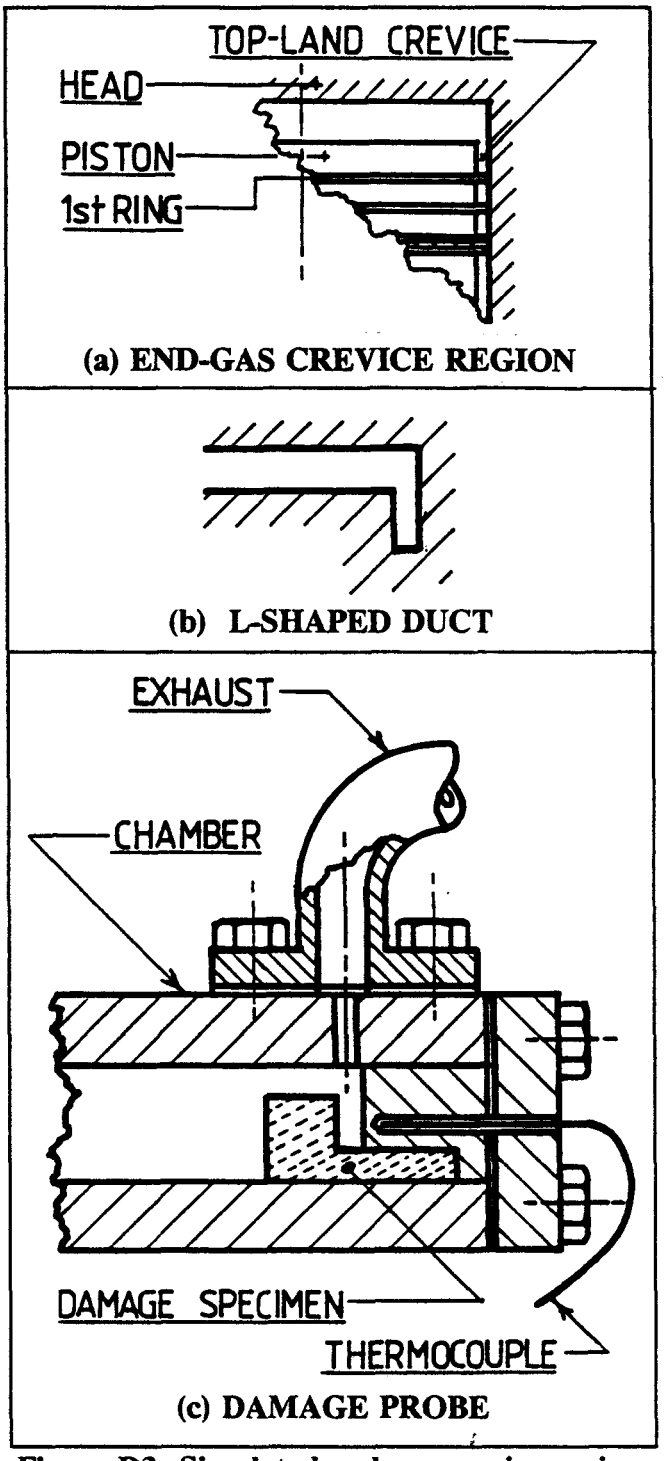

Figure D3: Simulated end-gas crevice region

The damage specimen geometry was derived from considerations of the end-gas crevice region in an engine. As discussed in chapter 2, the region most commonly eroded by knock is the piston top-land. This region forms an annular crevice shown in the figure D3(a). Due to the large difference between the gap width and the piston circumference, the geometry may be simplified to 2 dimensions. Thus the damage specimen was chosen as an L-shaped duct as shown in figure D3(b).

The dimensions of the specimen were derived from considerations of the chemical timescales which are roughly inversely proportional to the initial pressure [34]. If the chamber is

operated at atmospheric pressures, then the gas density is about 50 times less than in the case of the end-gas in an engine. To achieve a comparable conditions, the specimen dimensions should thus be increased 50 fold (compared to dimensions in the crevices of an engine).

The damage specimen (or probe) comprised of two sections bolted together as shown in figure D3(c). Erosion of the piston top-land was of interest, therefore the "piston section" of the specimen was made of aluminium, while the rest was constructed from steel (which was not expected to be eroded). This arrangement allowed for a simply manufactured specimen (which would have to be replaced) and allowed for the gap dimension (between the simulated piston and bore) to be easily varied. A 6063TF aluminium was used, having similar material properties to typical piston alloys.

A thermocouple was fitted into the steel section of the specimen as shown in figure D3(c). The tip of the thermocouple was positioned within 0.5 mm of the inside wall of the specimen. Although this temperature would not correspond to the exact material temperatures in the aluminium, it would show the effect of changes in material temperatures under various operating conditions.

D.2 DETONATION TEST PROCEDURE

Testing commenced with a pressure transducer fitted at the far end of the chamber (opposite end to the ignition point). No specimen was used for these tests. Pressure traces were captured over a wide range of mixture strengths, to evaluate the general operating conditions in the chamber. It was apparent that when leaning the mixture below a critical strength a transition occurred from detonating to deflagrating combustion, as observed by the sudden disappearance of pressure spikes. This was further evident by the significant reduction in the audible noise from the chamber.

Several tests were performed with two pressure transducers positioned at various points along the chamber to determine the location of the deflagration-detonation transition. These tests were to check that a developed detonation wave had been established well before the end of the chamber.

With a single transducer positioned at the end of the chamber, traces were captured over a range of detonating mixture strengths at steady state conditions. At each operating point 10 traces were captured, and the peak pressures averaged for that condition. These data were used to validate the detonation pressures predicted by the model as a function of fuel-oxygen equivalence ratio.

Subsequent tests were performed with damage specimens mounted at the end of the chamber (in place of the pressure transducer). With the thermocouple in positioned inside the specimen, the cooling fan baffle was adjusted to hold the temperature constant. Each specimen was subjected to 10 000 shots in the chamber.

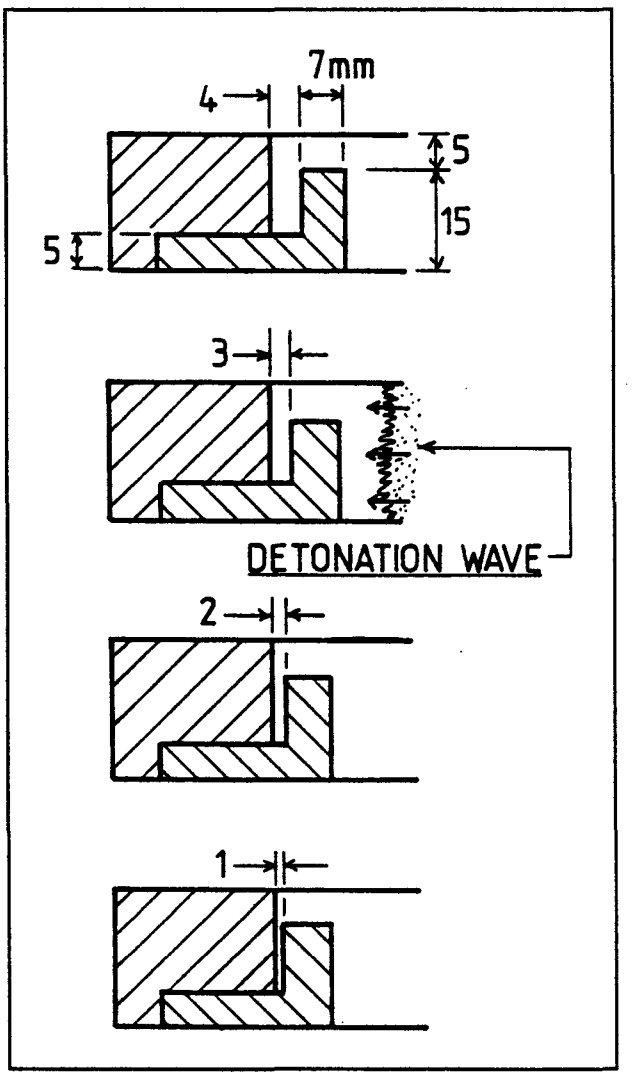

Figure D4: Damage specimen geometries

The aim of these tests was to evaluate the nature and severity of damage and to establish the effect of the crevice gap on the damage. The thermocouple temperature was held at 190°C for these tests. Four specimens were tested with different crevice gaps, as shown in figure D4. All other dimensions were held constant.

An experiment was conducted to determine the effect of material temperatures on erosion damage. Identical probes with a 3 mm gap were exposed to 10 000 shots. In some of these tests, the end of the chamber (with the specimen) was mounted in a basin, and a water supply with controllable flow rate was fed into the basin and allowed to overflow to the drain. By varying the water flow rate, the temperature of the specimen could be held constant at temperatures as low as 60°C. Other tests were performed with insulation on the chamber, which permitted stable temperatures of up to 350°C to be achieved.

It was hoped that the erosion damage could be measured on a mass-loss basis. The initial specimens were manufactured with small wall thicknesses (to extend the sensitivity of mass-loss measurement). However when tested, these specimens were unable to withstand the stresses in the chamber and in each case the exposed vertical wall of the specimen sheared at the base. Even with a specimen wall thickness of 5 mm, the vertical wall was found to be bent after a few minutes of testing. Ultimately a wall thickness of 7 mm was found to be great enough to withstand the structural stresses in the chamber. However, with this large size, the mass-loss during a test was too small to be accurately measured.

Consequently, a subjective scale was used to evaluate the magnitude of the damage. The erosion experiments reported by Maly et al [34] also had to rely on a subjective evaluation of the level of damage. The inner surface and the inner corner, shown in figure D5, where given a visual damage rating of between 0 and 10. The scale used was as follows:

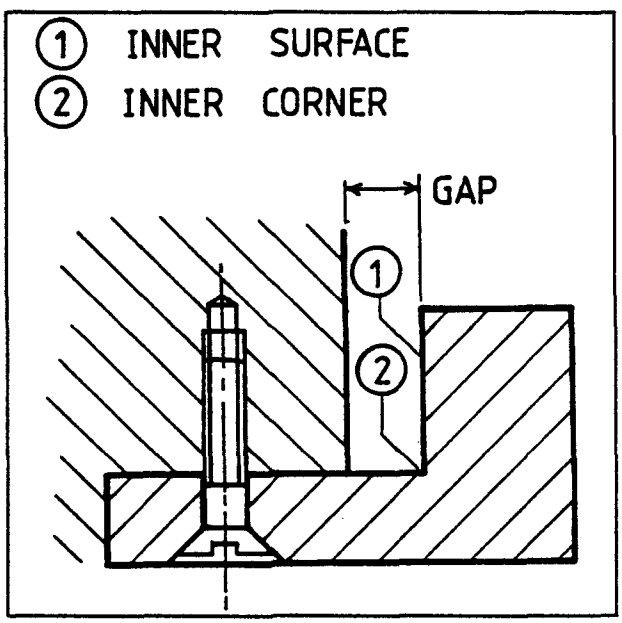

Figure D5: Regions evaluated for damage

0	-	no damage
2	-	very slight damage
4	-	intermittent spots and blasting
6	-	non-uniform sand blasting
8	-	uniform heavy sand blasting
10	-	heavy localised pitting

These two regions were evaluated as they correspond to the piston top-land and the corner of the top-land and ring, which have been identified as erosion regions. The rest of the regions in this simulated geometry correspond to the bore and ring which are not attacked by knock-induced erosion (as they are constructed of much tougher materials).

Although this subjective damage intensity is not accurate on a quantitative scale, it was

possible to accurately order the specimens in terms of damage relative to each other.

D.3 DETONATION CHAMBER RESULTS AND DISCUSSION

A typical pressure trace taken with the pressure transducer positioned at the end of the chamber is shown in figure D6. Two aspects of this trace need to be addressed. The first concerns the appearance of a positive pressure rise preceding the main pressure spike. The other concerns the nature of the high frequency oscillation superimposed on the trace. Both of these observations were seen on all pressure traces.

On striking the chamber with a hammer, to produce a similar audible noise level to the detonation, it was found that the pressure transducer produced a decaying oscillation with peak amplitudes similar to the small pulse observed on the pressure traces. It was deduced that the small pulse was being caused by the chamber's structural response to the start of the detonation process. Evidently, the detonation produces a stress wave in the wall material which travels at higher velocities than the detonation wave through the gas, thus arriving at the transducer earlier than the detonation wave. This phenomenon was used to estimate the position in the chamber at which the detonation transition occurs.

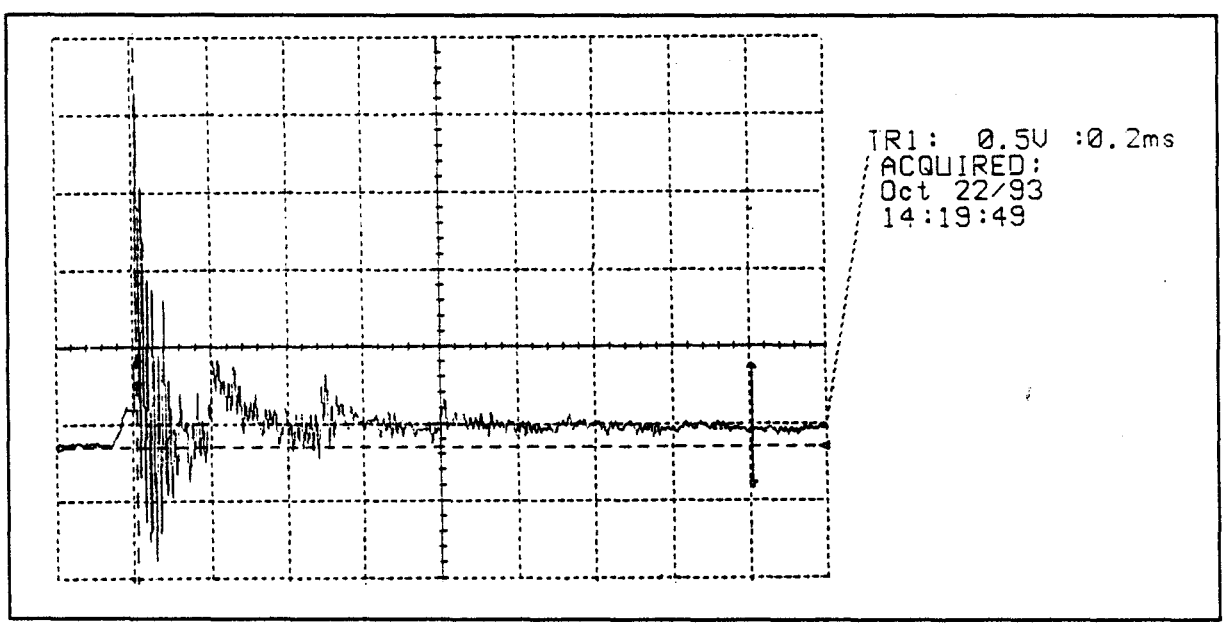

Figure D6: Detonation chamber pressure trace

The acoustic velocity (c_{solid}) within a solid may be described as follows:

$$c_{solid} = \sqrt{\frac{\beta}{\rho}} \qquad (m/s)$$

$$\textit{where} \quad \beta = 16.10^{10} \ \textit{bulk modulus}$$
$$\rho = 7860 \ kg/m^3 \ \textit{density}$$

$$\therefore \ c_{solid} = 4512 \ m/s$$

From the theoretical model, the detonation wave velocity (u_{det}) under these operating conditions is 2118 m/s. From the pressure trace shown in figure D6, the time difference (Δt) between the arrival of the stress wave pulse and the detonation spike is about 0.02mS (which was nearly constant for all operating conditions). The distance from the transducer (x_{det}) at which the detonation transition occurs may be estimated as follows:

$$\Delta t = \frac{x_{det}}{u_{det}} - \frac{x_{det}}{c_{solid}}$$

$$\therefore \ 0.00002 = \frac{x_{det}}{2118} - \frac{x_{det}}{4512}$$

$$\therefore \ x_{det} = 0.080 \ m = 80 \ mm$$

In other words, detonation commences at about 120mm from the spark plug, well before the transducer (or specimen). This was confirmed by placing two pressure transducers in the other two positions, at 65mm and 160mm from the spark plug, respectively. Simultaneous traces indicated that the transducer furthest from the spark was first to respond to the detonation wave followed by the transducer closest to the spark. Taking the time difference, and relative displacement of the transducers, it was apparent that the transducer nearest to the spark plug was responding to the shock wave reflected from the end of the chamber. This showed that the detonation transition occurred between the two transducers and confirmed the estimated position of 120mm from the spark plug.

The high frequency oscillations on the pressure trace were analysed and shown to be caused

by the transverse reflections of the shock waves across the chamber. Assuming a half wave corresponding to the 20mm chamber width, the fundamental frequency was determined to be 53 kHz. This matched the measured pressure oscillation of about 55 kHz.

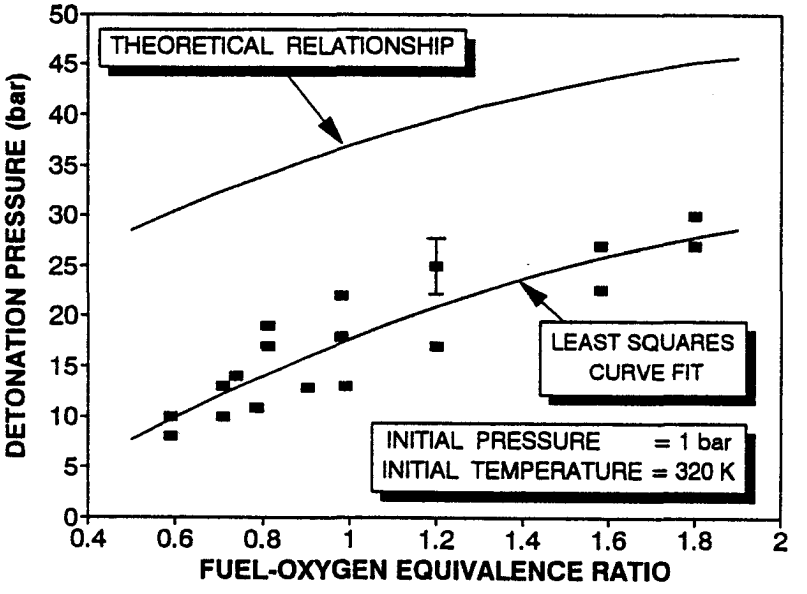

Figure D7: Theoretical and measured detonation pressure

The results of the measured and theoretical detonation pressure as a function of equivalence ratio are shown in figure D7. Each data point shown in this graph corresponds to the mean of 10 measurements. The mean standard deviation for these measurements are also illustrated. It is seen that the experimental data falls below the predicted values. However, the data follows a very similar trend to the theoretical predictions, as shown by the quadratic curve fitted to these data. The fact that the trend of the theoretical model is validated is sufficient for the purposes of predicting the effects of changes in initial conditions.

Figure D8 shows the results of the damage tests performed on the specimens with variable gap width. The inner surface is significantly affected by the magnitude of the crevice gap. In all cases the damage was found to occur close to the corner.

A similar, but more intense effect was observed at the inner corner of the specimens, with a crack and severe undercut developing at the largest gap tested. A further observation made on all these samples was a small undercut at the opposite corner (where the aluminium and steel portions are connected). From these observations, it is seen that the worst damage

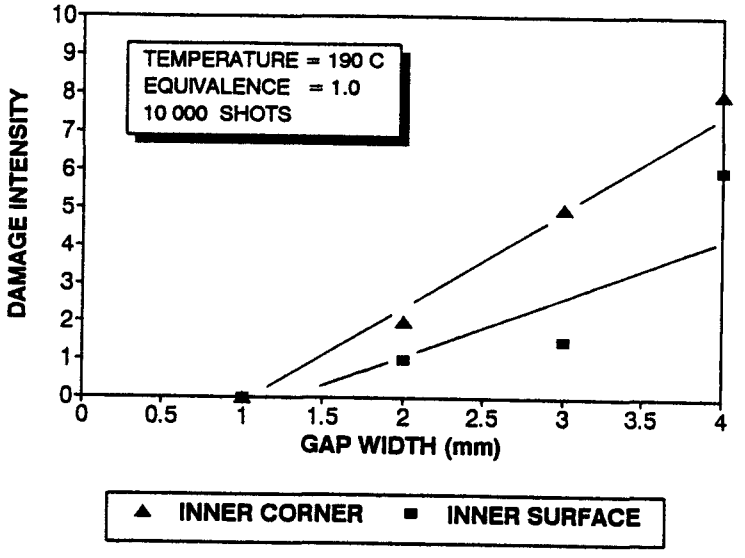

Figure D8: Effect of gap width on damage intensity

occurs at the corners, which is similar to the typical erosion damaged found at the first compression ring groove.

In chapter 3 it was observed that typical erosion (if not stopped) forms a blow-by channel around the first ring. These detonation chamber observations show the initiation process, by which the shock wave is focused down the crevice gap and removes material at the corners. In the case of an engine, the bottom and outside surfaces of the specimen are the ring and bore respectively, which are resistant to erosion damage. Therefore, it is the piston that is eroded although the other surfaces experience similar pressure pulses.

Figure D9 shows the results of the damage tests performed over a range of specimen temperatures. Elevated temperatures increase the amount of erosion damage. The most significant effect is at the corner where an undercut developed on all specimens tested above 200°C. At temperatures above 300°C a cavity of over 1mm deep developed along the whole corner for all specimens. The increased damage at elevated temperatures is attributed to the reduction of yield strength. For this aluminium, at 190°C the 0.2% proof stress is nearly halved, while at 350°C it is about 10% of its value at ambient temperatures [74].

It was observed that in all the tests performed, the front surface of the specimens (facing the oncoming shock) was relatively undamaged, irrespective of the level of erosion occurring

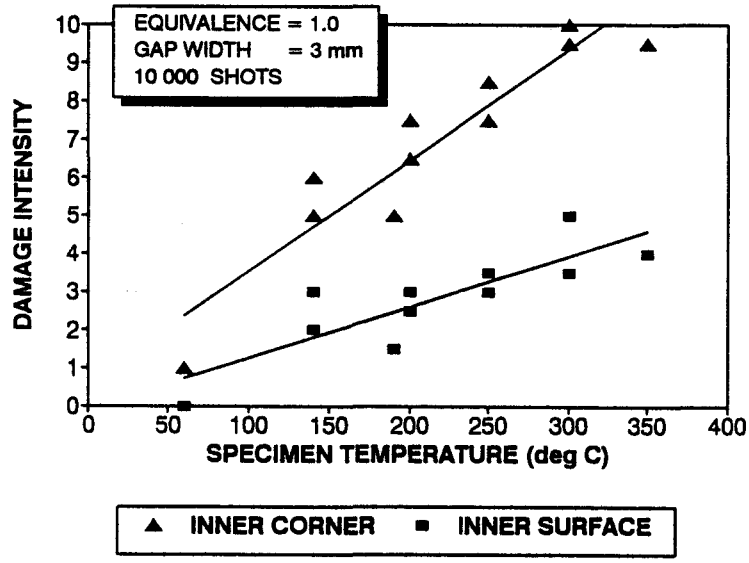

Figure D9: Effect of specimen temperature on damage intensity

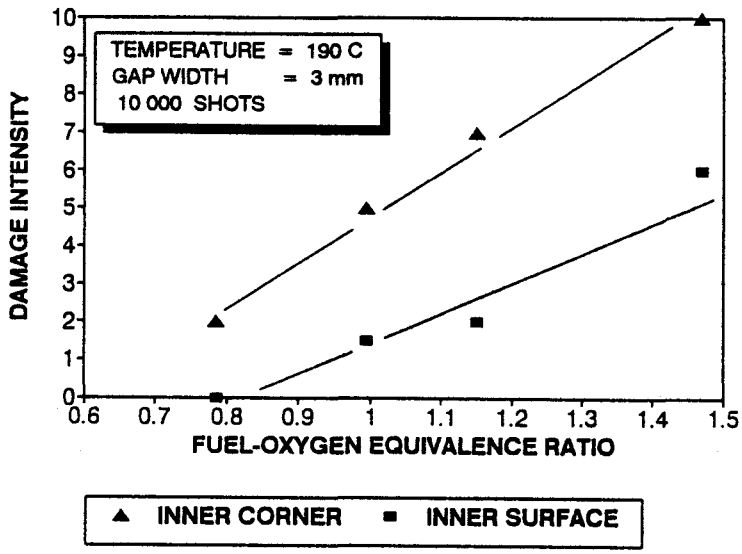

Figure D10: Effect of mixture strength on damage intensity

inside the crevice. This fact illustrates the importance of the wave interaction in the crevice region, and explains why erosion is rarely found on unbounded piston and head surfaces.

Figure D10 shows the damage test results over a range of equivalence ratios. The severity of erosion is seen to increase with mixture strength.

Photographic examination of damaged specimens was undertaken and typical examples for

various temperatures tested are shown in figure D11. These pictures demonstrate the extent of the detonation action in the corner compared to the rest of the crevice surfaces, and the effect of specimen temperature.

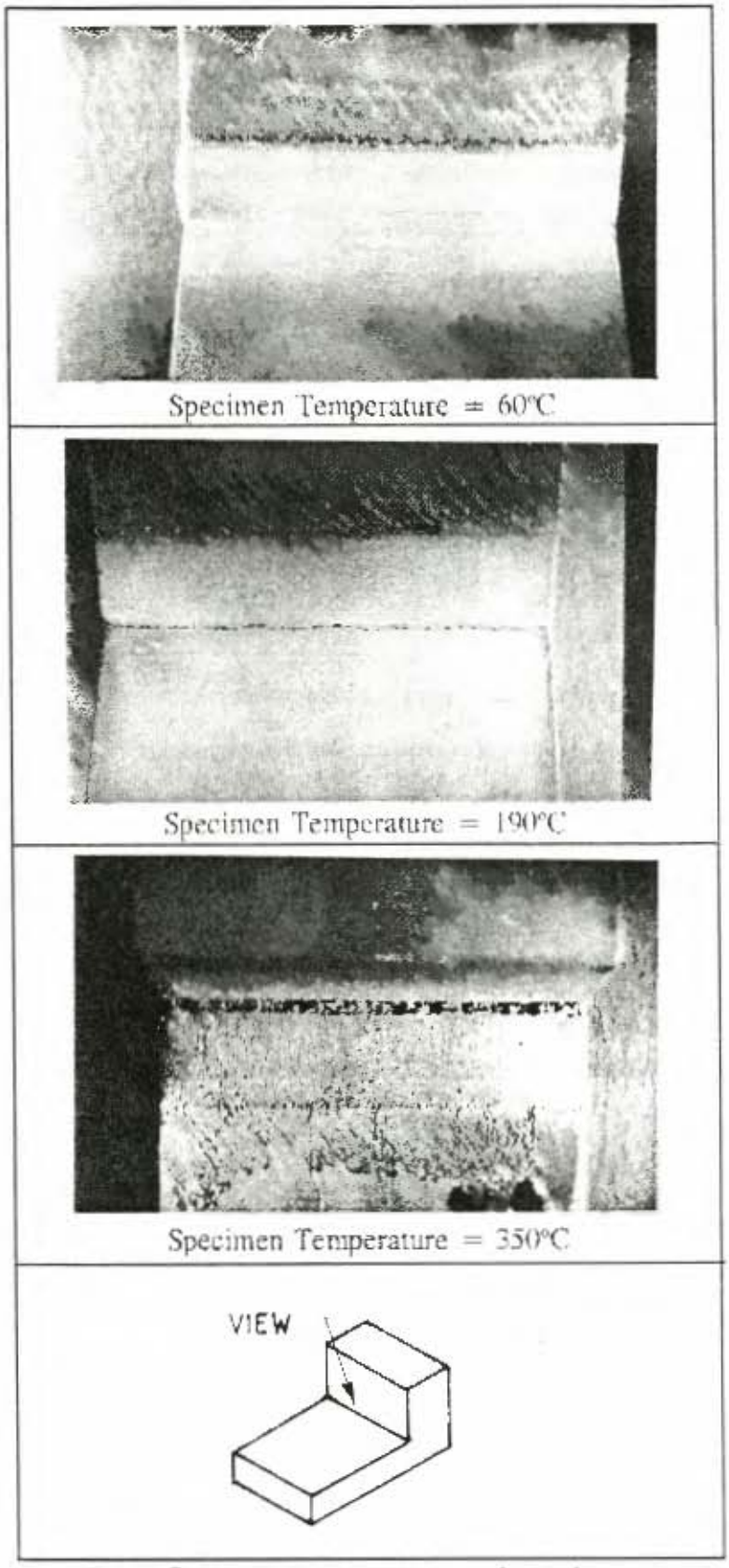

Figure D11: Detonation damaged specimens: 10 000 Shots; Stoichiometric Conditions; 3 mm Specimen Gap

APPENDIX E: ENGINE EROSION STUDY

This engine study investigated the effect of fuel and operating conditions on knock-induced erosion. An experimental method was developed to expose a specimen, located in the combustion chamber, to controlled knocking conditions and thus directly measure the amount of erosion.

E.1 EXPERIMENTAL DEVELOPMENT

The development of the equipment and experimental method progressed through various phases described in the following sections.

E.1.1 ENGINE MODIFICATION

A Ricardo E6 research engine was modified so that an aluminium specimen could be inserted into the combustion chamber. To accomplish this, a 12 mm thick spacer plate was fitted between the cylinder-head and bore.

The engine was run under extremely rich (non-knocking) conditions so that a carbon deposit was built up over the surface of the spacer plate. After operating under knocking conditions, the spacer plate was removed and the inner surface examined. The position of the end-gas region was identified as corresponding to the area on the spacer plate where the deposit had been removed. At this position, a cavity 10 mm deep by 25 mm wide was machined into the spacer plate, together with an access hole for the specimen, as shown in figure E1. Repeating the "deposit-knocking" test with the modified spacer plate showed that the deposits were removed from within the cavity.

An advantage of this arrangement is that the maximum flame path, from spark-plug to the cavity, is not affected by changes in compression ratio. The design of the cavity shape also took into account the path of the inlet swirl, to ensure good scavenging.

A connecting-rod of increased length (of 12 mm) was manufactured and used to accommodate the increased cylinder volume, allowing the normal range of compression ratios

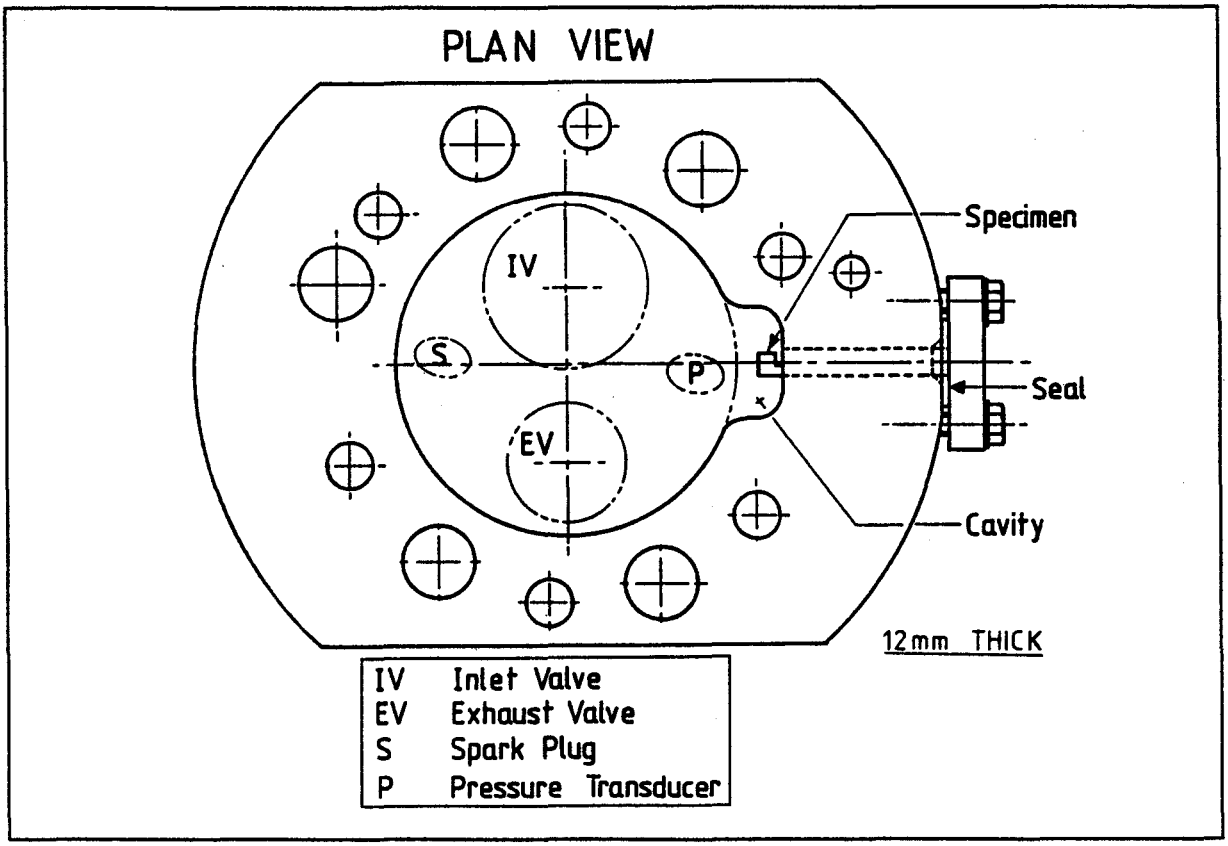

Figure E1: Spacer plate showing the position of the specimen

to be achieved.

E.1.2 DEVELOPMENT OF SPECIMEN GEOMETRY

The geometry of the specimen was optimised to achieve the greatest possible susceptibility to erosion damage. Various specimen geometries were tested under similar knocking conditions. The material used for the specimens was 6063TF aluminium alloy, which has similar properties as piston alloys.

Referring to figure E2, the first specimen (A) with a flat surface mounted flush to the wall showed no damage. This result was accepted as evidence that knock rarely erodes the unconfined regions of the combustion chamber and piston crown, as discussed in chapters 2 and 3. As a result, all subsequent specimens included some form of crevice region.

Specimen B, with 0.2 mm slots perpendicular to the front face was also found to produce no damage. It was considered that due to the size of the slots, very poor scavenging had

occurred.

A wider slot of 1 mm was tried (specimen C) which produced a small amount of erosion, after 40 minutes of testing under heavy knock.

To improve scavenging in the crevice, specimen D was designed with a crevice parallel to the front face. This geometry produced a significant increase in the erosion. However, it was found, that at the conclusion of most tests, the 2 mm thick front wall of the specimen was bent outwards and in some cases completely fractured at the base.

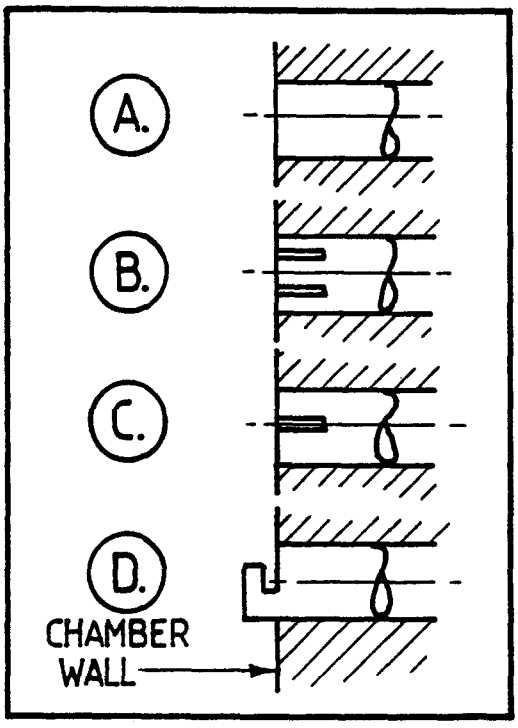

Figure E2: Specimen geometries evaluated

To prevent the fracture of the front wall, the thickness was increased to 4 mm. The specimen geometry finally adopted, shown in figure E3, produced significant erosion after 15 to 30 minutes of testing, seen in figure E4.

The specimens were screwed onto a mounting rod which was sealed at the exit point of the spacer plate, as shown in figure E1. A ceramic collar, shown in figure E3, was fitted between the specimen and rod, to prevent unnecessary heat loss.

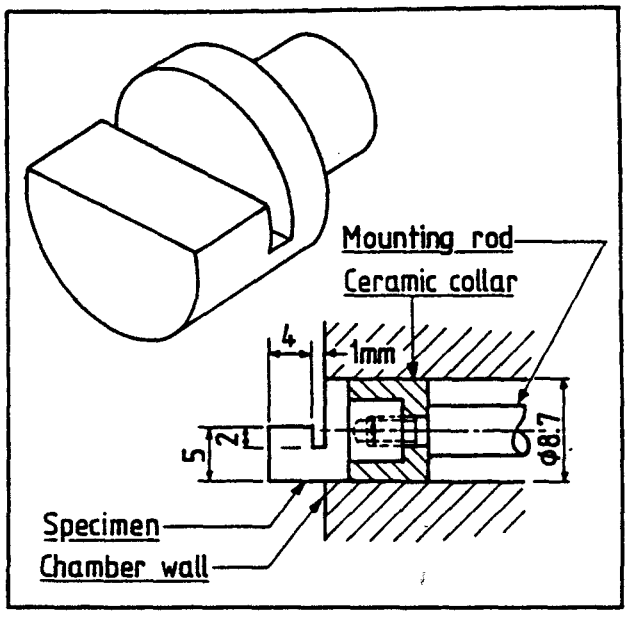

Figure E3: Adopted specimen geometry

Provision was made to monitor the specimen temperature, by drilling a hole down the length of the mounting rod and fitting a thermocouple into a pocket in the specimen. Tests run with the thermocouple placed showed that temperatures of between 170°C and 210°C were

achieved. However, the thermocouple could not be used during the damage tests, because the erosion formed a blow-hole into the thermocouple pocket.

The orientation of the specimen was found to have a significant effect on the amount of erosion. The specimen orientation shown in figure E1 was chosen for its greatest susceptibility to damage.

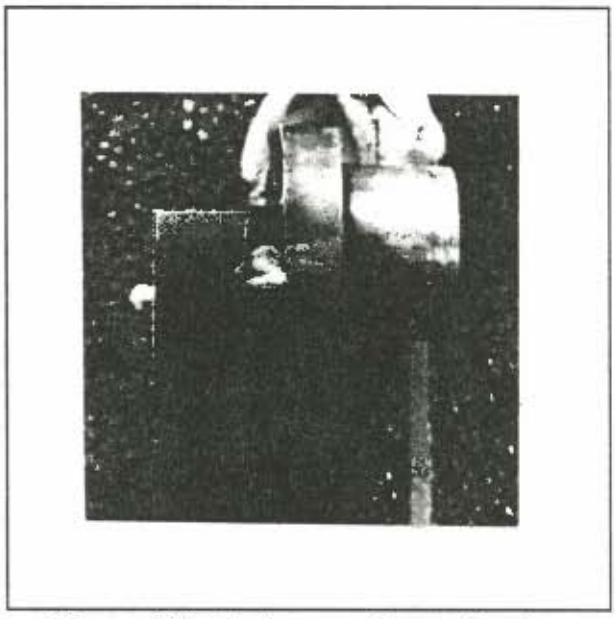

Figure E4: Engine specimen showing erosion damage

E.1.3 ESTABLISHING TEST CONDITIONS

Using the adopted specimen geometry, qualitative erosion tests were performed to evaluate the effects of various engine operating conditions. The observations made during this phase were used to establish the operating conditions used for quantitative testing. A subjective evaluation of damage was made, in a similar manner to that used in the detonation chamber tests.

A variety of operating conditions were tested using 93 RON gasoline. The observations made were as follows:

Engine Speed:

Greatest damage was encountered at low engine speed. This was possibly due to greater swirl at higher speeds, which caused the end-gas zone to be shifted away from the cavity.

Fuel-Air equivalence ratio:

It was found that the greatest amount of damage occurred at a 10% rich mixture.

Inlet air temperature:

The effect of daily variations in ambient temperature was found to affect the

repeatability of the knock intensity (as defined in section E.2). This problem was obviated by raising the inlet air temperature above the ambient conditions. Furthermore, the elevated inlet temperature facilitated the reduction in compression ratio (which was limited by the modified combustion chamber).

Test duration:

A series of specimens were periodically removed, examined and replaced during testing. It was found that over the first 5 minutes of testing, very little damage occurred. After 10 to 15 minutes the erosion seemed to stabilise. Comparing specimens tested for 15 minutes and 60 minutes, showed only small differences in the level of damage.

Compression ratio and spark timing:

These parameters were to be used to control the knock intensity in the final phase of testing. They were chosen to provide the basis of testing over a range of knock intensities as discussed in the results.

E.1.4 DAMAGE INTENSITY MEASUREMENT

Initially, the mass of material eroded was measured. However, under heavy knock, less than 2 milligrams was removed from the 10 gram specimen. The mass loss was at the limits of the mass balance and therefore this procedure was not sufficiently sensitive to the requirements of the research investigation.

An alternative method was therefore developed to objectively measure the extent of the specimen erosion. This involved the optical measurement of the amount of cross-sectioned area of the specimen surface that was removed by the erosion. The sides of the specimens were milled away and polished, as illustrated in figure E5. Jigs were used during the polishing process to ensure that the cross-sectional plane was at the same location in each case.

Both sides of the specimen were photographed using a standardised camera set-up to ensure

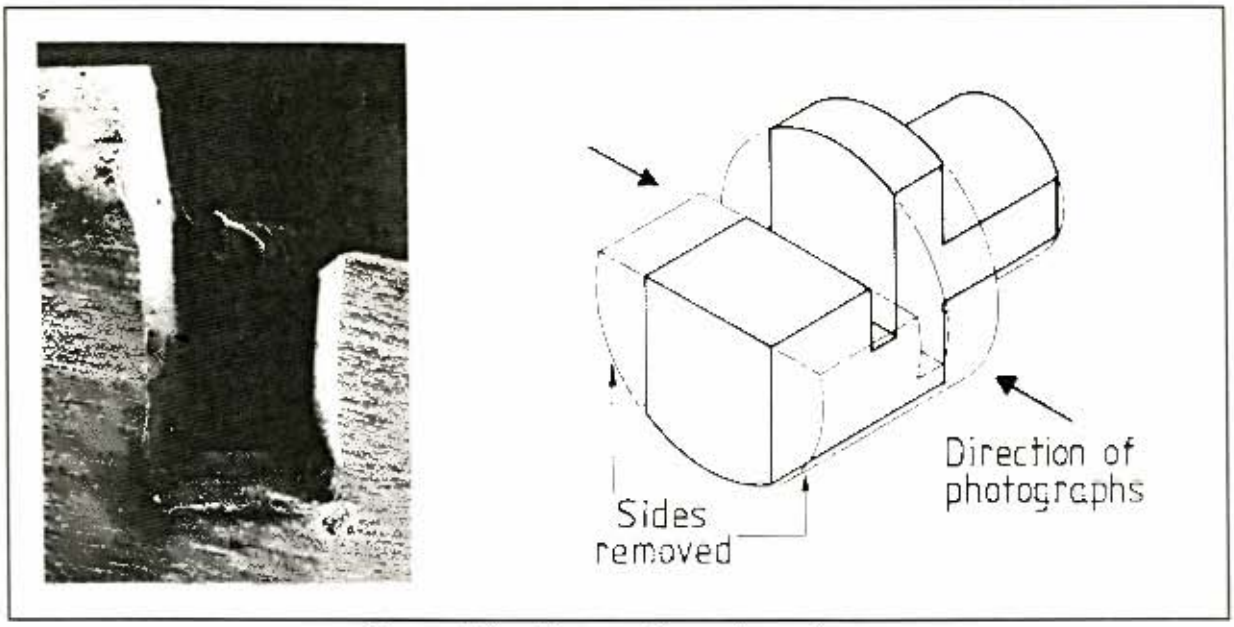

Figure E5: Preparation of specimen

identical magnifications. The photographs were then digitising using a scanner and appropriate software. By counting the digitised pixels of the eroded region, an objective measure of the magnitude of erosion was established. The Damage Intensity (DI) was defined as the mean pixel count from both sides divided by a suitable scaling factor. Using this Damage Intensity, values between 0 and 20 were measured during the test program, which was considered sufficient sensitive for the purposes of this study.

E.2 EXPERIMENTAL METHOD

The control conditions chosen as a result of the initial test phase, are shown in table I. A pressure transducer was fitted in the cylinder-head, adjacent to the specimen cavity, as shown in figure E1.

Under stabilised operating conditions, a digital-audio tape (DAT) recording, with a frequency range up to 20 kHz, was made of the pressure signal. The DAT recording was later down-loaded to an ISC-16 computerscope. The

Table I: Operating conditions

Engine speed, Load		900 rpm, WOT	
Fuel-Air Equivalence Ratio		0.9	
Inlet air temperature		120°C and 165°C	
Fuel	Compression ratio	93 RON	8.5:1
		97 RON	9.7:1
		Methanol	9.5:1
Spark-Timing		10° to 40°CA BTDC	
Test Duration		20 minutes	

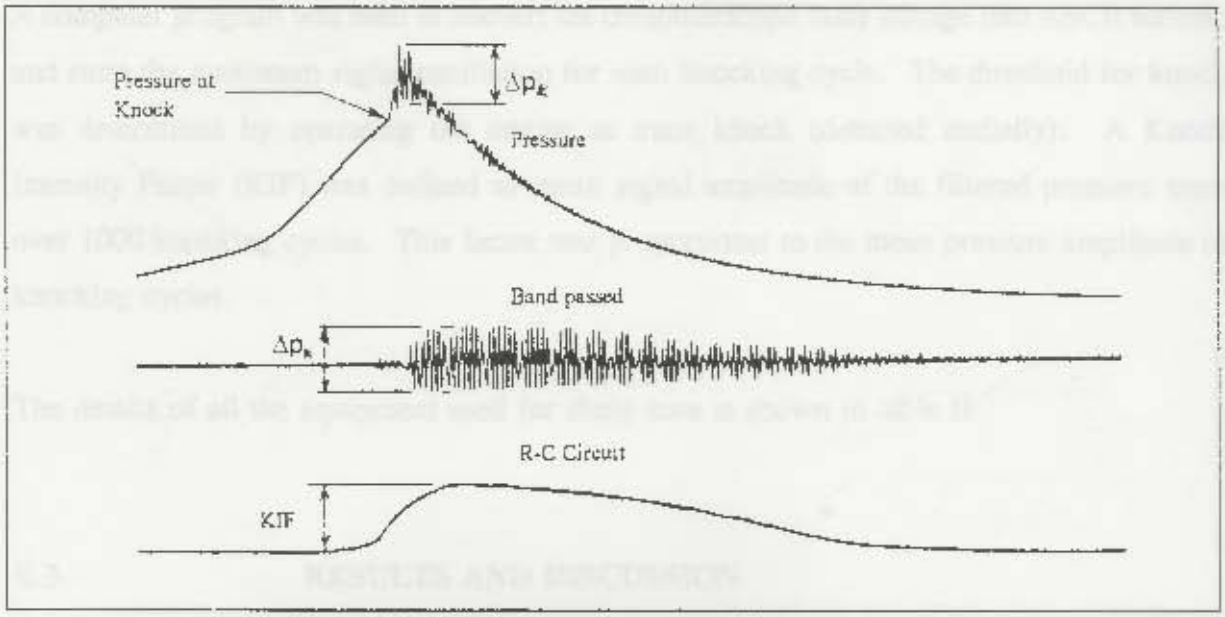

Figure E6: Pressure trace and filtered signals

cylinder pressure at the onset of knock was determined for an average of 100 knocking cycles. The DAT recording was then fed through a bandpass filter and R-C filter to determine a measure of the mean amplitude of the pressure oscillations. Figure E6 shows a typical signal at each stage of processing. The band pass filter was set at filter frequency of 6kHz and bandwidth of 1/3 octave to eliminate the low frequency oscillations. The R-C filter was used as a simple means of determining the maximum signal amplitude. Although the use of this filter precluded the measurement of absolute values, it simplified the data manipulation process.

Table II: Equipment

EQUIPMENT	MAKE/TYPE
Pressure Transducer	AVL 12QP300CV
Charge Amplifier	Kistler Model 568
Crank Angle Indicator	AVL 361 003
Digital Storage Scope	Gould DSO420
DAT Recorder	TEAC CS RD 100T
Computerscope	ISC-16
Band Pass Filter	General Radio 1564A
Exhaust Gas Analyzer	Siemens Ultramat 13M

A computer program was used to convert the computerscope mass storage into ASCII format, and store the maximum signal oscillation for each knocking cycle. The threshold for knock was determined by operating the engine at trace knock (detected audially). A Knock Intensity Factor (KIF) was defined as mean signal amplitude of the filtered pressure trace over 1000 knocking cycles. This factor was proportional to the mean pressure amplitude of knocking cycles.

The details of all the equipment used for these tests is shown in table II:

E.3 RESULTS AND DISCUSSION

This section presents the findings from both the preliminary test phase and the final erosion test data. Discussion of results is limited to the calculations arising out of the test data.

E.3.1 ESTIMATION OF LOCAL CREVICE PRESSURES DURING KNOCK

During the experimental phase of specimen geometry development, some specimens were tested with a front wall thickness of 2mm (compared to the 4 mm finally adopted). After testing under knocking conditions, it was found that the front wall of these specimens had been bent outwards by up to 0.8mm, as shown in figure E7. From considerations of the material properties and the mode of plastic deformation, it was possible to estimate the mean pressure difference across the front wall.

Figure E7: Specimen with bent front wall

Referring to figure E8, the front wall was treated as a simple cantilever with a uniform pressure (p) applied to the inner surface area (A). The moment (M) at the base of this

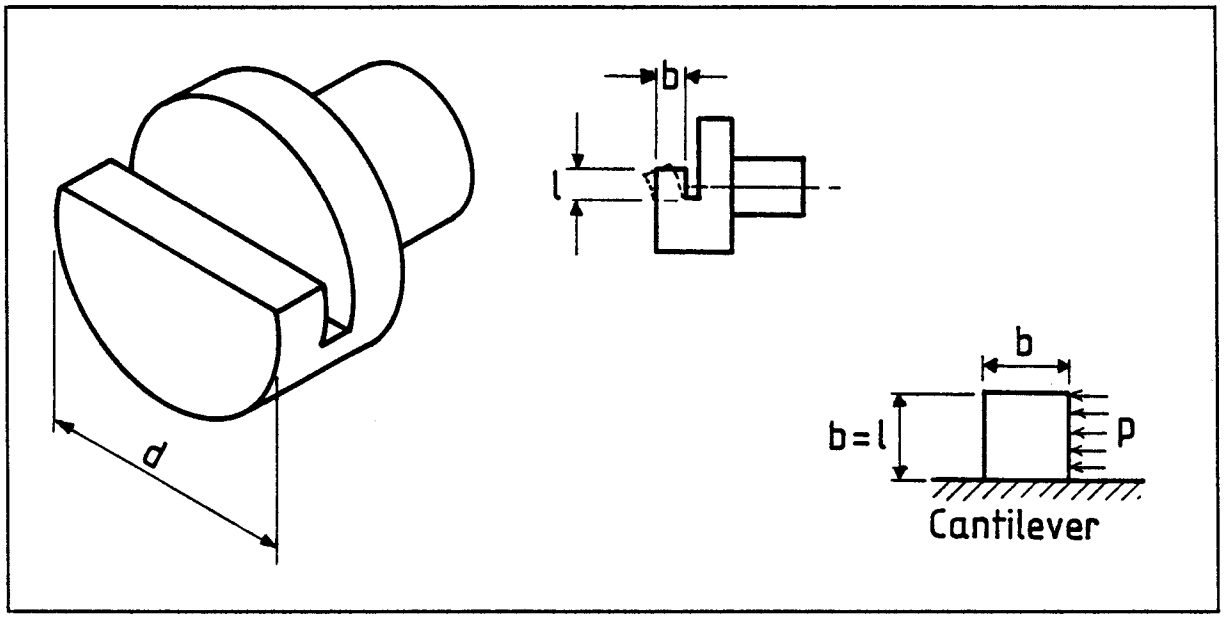

Figure E8: Specimen geometry and deformation

cantilever was described by:

$$M = \frac{pAl}{2} \quad (1)$$

At the point of yield, the moment (M_y) was determined from the yield stress (σ_y) as follows [87]:

$$M_y = \frac{\sigma_y b^2 d}{6}$$

Combining with equation (1), and noting that in this geometry, $b = l$ and $A = ld$, the pressure at the elastic limit (p_y) was calculated:

$$p_y = \frac{\sigma_y}{3} \quad (2)$$

Assuming a constant yield stress (which is an underestimate in the case of aluminium), the moment (M_p) at the point of complete plasticity at the base of the cantilever was determined by [87]:

$$M_p = \frac{\sigma_y b^2 d}{4}$$

The applied pressure (p_p) to produce this conditions was determined by combining with

equation (1) and using the appropriate geometry:

$$p_p = \frac{\sigma_y}{2} \tag{3}$$

Due to the high strain rate of the applied pressure (from the advancing shock wave), the yield stress is effectively increased. The Cowper-Symonds relationship [88] was used to calculate the effective yield stress (σ_{eff}) as a function of strain rate ($\dot{\varepsilon}$):

$$\sigma_{eff} = \sigma_y \left[1 + \left(\frac{\dot{\varepsilon}}{C} \right)^{\frac{1}{4}} \right] \tag{4}$$

where $C = 6500$ for aluminium alloys [88]

An order of magnitude estimate of the strain rate was obtained by assuming that the yield limit was attained within 1 microsecond. This interval approximates the time taken for the passage of a detonating shock across the specimen. The fact that these specimens had sustained permanent plastic deformation indicated that the strain levels were greater than the yield limit, making this a conservative estimate of the strain rate.

Thus, the applied pressures to produce yield or complete plasticity are as follows:

$$p_y = \frac{\sigma_y}{3} \left[1 + \left(\frac{\dot{\varepsilon}}{C} \right)^{\frac{1}{4}} \right]$$

$$p_p = \frac{\sigma_y}{2} \left[1 + \left(\frac{\dot{\varepsilon}}{C} \right)^{\frac{1}{4}} \right]$$

The yield stress for this aluminium alloy is influenced by temperature, as illustrated by the data in figure E9 [74]. A 5th order polynomial curve fit to this data provided the

relationship between yield stress and temperature, which was used to calculate the applied pressure to the inner surface.

Typical operating temperatures for the specimens were determined as described in section E.1.2. Temperatures between 170°C and 210°C were recorded, under various knocking conditions.

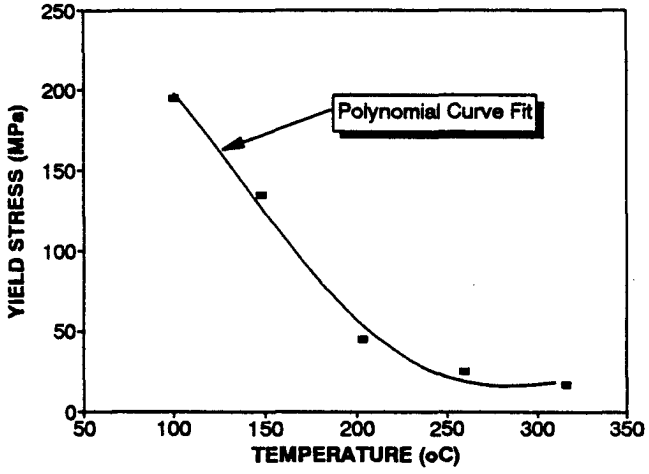

Figure E9: Effect of temperature on yield stress

Figure E10 shows the calculated pressure for either the elastic limit or complete plasticity to be achieved at the base of the cantilever, for a representative range of temperatures.

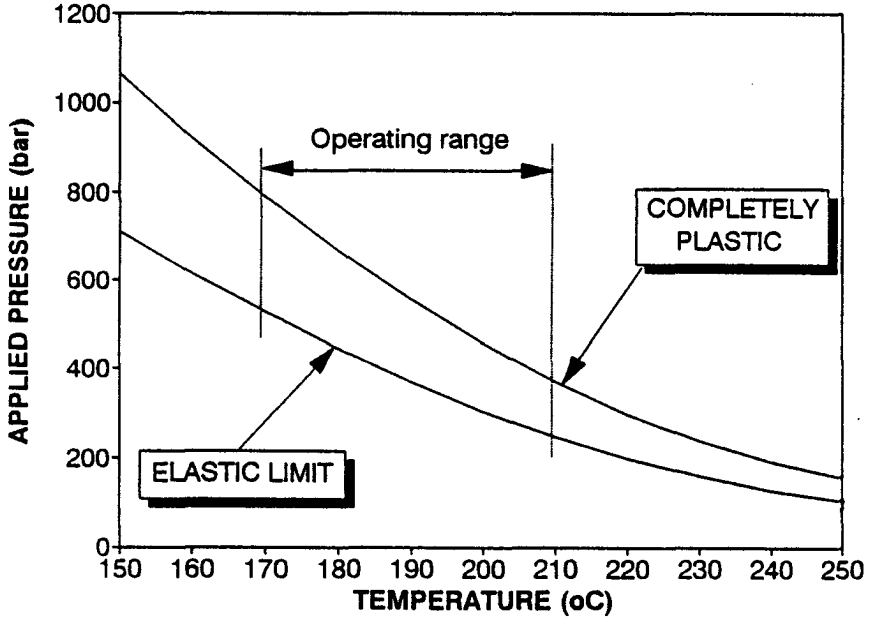

Figure E10: Pressure differential necessary to cause bending

To achieve the elastic limit, pressures of over 250 bar must have occurred. The bending of the specimen, as seen in figure E7 was quite considerable, indicating that conditions closer to complete plasticity had been achieved. Thus it is more probable that pressures of well

over 350 bar (and possibly up to 800 bar) had been achieved in the crevice.

It should be noted that this analysis assumed a uniform pressure distribution over the wall. As this condition is improbable, it was deduced that the local pressures were even greater than those calculated. The assumption of constant yield stress and the value of the strain rate were additional reasons for the calculations to be an under-estimate of the actual pressure peaks. Thus, the analysis has demonstrated the existence of extreme pressures occurring in the end-gas crevice regions. It is possible that the extreme short duration of the pressure pulse, or the very small area over which it applies, is the reason why conventional pressure transducers do not record such high pressure values.

E.3.2 EROSION TEST RESULTS

The erosion tests were performed over a wide range spark-timing settings using 93 RON, 97 RON and methanol. The tests were conducted at identical equivalence ratio, engine speed and wide open throttle. Figure E11 shows the damage intensity as a function of Knock Intensity Factor (equivalent to mean maximum pressure amplitude).

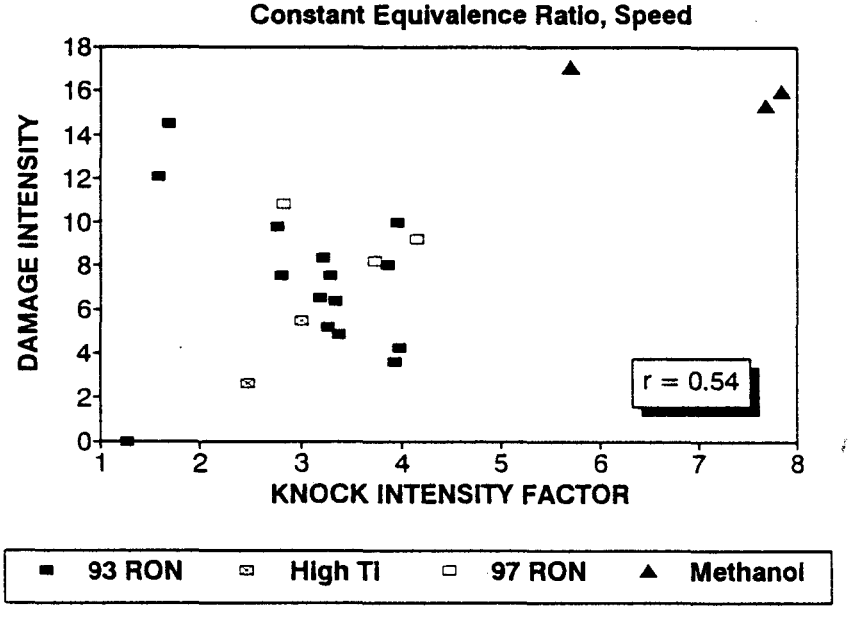

Figure E11: Erosion damage intensity as a function of Knock Intensity Factor

The two data points, indicated in the legend as "High Ti" were performed at an inlet air temperature of 165°C, with 93 RON gasoline. The remainder of the data was tested at an

APPENDIX F: RING GAP INVESTIGATION

The goals of this work were to investigate the magnitude of knock-induced ring gap closure and to identify the correct knock intensity criteria to quantify the process. This study was performed with a combination of analytical and experimental work.

F.1 THEORETICAL DEVELOPMENT

An existing heat transfer model was modified to account for the effect of knock intensity and extended to include the thermal expansion of the ring. From this, a relationship between knock intensity and changes in ring gap was established.

F.1.1 KNOCKING HEAT TRANSFER

A variety of detailed heat transfer models have been debated in the literature [76]. However, the purpose of this analysis was to predict trends and provide a functional relationship, and therefore a simple model was used. Taylor and Toong [75] correlated the overall heat transfer data from many engine tests and operating conditions. They found that these data fitted the general form:

$$Nu = C\, Re^{n} \tag{1}$$

where
- Nu - Nusselt Number
- Re - Reynold's Number
- C, n - constants

The value of the constant "n" has a range of between 0.6 and 0.8, depending on the choice of variables, engine types and conditions [76]. The cylinder bore (B) is usually chosen as the characteristic length, such that:

$$Nu = \frac{h\,B}{k}$$

$$Re = \frac{\rho\, u\, B}{\mu}$$

where	h -	convective heat transfer coefficient
	k -	thermal conductivity of gas
	ρ -	density
	μ -	gas viscosity
	u -	gas velocity

There was a need to account for the effect of various cyclic conditions on the Reynold's Number, or more specifically on the gas velocity. Woschni developed a relationship for the gas velocity (u_w) as a function of piston motion and combustion induced velocities [77], as follows:

$$u_w = 2.28\overline{U}_p + 0.0032\frac{T_o V}{V_o}\frac{\Delta p_c}{p_o}$$

where	U_p -	mean piston speed
	T_o -	temperature at inlet valve closing
	V_o -	cylinder volume at inlet valve closing
	p_o -	pressure at inlet valve closing
	Δp_c -	pressure rise due to combustion
	V -	instantaneous cylinder volume

The first term accounts for the effect of piston motion, while the second term describes the additional contribution of combustion induced gas velocities. The pressure rise due to combustion is defined as the difference in pressure between fired and motored conditions.

With knocking combustion there would exist an additional term in the Woschni equation to describe the gas velocities induced by the pressure waves within the combustion chamber. These velocities are responsible for the knock-induced heat flux, as discussed in chapter 2. This analysis does not include the local heat flux caused by the auto-ignition process, which is confined to the end-gas region. The gas velocity (u) driving the heat transfer was amended to include an additional term (u_k) to describe the knock-induced gas velocities:

$$u = u_w + u_k$$

However, considering the magnitude of the pressure rise rate under knocking conditions, it is expected that:

$$u_k >> u_w$$

This is justified by the significant increase in heat transfer [4,19,45,51] and shock waves occurring under knocking conditions. As a first approximation, the velocity of knock was considered to be the dominant factor in the heat transfer mechanism, such that:

$$u \approx u_k$$

And using equation (1), the Nusselt Number under knocking conditions (Nu_k) is:

$$Nu_k \approx C Re_k^n \qquad (2)$$

where $Re_k = Re_k(u_k)$ Reynold's Number under knocking conditions

Under light knock intensities, only a small portion of the end-gas is involved in the rapid heat release, leaving the core of the gas unaffected. Therefore it was assumed that average conditions are relatively unchanged (with respect to normal combustion). The knocking pressure amplitude (Δp_k) was used to describe the knock-induced gas velocity.

From conservation of energy (and with all else constant), a pressure difference (Δp_k) within a chamber would give rise to a proportionate increase in the kinetic energy of the gas, therefore:

$$u_k^2 \propto \Delta p_k$$

A hypothetical heat transfer coefficient (h_k) describing the additional heat flux due to knock, was developed by combining the previous relationships:

$$h_k \propto (\Delta p_k)^{\frac{n}{2}}$$

Assuming light knock implies that the gas and the coolant temperatures remain approximately constant relative to non-knocking conditions (such as might be obtained with higher octane fuel). Therefore, the temperature rise of the chamber walls ($\Delta T_{internal}$), due to knock alone may be approximated by:

$$\Delta T_{internal} \approx C_1 (\Delta p_k)^{\frac{n}{2}}$$

where C_1 - constant

F.1.2 RING GAP MODEL #1

The ring may be considered to be part of the piston and will experience a temperature rise proportional to the change in the rest of the material. This is justified by the fact that over 60% of the heat flux through the piston passes through the rings [4]. The change in ring gap as a result of this temperature rise may be determined by the thermal expansion coefficient of the ring material:

$$\Delta RG = \alpha \, l \, \Delta T_{ring}$$

where
- ΔRG - change in ring gap
- α - coefficient of thermal expansion of ring
- l - circumferential length of ring
- ΔT_{ring} - change in ring temperature

Thus, by substitution:

$$\Delta RG \approx \alpha l C_1 (\Delta p_k)^{\frac{n}{2}}$$

Grouping the constants together, the relationship between ring gap and knock-induced pressure amplitude (for the effect of knock alone) becomes:

$$\Delta RG \approx C_2 (\Delta p_k)^{\frac{n}{2}}$$

where C_2 - constant

It is assumed that the expansion of the cylinder is negligible. This is justified by the fact that it is materially constrained compared to the free-floating rings and that the additional heat flux due to knock is distributed over the length of the cylinder.

This model was developed with the assumption that the pressure oscillations which drive the heat transfer process occur repeatable (by using the Taylor and Toong equation). However, at light knock conditions, not all the cycles are knocking, and therefore, a method had to be established to account for the non-knocking cycles. A simple approach is to include the zero values (for non-knocking cycles) in the mean pressure amplitude **Knock Intensity (Δp_k) was defined as the mean pressure amplitude of all cycles.** It is emphasised that this knock intensity is by definition a function of the fraction of cycles knocking. A comparison between the experimental data and the model using this Knock Intensity was used to test the accuracy of the relationship.

F.1.3 RING GAP MODEL #2

Another model was developed, by defining a alternate Knock Intensity Index. Under light knocking conditions, it could be argued that only the knocking cycles contribute to the additional heat flux. The knocking heat flux should therefore be a function of both the pressure amplitude of knocking cycles and the fraction of cycles knocking. This is a subtle but fundamental difference to the previous model, which describes the pressure amplitude as a function of the fraction of cycles knocking.

The alternative **Knock Intensity (Δp_{kk}) was defined as the mean pressure amplitude of knocking cycles**, and the model was extended to include a term proportional to the fraction of cycles knocking, to account for their contribution to the heat flux. The only additional data needed for this evaluation is the point above which all cycles knock. Thus the second model developed is as follows:

$$For \quad \Delta p_{kk} \leq \Delta p_{100}: \qquad \Delta RG \approx C_2 (\Delta p_{kk})^{\frac{n}{2}} \left(\frac{\Delta p_{kk}}{\Delta p_{100}}\right)$$

$$and \quad \Delta p_{kk} > \Delta p_{100}: \qquad \Delta RG \approx C_2 (\Delta p_{kk})^{\frac{n}{2}}$$

where Δp_{kk} - mean pressure amplitude for knocking cycles only

Δp_{100} - mean knock pressure amplitude above which 100% of the cycles are knocking.

C_2 - constant

This model is fundamentally different to the first, in that it accounts for the non-knocking cycles by proportionately reducing the heat flux by the fraction of non-knocking cycles. The first model accounts for the non-knocking cycles by proportionately reducing the knock intensity, which does not describe the actual process occurring in an engine.

It is also worth noting that at knock intensities above Δp_{100} the models are the same.

That is: for Δp_k, $\Delta p_{kk} > \Delta p_{100}$: $\Delta p_{kk} = \Delta p_k$

These models represent a simplified attempt at predicting and understanding the general relationship expected in the experimental stage of this study. To have attempted to predict the absolute values of the ring temperatures as a function of knock amplitude would have meant developing a full heat transfer model of the piston-to-ring groove-to-ring heat transfer process, which is beyond the scope of this research. Therefore, the constant (C_2) was not

analysed, but its value was determined by a least squares fit to the experimental data.

F.2 EXPERIMENTAL STUDY OF RING GAP

The aim of this experimentation was to determine the effect of knock intensity on the ring gap in a running engine. To the author's knowledge, this is the first time that this type of measurement has been attempted.

F.2.1 EXPERIMENTAL METHOD

A CFR Waukesha engine was operated at a constant speed of 890 rpm and compression ratio of 7.5:1 under steady-state conditions [78,89]. Oil and coolant temperatures were monitored and held constant.

Using 93 RON fuel, knocking combustion was induced and its intensity varied by means of altering the ignition timing. 102 RON fuel was then tested, so that the effect of spark-advance which itself causes a change in heat flux, could be eliminated. The 102 octane fuel did not knock under any of the operating conditions.

The following equipment was used for data acquisition in these tests:

- AVL 12QP 300cv pressure transducer
- Kistler Model 568 Charge Amplifier
- Gould DSO420 2 Channel digital storage oscilloscope
- TEAC CS RD 100T Digital Audio Tape (DAT) Recorder
- General 1564-A Bandpass Filter
- ISC-16 Computer Scope and data analysis package

The signal from the pressure transducer via the charge amplifier was recorded on the DAT recorder. Simultaneously, the oscilloscope was used to monitor the input signals to the DAT for any indication of transducer failure and for monitoring the operating condition.

At the conclusion of a test, the output from the DAT was fed into the bandpass filter in order

to isolate the knock resonance amplitudes from the low frequency compression-combustion process. The filter was set at the following levels:

- Filtering frequency: 6kHz
- Bandwidth: 1/3 Octave

The signal was then fed into the Computer Scope, from which it was determined whether the cycle had knocked and the maximum knock pressure amplitude for each cycle. The knock amplitude was measured as peak-to-peak values.

A methodology for measuring the steady state ring gap was developed. Initially, it was hoped to use an electronic transducer which would have required only a single fitting for the duration of the tests. However, due to the harsh operating environment and sensitivity of the measurement required, nothing suitable could be found.

A mechanical system was developed which necessitated the removal of the piston between each test run. The ends of the top compression rings were machined into sharp scribes. An aluminium plate (0.9 mm thick) was placed behind the scribes as shown schematically in figure F1. A curved spring steel plate was placed behind the aluminium plate, inside the ring groove so as to force the plate against the scribes.

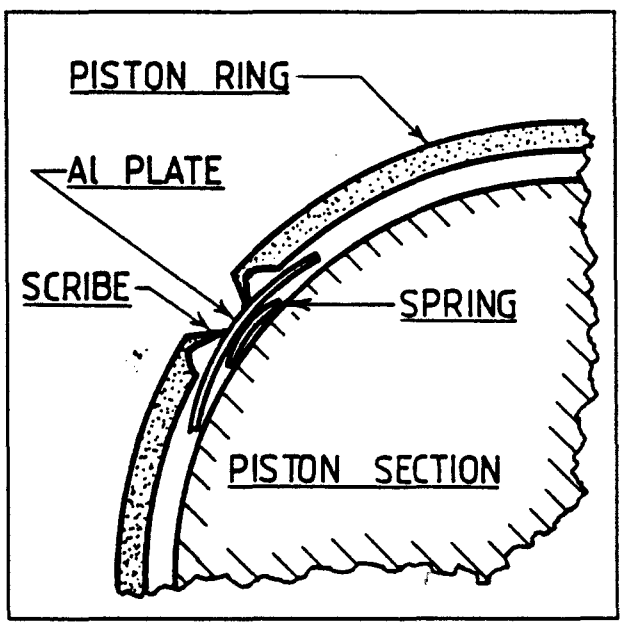

Figure F1: Section through piston showing ring gap measurement system

During engine operation, the ring gap reduced (due to thermal expansion) causing two witness marks to be made on the aluminium by the scribes. After completion of a test run, the plate was removed and the minimum ring gap was measured using a Vicker's graduated microscope. A typical aluminium plate with scribe marks is shown in figure F2. The installation of the modified ring, plate and spring had to be performed with great care, so as to avoid causing spurious marks to occur during the fitting. Many had to be rejected

due to the specimen and spring moving away from the ring gap during operation. It was found impossible to use this method at high knock intensities, as the vibration due to heavier knock caused the specimen to be dislodged. However, sufficient data was recorded at lower knock intensities to make this method worthwhile.

To provide validation of the accuracy of the experimental procedure, the ring temperature was measured under test conditions. A 1.5 mm hole was bored through the centre of the first ring groove, on the thrust side of the piston. The hole was counterbored on the outside of the piston. A type-K thermocouple was fed through the hole (from the inside of the piston) and cemented in place with high temperature epoxy. The counterbored section of the hole provided a key against the high pressure gases. On fitting the ring, the end of the thermocouple was jammed between the ring and groove, thus it was expected to give an indication of the changes in ring temperature, and not the absolute values. The thermocouple wire was led onto the connecting rod and then out of the crankcase using 4-bar linkage designed for this purpose.

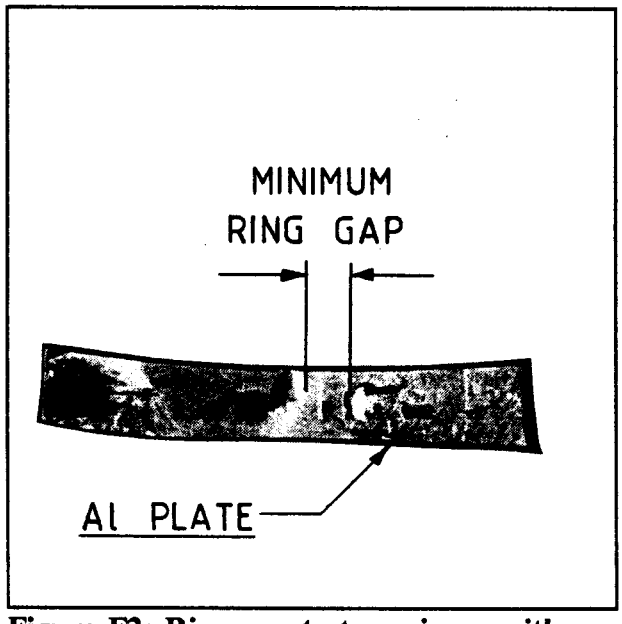

Figure F2: Ring gap test specimen with witness marks

The test procedure commenced with the removal of the piston and the fitting of the ring gap specimen plate. The piston was carefully installed, the temperature linkage reconnected and the engine run up to its operating conditions. It was intended that the ring temperature would also be used as an indication that steady state conditions had been achieved. However, in many cases the thermocouple wire did not last the duration of the test, as the repeated bending caused the wire to break. Subsequently, the coolant temperature was used as the indicator of steady state conditions. During the test, the a DAT recording was made of the pressure trace. At the conclusion, the piston was removed, the ring gap specimen examined and the rest of the analysis performed, as discussed above.

F.2.2 RESULTS AND DISCUSSION

The relationship between ring gap and spark timing is shown graphically in figure F3. The gap measurement using the Vicker's microscope system could be read with increments of 0.025 mm and therefore the maximum error was 0.0125 mm. Spark timing measurement was estimated to have a maximum error of about 0.5 °CA.

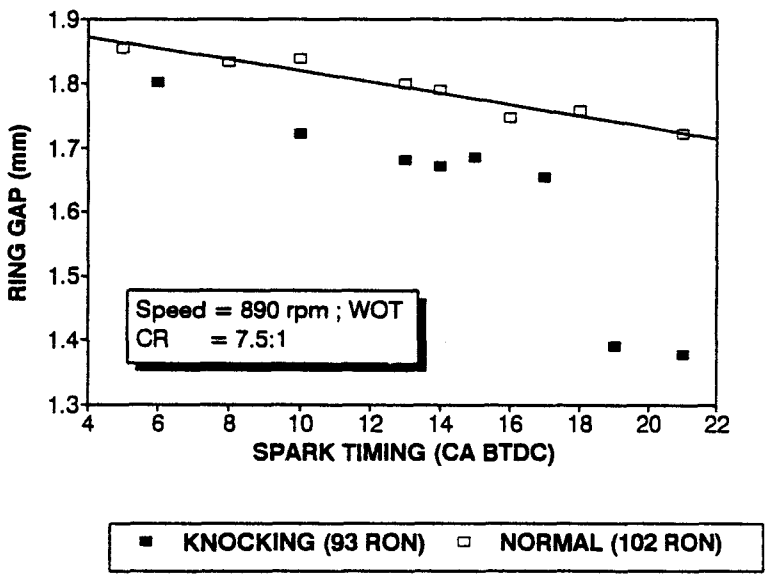

Figure F3: Ring gap measurements

The objective of this work was to investigate changes in ring gap due to knock alone. The knock intensity was varied by means of spark timing, and the effect of the spark timing on ring gap is seen in the non-knocking data in figure F3. To determine the effect of knock alone, the data from non-knock conditions was subtracted from the knocking data. A linear regression was applied to the non-knocking data which was found to have a correlation coefficient of 0.97. The values using this regression line were then subtracted from the knocking data, to determine the effect of knock alone on ring gap.

Figure F4 shows the change in ring gap plotted against the knock intensity defined as the mean pressure amplitude of all cycles. The theoretical curves in this figure corresponds to the first model which has been plotted for the extremities of the exponent n. For each value of the exponent, a least squares fit was performed to estimate the constant C_2.

F.2.2 RESULTS AND DISCUSSION

The relationship between ring gap and spark timing is shown graphically in figure F3. The gap measurement using the Vicker's microscope system could be read with increments of 0.025 mm and therefore the maximum error was 0.0125 mm. Spark timing measurement was estimated to have a maximum error of about 0.5 °CA.

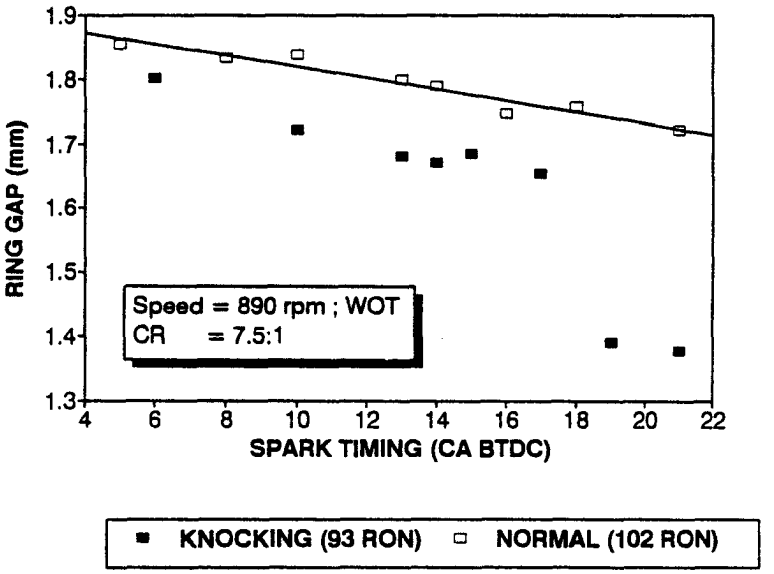

Figure F3: Ring gap measurements

The objective of this work was to investigate changes in ring gap due to knock alone. The knock intensity was varied by means of spark timing, and the effect of the spark timing on ring gap is seen in the non-knocking data in figure F3. To determine the effect of knock alone, the data from non-knock conditions was subtracted from the knocking data. A linear regression was applied to the non-knocking data which was found to have a correlation coefficient of 0.97. The values using this regression line were then subtracted from the knocking data, to determine the effect of knock alone on ring gap.

Figure F4 shows the change in ring gap plotted against the knock intensity defined as the mean pressure amplitude of all cycles. The theoretical curves in this figure corresponds to the first model which has been plotted for the extremities of the exponent n. For each value of the exponent, a least squares fit was performed to estimate the constant C_2.

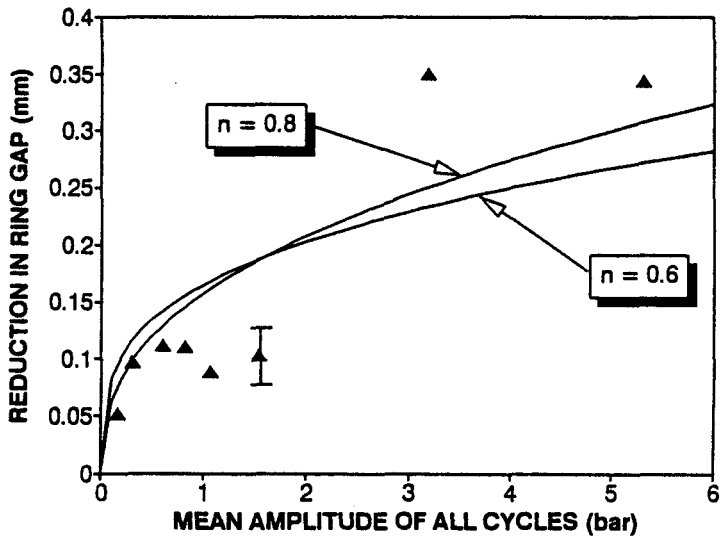

Figure F4: Experimental and Theoretical results based on mean pressure amplitude of all cycles

As discussed previously, the error in the ring gap measurement was about 0.0125 mm, and the uncertainty of the regression line amounts to 0.013 mm (as described by one standard deviation). Thus the total estimated error in these ring gap data amounts to 0.0255 mm. It is estimated that the knock pressure amplitude measurement had an accuracy of about 0.2 bar, due to the digitization process and the sensitivity of the pressure transducer and filtering equipment. The range of these error estimates is given in figure F4.

The second model was tested by plotting the ring gap data against the alternative knock intensity defined as the mean pressure amplitude of knocking cycles, as shown in figure F5. The theoretical curves in this figure corresponds to the model based on this definition of knock intensity. Experimentally, it was found that: $\Delta p_{100} = 5.3$ bar, which is the knock intensity above which all cycles were knocking. The modelled relationships were again plotted for the extremities of the exponent n, and a least squares fit was performed to estimate the constant C_2, for each of the exponents.

Figure F6 shows the measured relationship between ring gap (RG) and ring temperature (T_{ring}). A typical value for the coefficient of thermal expansion for ring material is given as 12.2 10^{-6} in this temperature range [79]. The expected slope that would be produced by this

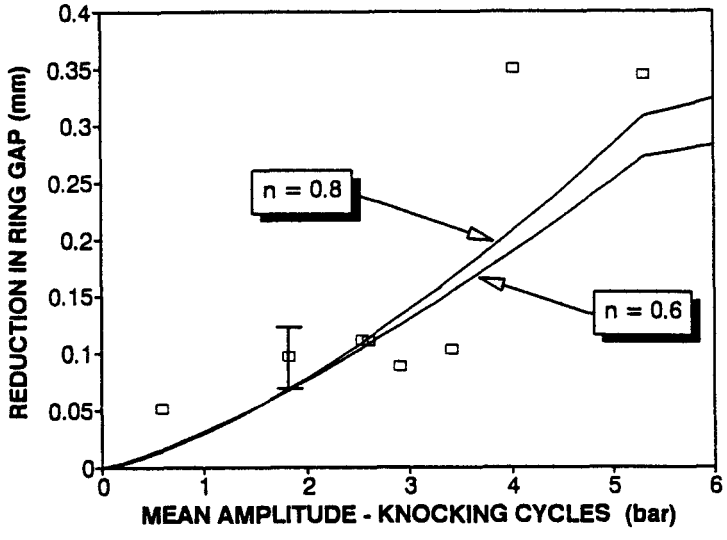

Figure F5: Experimental and Theoretical results based on mean pressure amplitude of knocking cycles alone

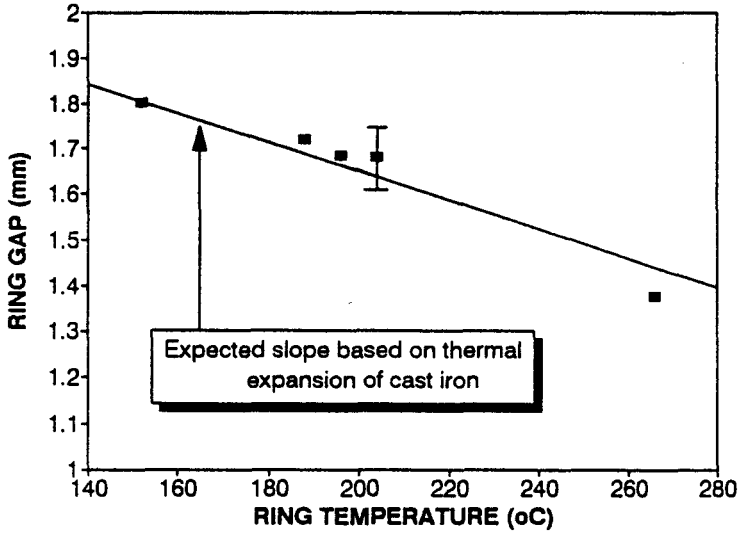

Figure F6: Relationship between ring gap and temperature

material is plotted in the figure and is not significantly different from the experimental data. The proximity of the data to the expected line is an independent confirmation of the accuracy of the ring gap measurement procedure.

APPENDIX G: RING SEIZURE AND YIELD

The objective of this study was to determine the effect of ring temperature on circumferential yield of a piston ring, after total ring gap closure. Both theoretical and experimental approaches are detailed in this appendix.

G.1 THEORETICAL ANALYSIS

At the point of total gap closure, the compression ring constitutes a solid ring confined by the bore. Under these conditions, the ring would be expected to seize in the bore and its temperature would rise rapidly, due to friction. Commensurate with the temperature increase, the ring would experience a compressive stress caused by the further thermal expansion of the ring and the confinement by the bore.

In contrast to the ring, the cylinder which is cooled externally, would experience only a minor temperature increase as the heat flux from the seizing ring is spread over the entire length of the bore. This means that the bore experiences negligible thermal expansion, and for the purposes of this analysis, the change in bore dimensions will be ignored.

To model this process, the ring may be thought of as a compression strut being completely constrained at its ends. As a consequence, a temperature increase would result in a thermal compression strain to be developed in the ring.

The compressive strain (ε) may be determined by:

$$\varepsilon = \alpha \, \Delta T$$

where α - coefficient of expansion (1/°C)

ΔT - temperature increase above the point of gap closure (°C)

A simple stress-strain relationship was assumed for the ring material, in the form of a linear

elastic region, followed by a constant yield stress to failure:

$$\sigma = E.\varepsilon \qquad for\ \sigma \leq \sigma_y$$

$$\sigma = \sigma_y \qquad for\ \sigma > \sigma_y$$

where σ - applied stress (MPa)

σ_y - yield stress (Mpa)

E - elastic modulus (Mpa)

Considering the ring at a temperatures above the point of gap closure, if the thermal stress rises into the plastic region, the ring would yield circumferentially (or in the case of the hypothetical strut, longitudinal). This permanent plastic strain (ε_p) was determined by the difference between the total thermal strain and the maximum permissible elastic strain as follow:

$$\varepsilon_p = \alpha \Delta T - \frac{\sigma_y}{E}$$

G.2 EXPERIMENTAL STUDY OF RING YIELD

These experiments were aimed at measuring the plastic yield of a ring as a function of ring temperature under simulated seizure conditions.

G.2.1 EXPERIMENTAL METHOD 1

A test rig was developed comprising of a water cooled cylinder and a gas burner, shown in figure G1. A standard compression ring was fitted into the cylinder, the ring gap was measured and the gap was then blocked by means of an adjustable wedge, shown in figure G2. The lock nuts on the wedge were made only "finger tight" so as not to impose any pre-stress on the ring. Dimensions were chosen such that the gas flame was focused on the ring (and not the bore). The ring was heated to the test temperature, as monitored by

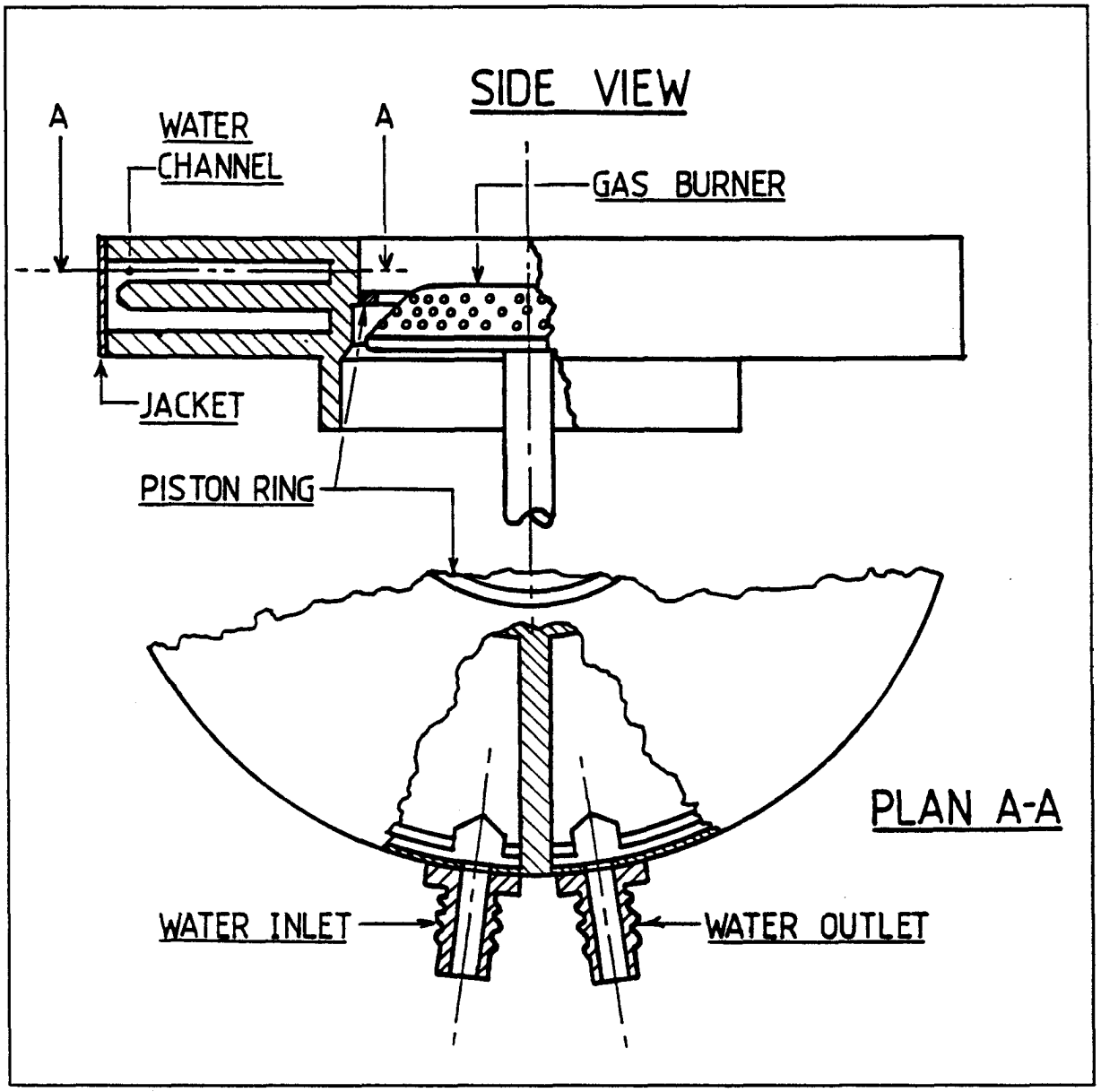

Figure G1: Burner apparatus

thermocouples. To minimise dimensional changes in the bore, a large diameter cooling fin was placed at the point at which the ring was positioned, also shown in figure G1. At the conclusion of a 10 minute soak at the chosen temperature, the gas flow was shut off and the rig allowed to cool to the starting temperature. The adjustable wedge was removed and the ring gap measured by means of a digital internal-vernier with accuracy of 0.005 mm. The difference between the ring gap at the start and completion of the test constituted the permanent plastic deformation. Together with the knowledge of the circumferential length of the ring, the plastic strain was determined, as follows:

$$\varepsilon_p = \frac{\Delta RG}{\pi d_o - RG_o}$$

where ΔRG - change in ring gap (mm)

d_o - bore diameter at initial temperature (mm)

RG_o - initial ring gap (mm)

The accuracy of the digital internal vernier used to make these measurements was within 0.005 mm. Converting this to an error in the strain measurement for this experiment amounts to $\Delta\varepsilon_p = 0.023\ 10^{-3}$. This error is about 4% of the maximum values measured.

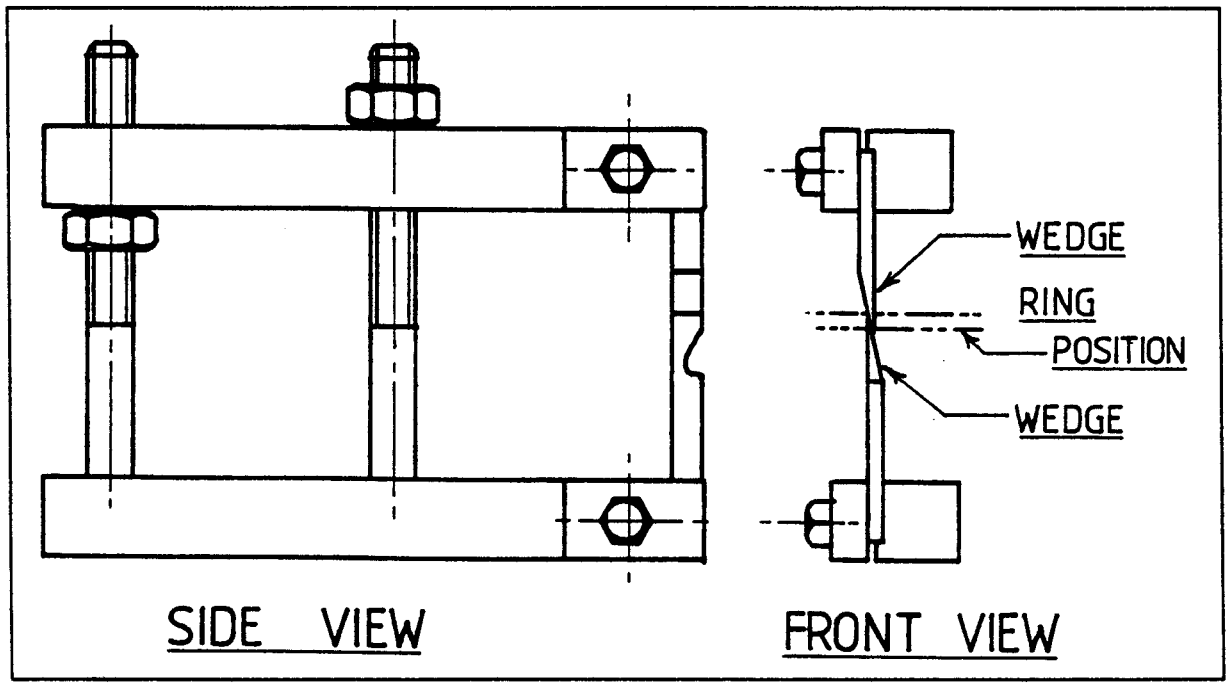

Figure G2: Adjustable wedge to close ring gap

Each ring tested was instrumented with 3 thermocouples placed at equidistant points around the circumference. The thermocouple junction was made up of two 0.3mm holes bored through the width of the ring and then counterbored to 0.8mm to half the width of the ring. The thermocouple wires were led through the holes and silver soldered to the underside. This allowed a mean cross-sectional temperature to be measured.

The standard rings chosen for this study were from a standard 4-cylinder 1 litre engine, with

nominal dimensions 3 mm wide by 1.6 mm thick fitted into a bore of 70 mm diameter. A spigot was manufactured and used to fit the ring into the cylinder, such that each ring was positioned horizontally at the same position in the bore. After each test the diameter of the cylinder was checked to ensure that no dimensional change had occurred.

Test were performed on 18 rings over a temperature range of 200°C to 420°C. The temperature of the water outlet was maintained at 40°C throughout the tests. The ambient temperature at which the initial ring gap (RG_o) was measured varied between 23°C and 24°C.

This experiment could not be performed at ring temperatures above 420°C owing to the limited heat produced by the flame and the high heat flux to the cooling water. Because it was considered that the ring seizure conditions would cause ring temperatures above 420°C, a second test procedure was developed to investigate this temperature range.

G.2.2 EXPERIMENTAL METHOD 2

This test procedure induced circumferential stresses in the ring by means of shrink-fitting an oversize ring into an undersize cylinder. The stress was applied at elevated temperatures to conform to the ring seizure condition. A control cylinder was manufactured with diameter 94 mm. A test cylinder was produced from mild steel with an internal diameter of 93.1 mm, outer diameter of 140mm and height of 30mm, as shown in figure G3. The one end of the test cylinder was machined with a 10° taper and a hole was drilled into the outer surface for the placement of a thermocouple. A piston with a ring groove was manufactured from mild steel to fit into the test cylinder.

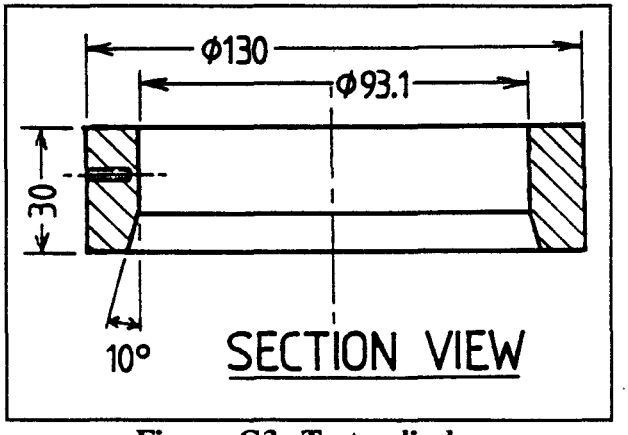

Figure G3: Test cylinder

The test procedure commenced with the measurement of the ring gap in the control cylinder and then the ring was fitted onto the piston. After heating the test cylinder in a furnace to

about 800°C, the cold piston-ring assembly was fitted into the cylinder and placed back into the furnace at the same temperature. The taper in the bore permitted the quick insertion of the piston and ring into the cylinder. After soaking the assembly at about 800°C for 10 minutes, the temperature was gradually reduced to the chosen test temperature (between 450°C and 750°C) by monitoring the thermocouple placed in the side of the cylinder and lead out of the furnace. At the high temperature conditions, hoop stresses would be induced in the ring (due to the closure of the ring gap at high temperatures) equivalent to that produced in a burner experiment operating at the same temperature. The manner in which this equivalence was achieved is detailed in what follows. After soaking at the test condition for 10 minutes, the temperature was raised again to about 800°C, the system removed from the furnace and the piston-ring assembly quickly extracted from the cylinder. On cooling to ambient conditions, the ring gap was again measured in the control cylinder and the difference in ring gap converted to plastic strain (in the same manner as used in the burner tests).

The coefficient of thermal expansion of the mild steel is greater than that of the cast iron ring. Therefore, as the temperature is increased the diameter of the bore increases at a greater rate than that of the ring, thereby reducing the circumferential strain. Conversely, as the temperature is lowered, greater hoop stresses would be induced in the ring. It was the objective of these tests to provide comparative data for the burner tests over a higher temperature range. For each test performed the initial ring gap had to carefully matched to correspond to the correct test temperature. The following analysis develops this relationship between initial ring gap and test temperature.

A piston ring is fitted into the control cylinder of diameter d_* at ambient temperature T_o. By measuring the initial ring gap RG_*, the circumferential length of the ring l_{ro} is:

$$l_{ro} = \pi d_* - RG_*$$

Now consider the test cylinder with diameter d_o at ambient temperature (where $d_o < d_*$). The perimeter length of the bore, l_{bo} is:

$$l_{bo} = \pi d_o$$

Hypothetically, if the ring were fitted into this cold test cylinder, then the ring gap RG_o

would be a negative value (interference) due to the smaller diameter of this cylinder relative to the test cylinder:

$$RG_o = l_{bo} - l_{ro} \qquad where \quad RG_o < 0$$

As the temperature of the test cylinder is raised above T_o to a value of T, the length of the ring and the perimeter length of the bore will increase by an amount described by the coefficients of expansion of each material and the temperature change $\Delta T = T - T_o$ as follows:

$$\begin{aligned} l_b &= l_{bo}(1 + \alpha_b \Delta T) \\ l_r &= l_{ro}(1 + \alpha_r \Delta T) \end{aligned} \qquad (1)$$

where
- l_b - perimeter length of test cylinder at temperature T
- l_r - circumferential length of ring at temperature T
- α_b - coefficient of expansion of the cylinder
- α_r - coefficient of expansion of the ring

Consequently the ring gap RG at the test temperature T may be determined from the difference between these two lengths:

$$RG = l_b - l_r$$

$$\therefore \quad RG = RG_o + (l_{bo}\alpha_b - l_{ro}\alpha_r)\Delta T$$

This may be approximate for convenience with only a small loss of accuracy as follows:

$$RG \approx RG_o + l_{bo}(\alpha_b - \alpha_r)\Delta T \qquad (2)$$

For comparative experiments at test temperature T, the applied stains in both experiments must be equal. In the gas burner tests, all the strain is derived from the thermal expansion of the ring held in a constant diameter bore. For the shrink fit method, the strain is derived from the difference in thermal expansion between the ring and cylinder, as well as the strain due to the interference fit (produced by the correct choice of dimensions). Equating the two processes yields:

$$[\alpha_r \Delta T]_{burner} = \left[(\alpha_b - \alpha_r)\Delta T - \frac{RG}{l_r}\right]_{shrink}$$

Substituting equation (1) for l_r and equation (2) for RG and solving for the interference ring gap RG_o at T_o yields:

$$RG_o \approx -(2\alpha_r - \alpha_b)(1 + \alpha_r \Delta T)\, l_{ro} \Delta T - l_{bo}(\alpha_b - \alpha_r)\Delta T \qquad (3)$$

The ring gap in the test cylinder and that of the control cylinder may now be related by means of the dimensions at T_o:

$$RG_o = l_{bo} - l_{ro} = \pi d_o - (\pi d_* - RG_*)$$

$$\therefore RG_* = \pi(d_* - d_o) + RG_o \qquad (4)$$

Finally the unique ring gap in the control bore RG_* may be related to the specific test temperature T to provide a condition similar to that produced in the gas burner experiment (assuming both are started at the same initial temperature T_o. This is done by combining equations (3) and (4):

$$RG_* \approx \pi(d_* - d_o) - (2\alpha_r - \alpha_b)(1 + \alpha_r \Delta T) l_{ro} \Delta T - l_{bo}(\alpha_b - \alpha_r)\Delta T$$

This may be simplified with another small loss in accuracy as follows:

$$\boxed{RG_* \approx \pi(d_* - d_o) - \pi d_o[(2\alpha_r - \alpha_b)(1 + \alpha_r \Delta T)\Delta T - (\alpha_b - \alpha_r)\Delta T]}$$

The values used for coefficients of thermal expansion for mild steel (α_b) and cast iron (α_r) were 14.4 10^{-6} and 12.2 10^{-6} respectively [74]

This relationship was used to determine the appropriate initial ring gap and test temperature combination for each test. The approach used was to choose a test temperature and compute the initial ring gap in the control cylinder (using the above relationship). A ring was placed in the control cylinder, its ring gap measured and then adjusted by filing the ends to the

appropriate value. Complete accuracy in achieving the desired ring gap was not possible. However, once the ring gap was close to the desired value, the measured ring gap was used as a means of determining the appropriate test temperature. This was achieved by applying a Newton-Raphson iteration to the above equation and solving for ΔT. By this process each test condition was established. It must be noted that in some cases the exact temperature was not achieved, but the error was less than 20°C.

The error in ring gap measurement amounts to $\Delta\varepsilon_p = 0.02\ 10^{-3}$, which is less than 0.5% of the maximum values measured.

G.3 RESULTS AND DISCUSSION

Having performed two equivalent test procedures it was now possible to plot these data over the whole temperature range tested. Figure G4 shows these data together with the theoretical prediction discussed in section G.1.

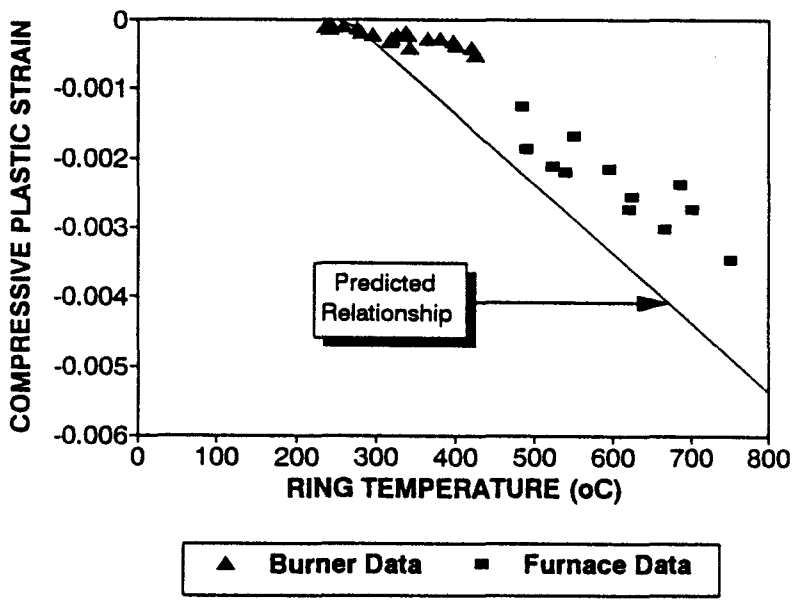

Figure G4: Plastic strain vs test temperature

The graph shows the permanent circumferential strain in the ring due to temperatures elevated above that causing complete ring gap closure. It is seen that, in general, the experimentally measured plastic strain is less than the predicted values, although the general

trend is confirmed. The discrepancy between the experimental data and the predicted relationship was later found to be caused by free-graphite spheroidization of the cast iron at the elevated temperatures. This aspect is dealt with in Appendix H.

Another factor that contributes to the discrepancy between theory and data is the stress-strain relationship used for the model. It was assumed that the yield stress is constant at strains higher than the yield point. This is not strictly true for cast iron and in fact the yield stress continues to rise above the yield point. This would have the effect of reducing the amount of plastic strain incurred.

The most significant fact shown in these test results (seen in figure G4) is the extent of permanent plastic strain. At 700°C a permanent strain of about 0.0035 was measured. For an automotive piston of bore 90 mm, this constitutes a permanent increase in the ring gap of 1 mm.

APPENDIX H: RING GROWTH

This appendix covers various details concerning the lateral ring growth investigation, discussed in section 5.3. These items all contribute towards an understanding of the mechanism by which rings are jammed in their ring grooves.

H.1 POISSON EFFECT

In the case of piston specimen #6, it was observed that the ring gap had increased and the ring had jammed in the ring groove. The following calculation determined the magnitude of lateral ring growth which could be expected from the Poisson effect alone.

A typical value of the Poisson ratio for cast iron rings is 0.25 [90]. Measured data from the specimen #6 case study were:

Bore diameter	=	95 mm
Ring thickness	=	2 mm
Change in ring gap	=	1.2 mm

The Poisson ratio (μ) is defined by the ratio between lateral and longitudinal strain as follows:

$$\mu = \frac{\varepsilon_{lat}}{\varepsilon_{long}}$$

where: ε_{lat} is lateral strain

ε_{long} is longitudinal strain

from the above data:

$$\varepsilon_{long} = \frac{1.2\,mm}{\pi\ 95\,mm} = 0.004$$

therefore:

$$\epsilon_{lat} = 0.25 \times 0.004 = 0.001$$

and thus the increase in ring thickness (lateral growth):

$$\delta x = 2mm \times 0.001 = 0.002\ mm$$

It was apparent that this small amount of growth cannot cause the jamming of rings in their grooves, given typical ring-groove side clearance values of 0.02mm to 0.1mm [81]. It was therefore concluded that the Poisson effect was not responsible for this damage.

H.2 SPECIMEN #6 EXAMINATION

A material examination was carried out on both compression rings from specimen #6 as well as new rings for the same piston, which served as a control. Dimensions were checked, Vicker's Hardness test were made and the microstructures examined. The Vicker's hardness was measured using the 55° diamond indentation at a force of 30 kgf. The measurements yielded the following data:

SPECIMEN	DIMENSIONS (mm)		HARDNESS
	Width	Thickness	(Vicker's)
Top Ring	4.20	1.90	325
2nd Ring	3.98	1.79	287
Control	3.80	1.7	219

Increases in both the lateral dimensions and hardness were evident from these data. The top ring width and thickness had increased by 10.5% and 11.7% respectively. The second ring showed smaller increases of 4.7% and 5.3%. It was deduced that if the growth was a thermal phenomenon, it could be expected that the top ring would show a larger growth than the second ring, as it had operated at higher temperatures [4]. Correspondingly, the hardness measurements showed a progressive increase from the new to the specimen top ring.

The specimen #6 rings as well as the control rings were examined under a microscope at

various magnifications. Examples of the microstructure for a each ring are shown in figures H1, H2 and H3.

Figure H1: Control ring (200X magnification)

The dark lines seen in these photographs are flake graphite in pearlite, while the dark blotches are spheroidal free graphite. Comparing these three photographs, it is seen that the control ring possesses a small amount of spheroidal graphite relative to the specimen #6 rings. Spheroidal deposits in the top ring were typically 40μm in diameter, while those in the 2nd ring were below 30μm.

It was also observed that the length of the graphite flakes had decreased from about 70μm in the control ring to 50μm in the top ring. In summary, these observations show a progressive increase in the amount of spheroidal graphite, accompanied by a reduction in flake graphite.

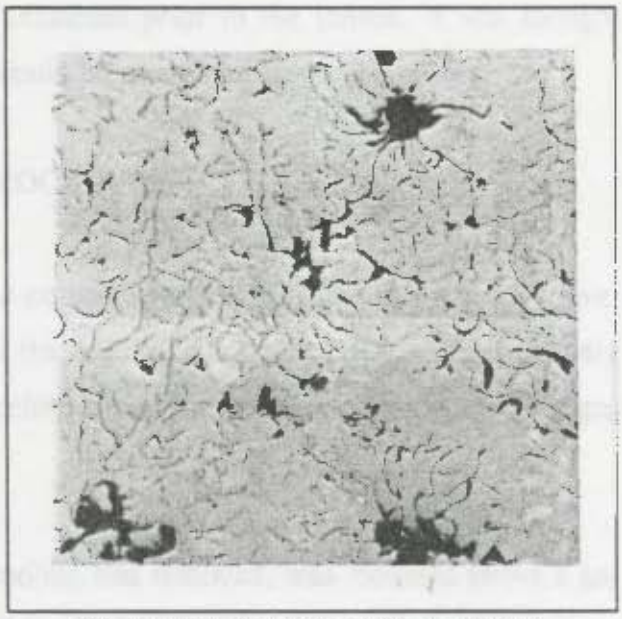

Figure H2: Specimen #6 2nd ring (200X magnification)

Angus [79] reported that permanent dimensional growth occurs in grey cast iron at temperatures above 350°C, by the process of spheroidization. This growth is caused by the breakdown of combined graphite and pearlite into spheroidal free graphite, and is proportional to the carbon content of the cast iron. Furthermore, it is reported that an attendant increase in hardness is found with increased levels of spheroidization. From this description it is inferred that the final condition of the specimen #6 rings was due to spheroidization of the graphite. The dimensional growth, increase in

hardness and observations of the microstructure all conform to the changes associated with this phenomenon.

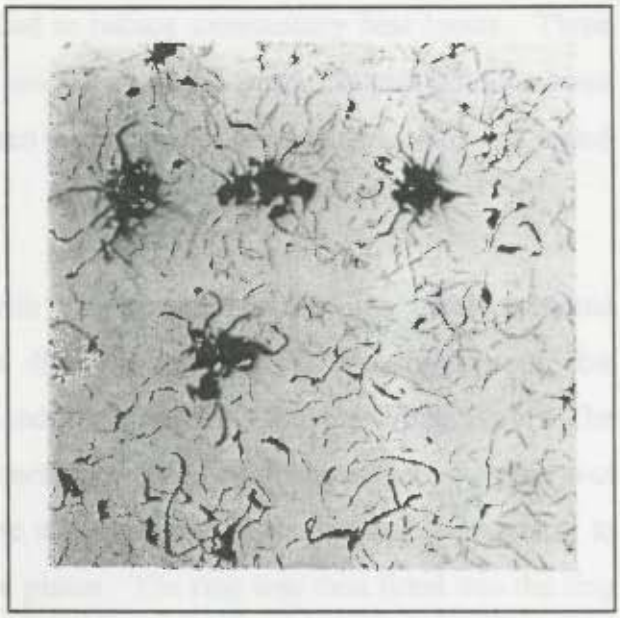

Figure H3: Specimen #6 top ring (200X magnification)

H.3 RING GROWTH EXPERIMENT

Because the case study rings had not been examined prior to the failure, it was thought necessary to investigate whether the change could be re-created in the laboratory.

H.3.1 EXPERIMENTAL PROCEDURE

An experimental apparatus was constructed to expose piston rings, fitted into a ring groove, to elevated temperatures. It was expected that the spherodization process would be relatively independent of any applied stresses, and therefore it was unnecessary to cause the ring gap to close completely in these experiments.

A cylinder from an air cooled engine, with cooling fins removed, was mounted above a gas burner. A piston was machined to remove all material below the second ring and was fitted into the bore with the top ring in place. The relevant specifications of this assembly are as follows:

Engine Type:	Volkswagen 1.91 litre, 4-cylinder
Bore:	94 mm
Ring X-Section:	3.8mm X 1.46mm
Ring-groove Clearance:	0.07 mm

The entire assembly was appropriately insulated to reduce unnecessary heat losses. Three holes were drilled through the bore so as to allow the fitting of thermocouples onto the outer surfaces of the ring. The remaining gap between the holes and thermocouple wire was sealed using a high temperature sealant.

The experimental procedure commenced with the measurement of the cross sectional dimensions of a new piston ring, using a digital micrometer. The average of five measurements along the ring was recorded and corrected for ambient temperature. The Vicker's hardness was measured, and the average of three readings around the ring was recorded. The width of the ring groove on the modified piston was checked as standard, to ensure that previous tests had not damaged the piston. The ring was then fitted into the ring groove and the piston assembly fitted into the bore, above the burner. The temperatures were monitored and the throttle adjusted to attain a constant soak temperature, ranging from 280°C to 600°C. After soaking the specimen for an hour the throttle was slowly closed so as to achieve a cooling period of around 15 minutes. Once the ring had cooled to the ambient temperature it was removed from the apparatus and the initial measurements were repeated.

H.3.2 RESULTS

It was found that for three tests at temperatures below 315°C, the rings were not jammed in their grooves. Furthermore, no significant changes were observed in their dimensions, hardness and microstructure.

In tests at temperatures above 350°C, the rings were found to be jammed in the ring groove. In three tests performed at the highest temperatures, the piston material had to be machined away to release the rings. This experience indicated the extent of the interference fit between ring and groove, after the high temperature exposure.

The results of the ring growth tests are shown in figure H4, in which a linear regression has been performed on the data to show the general trend. It is seen that a lateral growth of between 11% and 18% was measured for temperatures above 350°C. The growth was seen to be fairly insensitive to temperature.

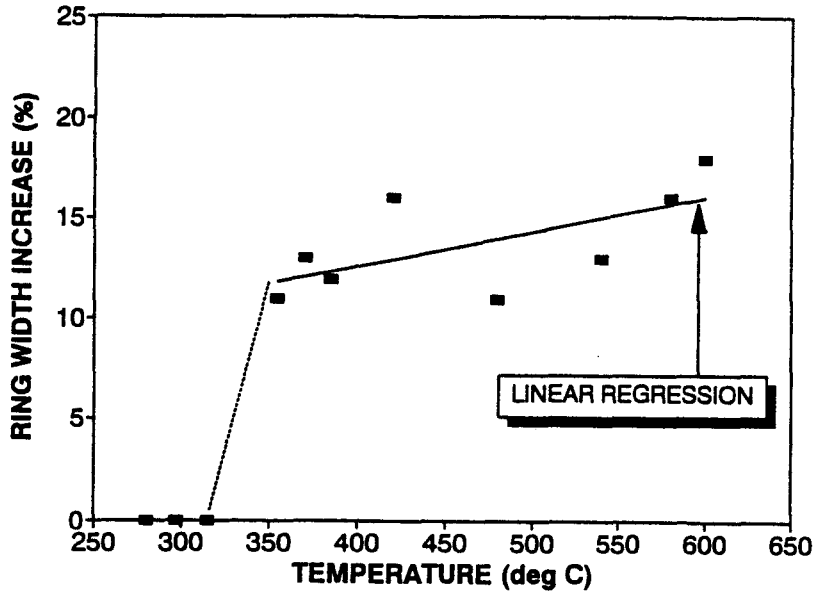

Figure H4: Ring growth as a function of test temperature

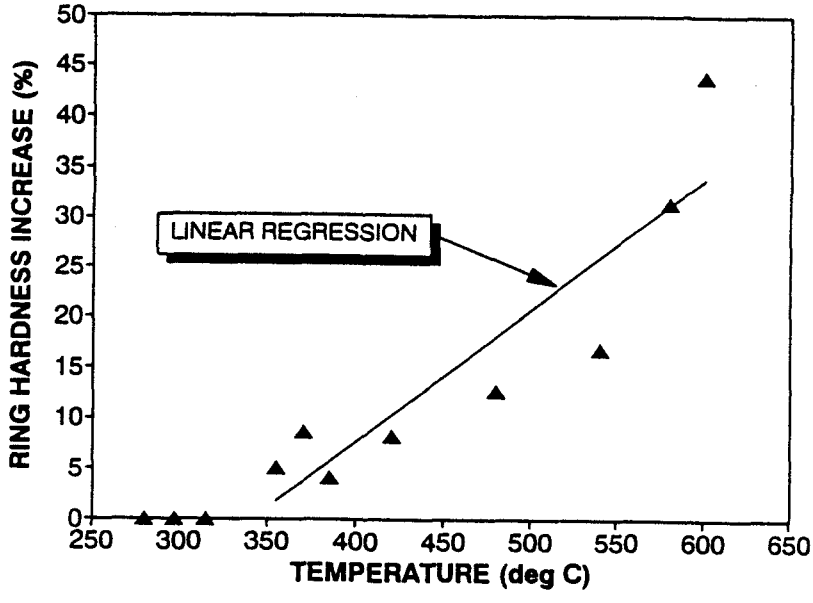

Figure H5: Ring hardness as a function of test temperature

Figure H5 shows the results of the hardness results, in which a regression line has also been plotted. The hardness values show a general increase over the temperature range. From these results, it is apparent that the dimensional growth occurs as a step change above 350°C,

whilst the hardness increases gradually as a function of temperature, also starting from 350°C.

Specimens from these rings (in the "before" and "after" state) were microscopically examined at various magnifications. As in the case study, it was found that the untested specimens showed longer graphite flake and negligible spheroidal free graphite compared to the specimens after testing.

APPENDIX I: DETONATION MODEL - BASIC CODE

The following code, written in BASIC solves for the detonation wave properties as a function of the initial pressure, temperature and equivalence ratio. The code was written to solve the equations developed in Appendix B for octane, methanol, ethanol and ethylene. Two programs, with a similar structure, were written. The first was used to model detonation conditions for air-fuel mixtures, while the second program modelled conditions for oxygen and ethylene mixtures. The differences lie in the use of the properties of ethylene and the fact that nitrogen is absent in detonation chamber simulation. However, the balance of these codes are identical. As a result, only the air-fuel model is presented in its entirety, followed by the modifications for the ethylene-oxygen program.

The state in which the code is presented is for constant initial pressure and mixture strength and variable initial temperature.

```
'*****************************************************************************************
'                    DETPROP.BAS
'PROGRAM TO CALCULATE DETONATION PROPERTIES OF THE END-GAS
'              IN SPARK-IGNITION ENGINES
'            [CHAPMAN-JOUGUET DETONATION WAVE]
'                    by Roy Nates
'*****************************************************************************************
'       ------ INITIAL STATEMENTS -------
'
   DIM U(2,10,8)      'PROPERTY COEFFICIENT
   DIM A(9)           'MOLES OF EACH SPECIES
   DIM VT(9)          'INTERMEDIATE VARIABLE
   DIM CV(9)          'SPECIFIC HEAT AT V              (kJ/kg.K)
   DIM CP(9)          'SPECIFIC HEAT AT P              (kJ/kg.K)
   DIM E(9)           'INTERNAL ENERGY                 (kJ/kg)
   DIM H(9)           'ENTHALPY                        (kJ/kg)
   DIM K(9)           'RATIO OF SPECIFIC HEATS
   DIM FU(9)          'DUMMY
   DIM FUDY(9)        'DUMMY
   DIM F(9)           'DUMMY
   DIM QTR(4)         'REAL ROOTS
   DIM QTI(4)         'IMAGINARY ROOTS
   DIM PHI(15)        'FUEL-AIR EQUIVALENCE RATIO
   DIM T1(15)         'INITIAL TEMPERATURE             (K)
   DIM P1(15)         'INITIAL PRESSURE                (bar)
   DIM AF(15)         'AIR-FUEL RATIO                  (mass basis)
   DIM P2(15)         'DETONATION STATIC PRESSURE      (bar)
   DIM T2(15)         'DETONATION TEMPERATURE          (K)
   DIM U1(15)         'DETONATION WAVE VELOCITY        (m/s)
```

```
DIM M2(15)        'BURNT-GAS MACH NUMBER          (behind wave)
DIM P02(15)       'DET STAGNATION PRESSURE        (bar)
DIM UP(15)        'BURNT-GAS VELOCITY             (m/s)
DIM GAMMA2(15)    'RATIO OF SPECIFIC HEATS
DIM RHO(15)       'BURNT-GAS DENSITY              (kg/m3)
RMOL = 8314.3     'UNIVERSAL GAS CONSTANT         (J/mol.K)
PI   = 3.1415927
'
'     ----- MAIN PROGRAM -------
'
      T1 = 600     ' STARTING INITIAL TEMPERATURE
      DDD% = 15    ' NUMBER OR DATA POINTS
      FOR II% = 1 TO DDD%
            GOSUB 2000          'INPUT VARIABLES
            GOSUB 2500          'ESTIMATE MOLES (NO DISSOCIATION)
            TT2 = T2+25         'DUMMY STARTING VALUE
            LOCATE 3,1
            PRINT "ESTIMATED T2      ="
                  WHILE ABS(TT2-T2) > 0.2    'ERROR LESS THAN 0.2 K
                        T2 =  (TT2+T2)/2
                        GOSUB 2600           'MEAN VALUES Cp; Cv; GAMMA &MW
                        GOSUB 3000           'ITERATION T2 AND P2
                        LOCATE 3,20
                        PRINT INT(TT2),"K"
                  WEND
            GOSUB 8000                       'DETERMINE U1 AND UP
'
                  PRINT "P1                  =";(INT(P1*10))/10,"bar"
                  PRINT "T1                  =";(INT(T1*10))/10,"K"
                  PRINT "PHI                 =";(INT(PHI*100))/100
                  PRINT "P2                  =";(INT(P2*10))/10,"bar"
                  PRINT "STAG PRESSURE       =";(INT(P02*10))/10,"bar"
                  PRINT "T2                  =";(INT(TT2*10))/10,"K"
                  PRINT "WAVE VELOCITY       =";(INT(U1*10))/10,"m/s"
                  PRINT "GAS VELOCITY        =";(INT(UP*10))/10,"m/s"
                  PRINT "GAMMA2              =";(INT(GAMMA2*1000))/1000
                  PRINT "MACH NUMBER         =";(INT(M2*1000))/1000
'
            PHI(II%) = PHI
            P2(II%)  = P2
            P02(II%) = P02
            T2(II%)  = T2
            U1(II%)  = U1
            UP(II%)  = UP
            RHO(II%) = (P2*1E5)/(R2*T2)
            AF(II%)  = (ATH/PHI)*4.76*29/(12*N + M + 16*PP)
            T1(II%)  = T1
            P1(II%)  = P1
            M2(II%)  = M2
'
            T1  = T1  + 50                   'NEXT DATA POINT
      NEXT II%
'
      GOSUB 9000                             'PREPARE OUTPUT FILE/PRINT
      END
'
```

```
730     ' ---- GAS PROPERTY COEFFICIENTS ----
'
        F% = 1
        RESTORE 1330
                FOR I% = 1 TO 9:FOR J% = 1 TO 8
                        READ U(F%,I%,J%)
                NEXT J% : NEXT I%
        F% = 2
        RESTORE 1590
                FOR I% = 1 TO 9:FOR J% = 1 TO 8
                        READ U(F%,I%,J%)
                NEXT J% : NEXT I%
        RETURN
'
860     '--- EQUILIBRIUM CONSTANTS : KP1 AND KP2 ---
'
        IF T < 3000 THEN F% = 1 ELSE F% = 2  'F%
                FOR I% = 1 TO 5
                        SUM = 0
                                FOR J% = 2 TO 5
                                        SUM = SUM + U(F%,I%,J%)*(T^(J%-1))/(J%-1)
                                NEXT J%
                        VT(I%) = SUM
                NEXT I%
                X1 = (U(F%,2,1)+U(F%,3,1)-U(F%,4,1)-U(F%,1,1))*(1-LOG(T))
                X1 = X1 - (VT(2)+VT(3)-VT(4)-VT(1))
                X1 = X1 - (U(F%,2,6)+U(F%,3,6)-U(F%,4,6)-U(F%,1,6))+(4.047E+07/(RMOL*T))
                LNKP1 = X1
        KP1 = EXP(LNKP1)
                X1 = (U(F%,2,1)+.5*U(F%,5,1)-U(F%,1,1))*(1-LOG(T))
                X1 = X1 - (VT(2)+.5*VT(5)-VT(1))
                X1 = X1 - (U(F%,2,6)+.5*U(F%,5,6)-U(F%,1,6))+(2.7969E+08/(RMOL*T))
                LNKP2 = X1
        KP2 = EXP(LNKP2)
        RETURN
'
1080    '----- CALCULATION OF Cv; Cp; k; H; E -----
'
        IF T < 3000 THEN F% = 1  ELSE F% = 2
                FOR I% = 1 TO 9
                        SUM1 = 0 : SUM2 =0 : SUM3 =0
                                FOR J% = 1 TO 5
                                        SUM1 = SUM1 + U(F%,I%,J%)*(T^(J%-1))
                                        SUM2 = SUM2 + J%*U(F%,I%,J%)*(T^(J%-1))
                                        SUM3 = SUM3 + U(F%,I%,J%)*(T^J%)
                                NEXT J%
                        FU(I%) =   SUM1
                        FUDY(I%) = SUM2
                        F(I%) =    SUM3
                        H(I%) = RMOL*F(I%)                  'J/KMOL
                        E(I%) = RMOL*(F(I%)-T)              'J/KMOL
                        CV(I%)= RMOL*(FUDY(I%)-1)           'J/KMOL.K
                        CP(I%)= CV(I%) + RMOL
                        K(I%)  = CP(I%)/CV(I%)
                NEXT I%
        RETURN
```

```
1330 ' ----- LOW TEMPERATURE DATA  (500 - 3000K) -----
'
        ' CARBON DIOXIDE
       DATA 3.09590,  2.73114E-3, -7.88542E-7,  8.66002E-11, 0
       DATA 6.58393, -3.93405E 8,          44.01
       ' CARBON MONOXIDE
       DATA 3.31700,  3.76970E-4, -3.22080E-8, -2.19450E-12, 0
       DATA 4.63284, -1.13882E 8,          28.011
       ' WATER
       DATA 3.74292,  5.65590E-4,  4.95240E-8, -1.81802E-11, 0
       DATA .965140, -2.39082E 8,          18.015
       ' HYDROGEN
       DATA 3.43328, -8.181E-6,  9.66990E-8, -1.44392E-11, 0
       DATA -3.84470,          0,          2.016
       ' OXYGEN
       DATA 3.25304,  6.52350E-4, -1.49524E-7,  1.53897E-11, 0
       DATA 5.71243,          0,          31.999
       ' NITROGEN
       DATA 3.34435,  2.94260E-4,  1.95300E-9, -6.57470E-12, 0
       DATA 3.75863,          0,          28.013
       ' C8H18
       DATA -0.71993,  4.64260E-2, -1.68385E-5,  2.670090E-9, 0
       DATA       0, -4.82318E8,          114
       ' METHANOL
       DATA 2.285   ,  5.504E-3  , -4.8913E-7,  -2.4173E-10, 0
       DATA       0, -1.91068E8,          32.042
       ' ETHANOL
       DATA 2.394   ,  1.2605E-2 , -4.1617E-6,  6.029E-10,   0
       DATA       0, -2.24298E8,          46.07
'
1590 ' ----- HIGH TEMPERATURE DATA  (3001 - 6000K) -----
'
       ' CARBON DIOXIDE
       DATA 5.20816,  5.90837E-4, -5.61431E-8,  2.04685E-12, 0
       DATA -4.32923, -3.93405E 8,          44.01
       ' CARBON MONOXIDE
       DATA 3.53114,  2.73436E-4, -3.27672E-8,  1.56492E-12, 0
       DATA 3.41176, -1.13882E 8,          28.011
       ' WATER
       DATA 3.92119,  6.58323E-4,  0.21913E-8,  2.15227E-12, 0
       DATA -.242340, -2.39082E 8,          18.015
       ' HYDROGEN
       DATA 3.21299,  2.87156E-4, -2.28839E-8,  7.6656E-13, 0
       DATA -2.78598,          0,          2.016
       ' OXYGEN
       DATA 3.55064,  3.20312E-4, -2.87575E-8,  1.00528E-12, 0
       DATA 4.20945,          0,          31.999
       ' NITROGEN
       DATA 3.51443,  2.58314E-4, -2.84107E-8,  1.24154E-12, 0
       DATA 2.74113,          0,          28.013
       ' C8H18
       DATA -0.71993,  4.64260E-2, -1.68385E-5,  2.670090E-9, 0
       DATA       0, -4.82318E8,          114
       ' METHANOL
       DATA 2.285   ,  5.504E-3  , -4.8913E-7,  -2.4173E-10, 0
       DATA       0, -1.91068E8,          32.042
       ' ETHANOL
       DATA 2.394   ,  1.2605E-2 , -4.1617E-6,  6.029E-10,   0
```

```
      DATA      0, -2.24298E8,        46.07
'
2000' ----- INPUT VARIABLES ------
'
      FF% = 7        'USING OCTANE  DATA
'     FF% = 8        'USING METHANOL DATA
'     FF% = 9        'USING ETHANOL  DATA
            IF FF%=7 THEN N=8 : M=18 : PP=0
            IF FF%=8 THEN N=1 : M=4  : PP=1
            IF FF%=9 THEN N=2 : M=6  : PP=1
'
      PHI = 1.1      'EQUIVALENCE F/A
      P1 = 60        'INITIAL PRESSURE  (bar)
      T2 = 3000      'DUMMY ESTIMATE
      PER =  0       'PERCENT ETHANOL by mass
'
            Y1 = PER/46          'ONLY USED FOR BLENDS
            Y2 = (100-PER)/114
            AL = Y1/(Y1+Y2)      'MOLES OF ETHANOL
            HH = Y2/(Y1+Y2)      'MOLES OF OCTANE
'
      RETURN
'
2500' ---- ESTIMATE VALUES FOR PRODUCT k AND MW -----
          'ASSUMES NO DISSOCIATION
'
      ATH = N + M/4 - PP/2
            IF PHI <=1 THEN A(1)=N ELSE A(1) = PP + (2*ATH/PHI) - N - M/2
            IF PHI <=1 THEN A(2)=0 ELSE A(2) = N - A(1)
      A(3) = M/2   : A(4) = 0
            IF PHI >1  THEN A(5)=0 ELSE A(5) = PP/2 +ATH/PHI -N -M/4
      A(6) = 3.76*ATH/PHI
'
      RETURN
'
2600 '----- MEAN VALUES FOR Cp; Cv; GAMMA & MW FOR BURNT AND UNBURNT-GAS -----
'
      WHILE FLAG <> 1
      FLAG = 1
'
 'CALCULATE MEAN CP, CV, GAMMA & MW FOR REACTANTS
      T = T1
            GOSUB 1080                          'CALCULATE CP AND CV
            WR = 1 + (ATH/PHI)*4.76             'MOLES REACTANTS
            CPR = (HH*CP(FF%)+AL*CP(9) + (ATH/PHI)*CP(5) + (3.76*ATH/PHI)*CP(6))/WR
            CVR = (HH*CV(FF%)+AL*CV(9) + (ATH/PHI)*CV(5) + (3.76*ATH/PHI)*CV(6))/WR
            GAMMA1 = CPR/CVR
            MWR = (HH*U(F%,FF%,8) + AL*U(F%,9,8) + (ATH/PHI)*U(F%,5,8)
                              +(3.76*ATH/PHI)*U(F%,6,8))/WR
      WEND
'
2650 '----- CALCULATE MEAN CP, CV, GAMMA & MW FOR PRODUCTS (PER MOLE FUEL) -----
      T = T2
            GOSUB 1080                          'CALCULATE CP AND CV
            WP = A(1) + A(2) + A(3) + A(4) + A(5) + A(6) 'MOLES OF PRODUCT
            SUM1 = 0 : SUM2 = 0 : SUM3 = 0
                  FOR J% = 1 TO 6
                        SUM1 = SUM1 + CP(J%)*A(J%)
```

```
                        SUM2 = SUM2 + CV(J%)*A(J%)
                        SUM3 = SUM3 + A(J%)*U(F%,J%,8)
                    NEXT
                CPP = SUM1/WP
                CVP = SUM2/WP
                GAMMA2 = CPP/CVP
                MWP = SUM3/WP
                R1 = RMOL/MWR
                R2 = RMOL/MWP
'
        RETURN
'
3000' ---- ITERATION USING ASSUMED T2 TO DETERMINE DETONATION PROPERTIES ----
'
        R1 = RMOL/MWR
        R2 = RMOL/MWP
                X = (1/GAMMA2) + 1 - ((R1*T1)/(R2*T2))
                MU = 0.5*X + 0.5*(((X^2) + 4*R1*T1/(R2*T2))^0.5)
        P2 = MU*R2*T2*P1/(R1*T1)
        T = T2
'
        GOSUB 860                                   'CALCULATE KP1 AND KP2
                A = MU*T2*(P1/101.325)/(T1*WR)
                B = (2/PHI)*ATH - (N+M/2)
                C = (1/KP1)-1
                D = A*(KP2^2)
'
    'SET UP COEFTS OF QUARTIC EQUATION
                QT1 = 2*C   'COEFT OF X^4
                QT2 = 4*C/D +M -2*B*C +2*N -4*C*N
                QT3 = 2*C*N^2 -4*N^2 +4*B*C*N -3*N*M +4*N/D -2*B*N
                QT4 = 2*N^3 -2*B*C*N^2 +4*B*N^2 +3*M*N^2
                QT5 = -(2*B +M)*N^3
        GOSUB 7000
        J% = 1
                WHILE QTR(J%) < 0 AND QTR(J%) > N
                J% = J%+1
                WEND
                        X = QTR(J%)
                        A = MU*T2*(P1/101.325)/(T1*WR)
                        B = (2/PHI)*ATH - (N+M/2)
                        C = (1/KP1)-1
                        D = A*(KP2^2)
                A(1) = X
                A(2) = N - A(1)
                A(5) = ((A(1)/A(2))^2)/D
                A(3) = PP + 2*(ATH/PHI) - 2*A(1) - A(2) - 2*A(5)
                A(4) = M/2 - A(3)
                A(6) = (3.76/PHI)*ATH
'
      'INTERNAL ENERGY OF REACTANTS
        T = T1
        GOSUB 1080
        ER = HH*(E(FF%)+U(F%,FF%,7))+AL*(E(9)+U(F%,9,7))+(ATH/PHI)*(E(5)+3.76*E(6))
'
      'INTERNAL ENERGY OF PRODUCTS
        T = T2
        GOSUB 1080
```

```
        SUM1 = 0
                FOR I% = 1 TO 6
                        SUM1 = SUM1 + A(I%)*(E(I%)+U(F%,I%,7))
                NEXT
        EP = SUM1                       'INTERNAL ENERGY OF PRODUCTS (J/KMOL)
        GOSUB 2600
                N2 = MWR/MWP
                FE = N2*EP - ER - (N2*RMOL*T2/(GAMMA2*2))
        TT2 = T2 - FE/(N2*WP*CVP - 0.5*N2*RMOL/GAMMA2)      'ITERATION FOR NEW TEMP
'
        RETURN
'
7000  '----- ROOTS OF QUARTIC EQUATION -----
'
        GOSUB 7440
        RETURN
'
7440  ' ----- SUBROUTINE: QUARTIC -----
'
' Equation: QT1*X^4 + QT2*X^3 + QT3*X^2 + QT4*X + QT5
' Solution: QTR(J) + i*QTI(J)
'
        A0=QT5/QT1:A1=QT4/QT1:A2=QT3/QT1:A3=QT2/QT1
                A=A3/2
                        CB1=1:CB2=-A2:CB3=A1*A3-4*A0:CB4=A0*(4*A2-A3*A3)-A1*A1
                                GOSUB 7670    'Cubic solution
                IF CBI<>0 THEN GOTO 7560
                        IF CBR1<CBR2 THEN CBR1=CBR2
                                IF CBR1<CBR3 THEN CBR1=CBR3
'
7560            B=CBR1/2
                        IF  B*B>A0  THEN  D=SQR(B*B-A0):CA=-(A1/2-A*B)/D  ELSE
                D=0:CA=SQR(A*A+2*B-A2)
                        QD1=1:QD2=A-CA:QD3=B-D
                                GOSUB 7930    'Quadratic solution
                QTR(1)=QDR1:QTR(2)=QDR2:QTI(1)=QDI
                        QD1=1:QD2=A+CA:QD3=B+D
                                GOSUB 7930    'Quadratic solution
                QTR(3)=QDR1:QTR(4)=QDR2:QTI(3)=QDI
                QTI(2)=-QTI(1):QTI(4)=-QTI(3)
        RETURN
'
7670  ' ----- SUBROUTINE: CUBIC -----
'
' Equation: CB1*X^3 + CB2*X^2 + CB3*X + CB4
' Solution: CBR1, CBR2, CBR3, CBI
'
                IPATH=2:EX=1/3
                        IF CB4=0 THEN CBR1=0:GOTO 7880
                AZ=CB1*CB1
                Q=(27*AZ*CB4-9*CB1*CB2*CB3+2*CB2^3)/(54*AZ*CB1)
                        IF Q=0 THEN Z=0:GOTO 7870
                                IF Q<0 THEN IPATH=1:Q=-Q
                P=(3*CB1*CB3-CB2*CB2)/(9*AZ)
                ARG=P^3+Q^2
                        IF ARG<0 THEN Z=-2*SQR(-P)*COS(ATN(SQR(-ARG)/Q)/3):GOTO 7860
                                IF ARG=0 THEN Z=-2*Q^EX:GOTO 7860
                SARG=SQR(ARG)
```

```
                IF P<0 THEN Z=-(Q+SARG)^EX-(Q-SARG)^EX:GOTO 7860
                    IF P=0 THEN Z=-(2*Q)^EX:GOTO 7860
            Z=(SARG-Q)^EX-(SARG+Q)^EX
7860            IF IPATH =1 THEN Z=-Z
7870        CBR1=(3*CB1*Z-CB2)/(3*CB1)
7880        QD1=CB1:QD2=CB2+CBR1*CB1:QD3=CB3+CBR1*QD2
            GOSUB 7930 '    Quadratic solution
            CBR2=QDR1:CBR3=QDR2:CBI=QDI
        RETURN
'
7930  ' ----- SUBROUTINE: QUADRATIC -----
'
 ' Equation: QD1*X^2 + QD2*X + QD3
 ' Solution: QDR1, QDR2, QDI
'
            X1=-QD2/(2*QD1)
                DISCRIM=X1*X1-QD3/QD1
                    IF  DISCRIM<0  THEN  X3=SQR(-DISCRIM):X2=0  ELSE
            X2=SQR(DISCRIM):X3=0
                QDR1=X1+X2:QDR2=X1-X2:QDI=X3
        RETURN
'
8000  '----- CALCULATE WAVE AND GAS VELOCITY -----
'
        U1 = MU * ((GAMMA2*RMOL*T2/MWP)^0.5) 'WAVE VELOCITY
        UP = U1 - (GAMMA2*R2*T2)^0.5          'GAS VELOCITY
        M2 = UP/((GAMMA2*R2*T2)^0.5)          'MACH No OF GAS
        P02 = P2*(1 + ((GAMMA2-1)/2)*M2^2)^(GAMMA2/(GAMMA2-1)) 'STAGNATION PRESSURE
        RETURN
'
9000  '----- PREPARE OUTPUT FILE -----
'
            OPEN "D2-4-3.WQ1" FOR OUTPUT AS #1
                FOR J%=1 TO DDD%
                    Q$=STR$(PHI(J%))+";"+STR$(P1(J%))+";"+STR$(T1(J%))
                    Q$=Q$+";"+STR$(P2(J%))+";"+STR$(P02(J%))+";"+STR$(T2(J%))
                    Q$=Q$ +";"+STR$(U1(J%))+";"+STR$(UP(J%))+";"+STR$(RHO(J%))
                    Q$=Q$ +";"+STR$(M2(J%))
                    PRINT #1,Q$
                NEXT J%
            CLOSE #1
        RETURN
'
'*************************************************************************************************
```

The following lines of code where added to the above program to simulate the detonation of ethylene-oxygen mixtures used in the detonation chamber tests. Line 1081, shown below, was added to include the properties of ethylene. Lines 2500, 2600 and 2650 replaced their respective line numbers in the above program to exclude nitrogen from the chemical reaction.

```
1081 ' CALCULATION OF PROPERTIES OF ETHYLENE (C2H4)
'
              WHILE FLAGG < > 1
                   FLAGG = 1
                         TTT = T1
                         GOSUB 1100
                               CP(10) = FUNC
                               CV(10) = CP(10) - RMOL
                               K(10) = CP(10) / CV(10)
'
'     SIMPSON'S RULE INTEGRATION OF CP(T) TO DETERMINE H(T)
'
                   SUM1 = 0: SUM2 = 0
                   Z% = 300                    'NUMBER OF INTERVALS
                   INTT = (T1 - 298) / Z%      'SIZE OF INTERVALS
                         FOR I% = 1 TO Z% - 1
                               TTT = 298 + INTT * I%
                               GOSUB 1100
                               SUM1 = SUM1 + FUNC
                         NEXT I%
                         FOR I% = 1 TO Z%
                               TTT = (2 * I% - 1) * INTT / 2 + 298
                               GOSUB 1100
                               SUM2 = SUM2 + FUNC
                         NEXT I%
                   TTT = 298:    GOSUB 1100:   FXO = FUNC
                   TTT = T1:     GOSUB 1100:   FXN = FUNC
'
             HT = (T1 - 298) * (FXO + FXN + 2 * SUM1 + 4 * SUM2) / (6 * Z%)
             H(10) = HT + 52318                'ENTHALPY (J/MOL.K)
             E(10) = H(10) - RMOL * T1         'INTERNAL ENERGY (J/MOL.K)
'
             WEND
'
             RETURN
'
1100         FUNC = 28.7902 + 128.8856 * EXP(-527.1308 / (TTT ^ .9644))
             RETURN

2500 ' ---- ESTIMATE VALUES FOR PRODUCT k AND MW -----
             'ASSUMES NO DISSOCIATION
'
             ATH = N + M / 4
                   IF PHI < = 1 THEN A(1) = N ELSE A(1) = (2 * ATH / PHI) - N - M / 2
                   IF PHI < = 1 THEN A(2) = 0 ELSE A(2) = N - A(1)
             A(3) = M / 2: A(4) = 0
                   IF PHI > 1 THEN A(5) = 0 ELSE A(5) = ATH / PHI - N - M / 4
```

```
            A(6) = 0
'
            RETURN
'
2600 '----- MEAN VALUES FOR Cp; Cv; GAMMA & MW -----
'
            WHILE FLAG <> 1
                  FLAG = 1
'
 'CALCULATE MEAN CP, CV, GAMMA & MW FOR REACTANTS
                  T = T1
                  GOSUB 1080                    'CALCULATE CP AND CV
                        WR = 1 + (ATH / PHI)              'MOLES REACTANTS
                        CPR = (CP(FF%) + (ATH / PHI) * CP(5)) / WR
                        CVR = (CV(FF%) + (ATH / PHI) * CV(5)) / WR
                        GAMMA1 = CPR / CVR
                        MWR = (28 + (ATH / PHI) * U(F%, 5, 8)) / WR
            WEND
'
2650 '----- CALCULATE MEAN CP, CV, GAMMA & MW FOR PRODUCTS (PER MOLE FUEL) -----
'
            T = T2
            GOSUB 1080  'CALCULATE CP AND CV
      WP = A(1) + A(2) + A(3) + A(4) + A(5)      'MOLES OF PRODUCT
            SUM1 = 0: SUM2 = 0: SUM3 = 0
                  FOR J% = 1 TO 5
                        SUM1 = SUM1 + CP(J%) * A(J%)
                        SUM2 = SUM2 + CV(J%) * A(J%)
                        SUM3 = SUM3 + A(J%) * U(F%, J%, 8)
                  NEXT
'
            CPP = SUM1 / WP
            CVP = SUM2 / WP
            GAMMA2 = CPP / CVP
            MWP = SUM3 / WP
            R1 = RMOL / MWR
            R2 = RMOL / MWP
'
            RETURN
```